A Design Tool for Conveyor Belt Furnaces

PROEFONTWERP

ter verkrijging van de graad van doctor aan de
Technische Universiteit Eindhoven, op gezag van de
Rector Magnificus, prof. dr. M. Rem, voor een
commissie aangewezen door het College voor Promoties
in het openbaar te verdedigen op
woensdag 1 november 2000 om 16.00 uur

door

Maurice Pierre Marie Arthur Limpens

geboren te Geleen

Dit proefontwerp is goedgekeurd door de promotoren:

prof.dr.ir. A.A. van Steenhoven
en
prof.dr.ir. R.M.M. Mattheij

Copromotor:

dr.ir. C.C.M. Rindt

CONTENTS

CHAPTER 1. INTRODUCTION

1.1 Problem description

The company Gemco Furnaces manufactures industrial furnaces for several purposes. One type of furnace built by Gemco is the so called "conveyor belt furnace". This is a furnace type in which the products are heated up and cooled down while they are transported through the furnace by means of a conveyor belt. All kinds of products can be treated in the furnace. Examples are ceramics or electronic components.
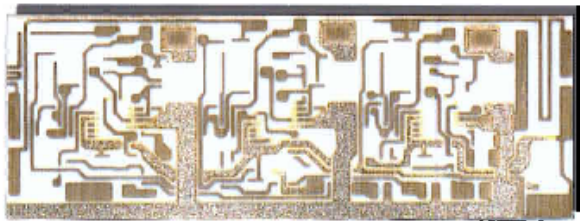
Figure 1.1. Ceramic IC-board produced by direct copper bonding.
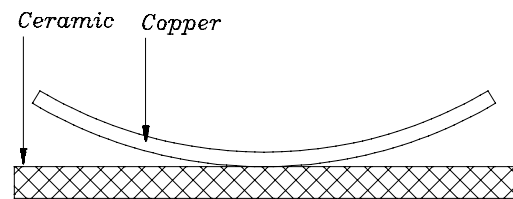
Figure 1.2. Copper flake on a ceramic base material at the beginning of the process.

A typical production process is the so called DCB process (direct copper bonding) for the production of ceramic IC-boards, as depicted in Figure 1.1. Because ceramic IC-boards can be used in a wide temperature range, they are especially suitable for use in aviation and aerospace technology. In the production process, first a copper top layer is attached to a ceramic base material, which usually consists of Al_2O_3 (alumina). After the bonding process a circuit is etched in the copper top layer in order to produce the IC-board. The bonding of the copper to the ceramic occurs at a high temperature, and therefore, the materials are heated in a conveyor belt furnace. At the beginning of the production process, a thin copper foil lies on a ceramic base material as depicted in Figure 1.2. The sides of the copper foil are bent upwards, so that the bonding process starts in the middle, and then continues to the sides as the copper sags out under its own weight because of the high temperature. In this way, air enclosures are prevented in order to guarantee a good product quality. The copper bonds to the ceramic at 1063 [°C]. This temperature however is only 2 [°C] lower than the melting point of copper. When the melting point is reached, the sides of the copper foil will hang down and hit the ceramic too early, causing air enclosures and thus a useless product. Therefore, furnaces used for this production process must have a very high temperature accuracy and adjustability. As in a typical production process several products are placed next to each other on the belt, it is also very important that the temperature distribution over the width of the belt is uniform. A non-uniform temperature distribution is the main problem of this type of furnaces, and improving the temperature uniformity is the main goal of this study. As an ultimate design requirement, for an optimized furnace a maximum temperature difference of approximately 1 [°C] over the width of the belt is aimed at.

Another production process for which temperature uniformity is of great importance is the production of flat panel displays. The display is produced by attaching coatings to a glass plate at a temperature of about 600 [°C]. To prevent the glass from breaking, the thermal stresses during the heating and cooling process have to be kept as low as possible, and therefore, also here the temperature uniformity is very important.

At the moment, Gemco is building their furnaces based on years of experience and with the aid of some temperature measurements that are done on newly produced furnaces. In order to get the required temperature history for the production process, a furnace is equipped with electronics to control the power output of the heating elements. This method can be used for building standard furnaces. However, for very critical production processes or for a new type of conveyor belt furnace designed for special demands, this method is extremely laborious. Therefore it is necessary to get a better understanding of the heat transfer phenomena inside a furnace. The goal is to be able to calculate disturbances in temperature uniformity for a furnace with given settings of the element power.

1.2 Description of a conveyor belt furnace

In Figure 1.3 a schematic presentation of a conveyor belt furnace is shown. The products are placed on a belt, which is pulled through the muffle. The muffle is a tube, made of a heat resistant nickel-chromium alloy, in which a controlled atmosphere is realized depending on the production process. For the DCB process a nitrogen atmosphere is needed to avoid oxidation of the products at high temperatures. This atmosphere is controlled by means of gas inlet pipes, as depicted in Figure 1.5. The products are heated by circumferentially positioned electrical heating elements, placed outside the muffle. The temperature of the heating elements varies along the length of the furnace, so that the products are heated not too fast and high material stresses are avoided. This is realized by dividing the furnace in a number of zones, each with its own temperature setting for the heating elements.
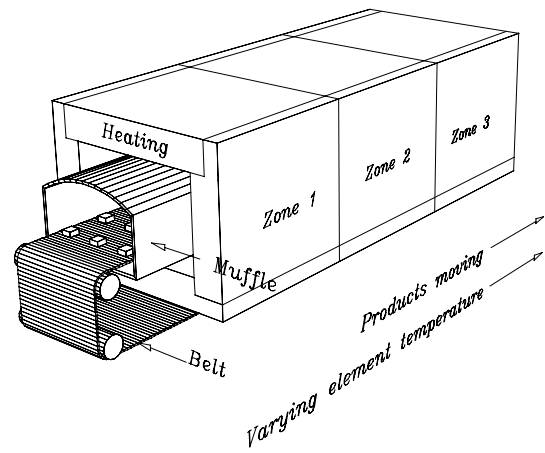
Figure 1.3. Conveyor belt furnace.
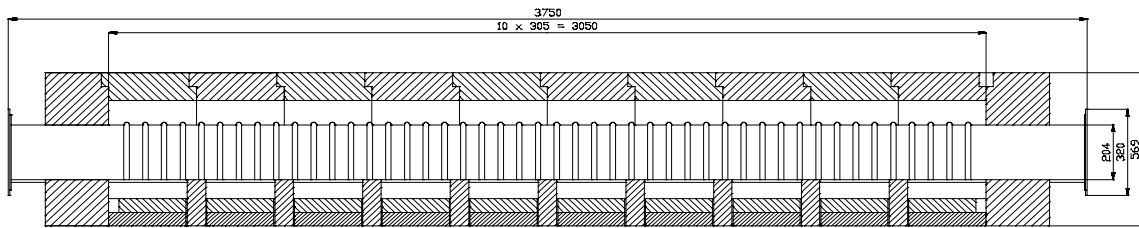
Figure 1.4. Global dimensions of the heating section of a real furnace (side view).

1 Muffle
2 Heart plate
3 Belt
4 Gas inlet
5 Product
6 Support stone
7 Stones containing heating elements.
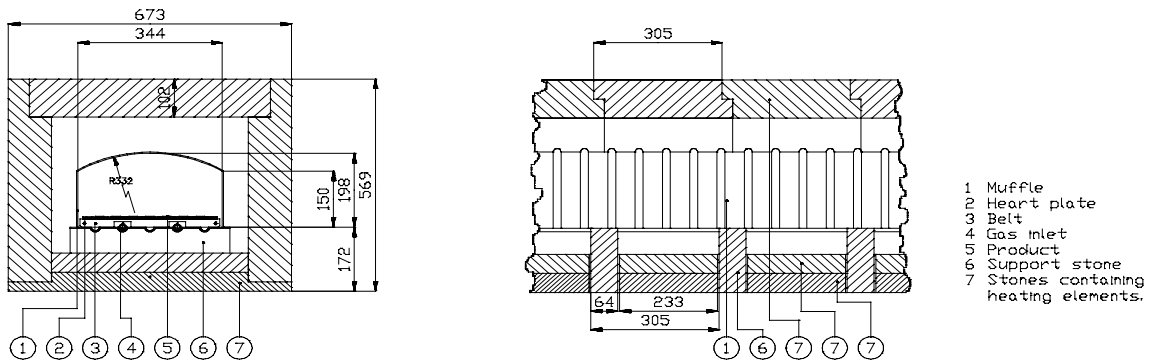
Figure 1.5. Cross sectional area and detailed side view.

The total heating section of a real conveyor belt furnace is usually about 3 meters long, but the exact length is also process dependent. After the heating section there is also a cooling section, in order to let the products cool down in a controlled way. As the main problem occurs in the heating section, the cooling section is not considered in this project. Some global dimensions of the heating section of a furnace are given in Figure 1.4 and Figure 1.5. A detailed view of cross-sectional muffle dimensions is given in appendix 7.

In Figure 1.4 a side view of the heating section of a the furnace is drawn. The heating section consists of 10 zones of 305 [mm]. On the left in Figure 1.5 a cross sectional area through a heating section is shown. Inside the muffle a belt is transporting the products through the furnace. The belt is carried by hearth plates, which are resting on the bottom of the muffle. On the right in the same figure a more detailed side view of a part of the furnace is shown to give some global dimensions. The muffle is carried by support stones, and heated by electrical heating elements placed around the muffle. The heating elements are constructed as depicted in Figure 1.6. Inside the heat resistant stones surrounding the muffle, grooves are milled containing spirals of heat resistant wires (Kanthal wire). A large electrical current is sent through the Kanthal wires, heating both the wires and the heat resistant stones. Because of the high element temperature, heat transfer between the elements and the muffle will mainly occur by radiation.

As mentioned before, the products are heated up slowly by setting the element temperature of every zone to a different value. In order to get a homogeneous temperature distribution in each cross section through the muffle, the input power to the four heating elements in each zone can be controlled separately. For furnaces with a belt width greater than 200 [mm] and a high required temperature accuracy (absolute accuracy about 2.5 [°C] or better), there are three control units per heating zone, which can be connected to the heating elements in the two different ways shown
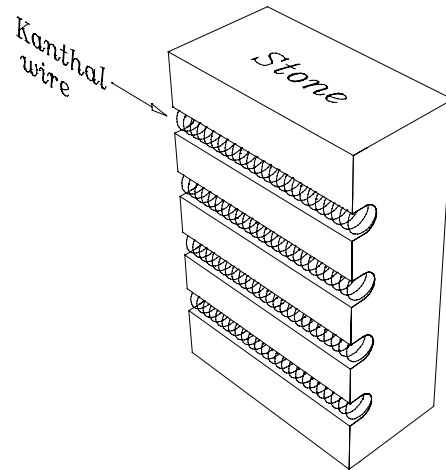
Figure 1.6. Construction of the heating elements.
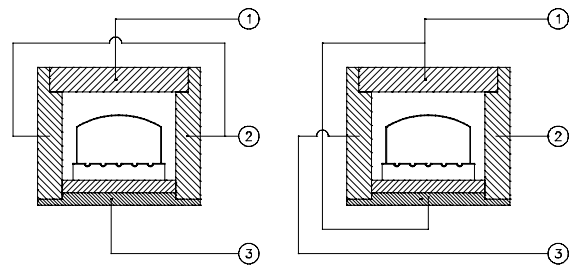
Figure 1.7. Different ways of connecting the control units to the heating elements.

Zone	T_{set} [°C]	Relative input power of the elements %		
		Side	Bottom	Top
1	500	100	100	100
2	600	100	100	100
3	750	100	100	100
4	850	100	100	100
5	900	100	100	100
6	900	75	100	75
7	900	75	100	75
8	900	75	100	75
9	900	75	100	75
10	850	100	100	100

Table 1. Temperature and relative power settings for the heating elements per zone.

in Figure 1.7. Either the two side elements or the top and bottom element are controlled by the same unit. In Table 1 the set temperature and the power distribution for every zone used during a test measurement are given. In the furnace under consideration the two side elements are connected to one control unit. Except for the somewhat low maximum temperature (900 [℃]) the values are representative for a furnace operating in a production process.

In order to get an impression of the product temperature history, temperature measurements were done in a newly built conveyor belt furnace at Gemco, using the settings given in Table 1. During this measurement, the belt speed was 180 [mm/min], which is a typical value for the belt speed in a conveyor belt furnace. In Figure 1.8 the measured temperature history for a thermocouple in the middle of the belt is depicted. The product temperature varies between 25 [℃] and 900 [℃]. From comparisons between thermocouples divided over the width of the belt, the temperature differences appeared to be a few degrees, causing the bonding problems as explained earlier.
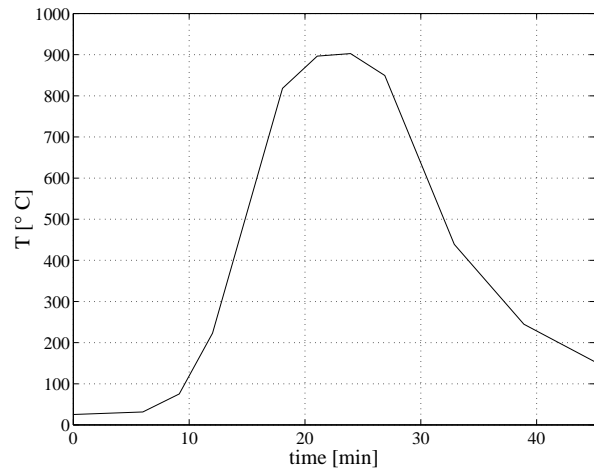
Figure 1.8. Temperature history measured by the thermocouples.

1.3 Model simplifications

Global heat transfer phenomena

As depicted in Figure 1.9, heat transfer will be caused by radiation, conduction and convection through the medium inside the muffle, as well as by conduction through the belt with the products. Because of the relatively low value of the belt speed, forced convection induced by the movement of the belt is assumed to be of minor influence on the heat transfer. However, natural convection inside the muffle may be an important effect disturbing the temperature uniformity over the width of the belt. As the belt with the products is cooler than the muffle, a natural convection pattern as depicted in Figure 1.10 is expected in a cross-section of the muffle. The relatively hot muffle will heat the medium near its walls, causing the medium to get a lower density. This will induce an upward flow towards the top of the muffle, resulting in two opposite rotating vortices in the region above the belt. When flowing downwards in the middle of the muffle, the medium will be relatively hot, as it was heated while streaming along the muffle walls. Flowing
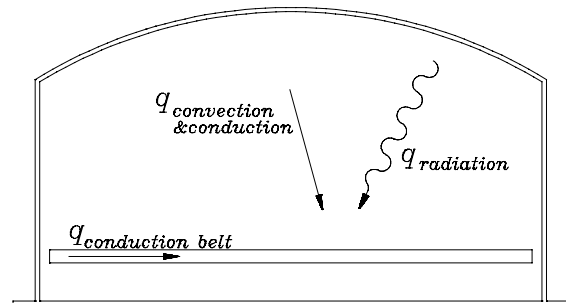
Figure 1.9. Heat fluxes inside the muffle.
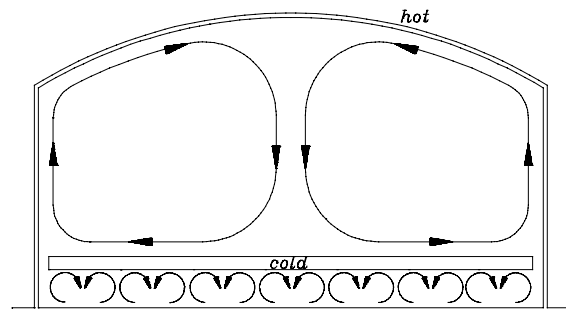
Figure 1.10. Expected convection pattern in a cross-section of the muffle.

towards the sides of the muffle over the relatively cold belt surface the medium will be cooled because of convective heat fluxes to the belt. As this convective heat transfer is the strongest for large temperature differences between the belt and the medium, it is expected to decrease towards the sides, causing a non-uniform temperature at the top surface of the belt. In the region below the belt, Rayleigh-Bénard convection cells are expected to appear. This convection pattern may influence the temperature distribution of the bottom surface of the belt. Temperature gradients in axial direction will cause one or more axial vortices, divided over the length of the muffle. It is expected that the influence of these axial vortices on the temperature uniformity over the width of the belt is relatively weak compared to the influence of the cross-sec-

Figure 1.11. Expected 3-D convection pattern for a given axial temperature profile in the case of relatively strong axial vortices.

tional vortices. In general, the combination of the axial and the cross-sectional convective effects is difficult to sketch. If the axial effects are strong in comparison to the cross-sectional effects, a pattern as indicated in Figure 1.11 is to be expected.

Next to convection, also radiative heat transfer from the muffle to the belt with products will play an important role in the furnace problem. As high muffle temperatures appear, radiative effects are supposed to be more important than convective effects. The effect of radiation on the temperature uniformity is not obvious at first sight. Conductive heat transfer through the belt with the products will probably have an equalizing effect decreasing the non-uniformity. The importance of this effect highly depends on the belt properties.

Model choices

For modelling an industrial furnace several heat transfer phenomena have to be taken into account. As a conveyor belt furnace has a relatively large length compared to its cross-sectional dimensions, heat transfer effects in a cross-section are expected to be stronger than axial effects. Therefore, it is assumed that a 2-*D* model is a suitable basis for calculating heat transfer effects in the furnace. The 3-*D* heat transfer effects can then be incorporated in the 2-*D* model as source terms, which sizes can be determined from measurements in an experimental set-up. The advantage of such a model compared to a complete 3-*D* model is that it serves better as a design tool, because a complete 3-*D* model including radiation, convection and conduction will require a lot of computing power and time for calculating a furnace problem.

In the cross-section of the muffle, there are two different geometries in which the heat transfer has to be calculated. First there is the muffle geometry, in which a medium is situated, which transports heat from the muffle walls to the belt surface by convection, and through which radiation passes from the muffle walls to the belt surface. Based on the dimensions of the muffle and on the occuring temperature gradients, the flow is assumed to be laminar. Inside the muffle geometry the second geometry is situated, which is the belt with the products. Heat is transported through this geometry by conduction, while it is heated up in time. The two geometries are coupled by the heat transfer fluxes at the surfaces of the belt and the products.

Because of mechanical strength considerations, the muffle roof of an industrial conveyor belt furnace will allways have a curved shape. The curved roof and the inclined belt with products make the muffle geometry rather complex. A finite element approach is suitable for calculating the flow phenomena in such complex geometries, because of its ability to use unstructured and locally refined meshes. As the finite element method can also be used for the conduction calculation in the belt with the products, the coupling between the belt and the muffle geometry can easily be made. For calculating the radiation from the muffle to the belt, a radiation model must be used. Also this radiation model should fit within the finite element formulation. Such a radiation model is the discrete ordinate method. The radiative phenomena are described mathematically in terms of differential equations, which then can be discretized and solved using finite elements.

1.4 Outline of the thesis

As the main problem is temperature uniformity over the belt width, the project is divided into three main parts. In order to understand the causes of the temperature differences, first a numerical model is built for analysing the various heat fluxes inside the muffle. As a standard finite element package including radiation was not available, a radiation model based on the discrete ordinate method was programmed. This radiation model is combined with the commercially available finite element package SEPRAN, which is mainly designed for solving heat and flow problems. Because of the open structure of the package it is very suitable for use in combination with self written routines, like the radiation model in this case. The second main task is building an experimental set-up. This set-up will be used to check the numerical model and some devised measures of improvement. Therefore, the set-up must contain measuring equipment, and it must simulate important aspects of a real conveyor belt furnace. With the experimentally validated program measures for improving the temperature uniformity can be evaluated. As the model must serve as a design tool, an important demand is to keep the model as simple as possible. The third main task of the project is presenting an improved furnace design, suitable for practical use.

In chapter 2 the radiation model is described. From the standard transport equation for radiation intensity a special 'plane' discrete ordinate model is derived for non-absorbing media, which enables efficient radiation calculations in a furnace. Special attention is paid to the complex boundary conditions, involving specular and diffuse reflections. In chapter 3 attention is paid to the complete furnace model. The Navier-Stokes equations for natural convection in the medium and the transient conduction equation for the belt are derived. The total structure of the furnace model shows the coupling between all the heat transfer equations. At the end of this chapter some test results are shown. In chapter 4 the design of the experimental set-up is described, together with the measurement strategy for model validation and determination of 3-*D* effects. Chapter 5 contains an analysis of the furnace, showing the measurement results, and an estimation of the 3-*D* heat transfer effects. At last, the furnace design is optimized in chapter 6.

CHAPTER 2. RADIATIVE HEAT TRANSFER

In general, radiative heat transfer can be described by the transport equation for radiation intensity. In order to solve this differential equation it is discretized using the discrete ordinate method in combination with the finite element method. In this chapter first the transport equation for radiative heat transfer is derived, after which it is discretized using the discrete ordinate method. Special attention is paid to the treatment of the boundary conditions. At last some numerical tests for the radiation model are shown.

2.1 The general transport equation for radiation intensity

Consider radiation with a spectral intensity equal to $i_\lambda(S)$ (with λ denoting the wavelength dependency) travelling over a distance dS through an absorbing, emitting and scattering medium, as depicted in Figure 2.1. The decrease of radiation intensity due to absorption over distance dS equals

$$di_{\alpha,\lambda} = -\alpha_\lambda(S)i_\lambda(S)dS, \qquad (2.1)$$

with $\alpha_\lambda(S)$ the medium absorption coefficient. When the medium is in local thermodynamical equilibrium, and $i_{b,\lambda}(S)$ is the medium black body intensity, then the increase of radiation intensity over distance dS by emission equals (Siegel and Howell, 1992):

$$di_{e,\lambda} = \alpha_\lambda(S)i_{b,\lambda}(S)dS. \qquad (2.2)$$

Figure 2.1. Radiation travelling over distance dS through volume dV of a medium.

The radiation intensity along path coordinate S is decreased by an amount of radiation which is scattered out of the volume dV. It is also increased by an amount of radiation intensity which is scattered into the volume dV along S from the surrounding environment. The netto change of radiation intensity by scattering therefore equals

$$di_{s,\lambda} = -\sigma_{s,\lambda}(S)i_\lambda(S)dS + \frac{\sigma_{s,\lambda}dS}{4\pi}\int_{\omega_i=0}^{4\pi} i_\lambda(S,\omega_i)\Phi(\lambda,\omega,\omega_i)d\omega_i . \qquad (2.3)$$

In this equation, σ_s is the scattering coefficient and $\Phi(\lambda,\omega,\omega_i)$ is the so called phase function for scattering from solid angle ω_i to solid angle ω. From the equations (2.1), (2.2) and (2.3) the total change of radiation intensity along the curve coordinate S is determined to be

$$\frac{di_\lambda}{dS} = -\alpha_\lambda i_\lambda(S) + \alpha_\lambda i_{b,\lambda}(S) - \sigma_{s,\lambda}i_\lambda(S) + \frac{\sigma_{s,\lambda}}{4\pi}\int_{\omega_i=0}^{4\pi} i_\lambda(S,\omega_i)\Phi(\lambda,\omega,\omega_i)d\omega_i . \qquad (2.4)$$

Equation (2.4) is known as the transport equation for radiation intensity. It is a so called "integro differential equation", as i_λ is a part of the integral in the right hand side scattering term.

Grey and non-scattering media

For a grey, non-scattering medium, the medium properties are not wavelength dependent and $\sigma_s = 0$ [m^{-1}] (Siegel and Howell, 1992). The transport equation for radiation intensity (2.4) reduces to

$$\frac{di(S)}{dS} = \alpha\left(i_b(S) - i(S)\right), \tag{2.5}$$

with α the Planck mean absorption coefficient, defined as

$$\alpha = \frac{\int\limits_{\lambda=0}^{\infty} \alpha_\lambda i_{b,\lambda} d\lambda}{i_b}. \tag{2.6}$$

In this equation the integrated black body intensity i_b over all wavelengths is defined as

$$i_b = \int\limits_{\lambda=0}^{\infty} i_{b,\lambda} d\lambda = \frac{\sigma T^4}{\pi}. \tag{2.7}$$

The transport equation for radiation intensity contains two unknowns, which are the directional intensity i along S and the medium black body intensity i_b. In order to solve the unknowns an additional equation is required, which determines a relation between i and i_b. This equation is the energy equation of the medium.

2.2 The energy equation including radiative fluxes

The transient energy equation without viscous dissipation and including radiative fluxes can be written as:

$$\rho c_p \frac{DT}{Dt} = \underline{\nabla} \cdot \left(k \underline{\nabla} T - \underline{q}_{rad}\right), \tag{2.8}$$

with ρ the density, c_p the heat capacity, T the temperature and k the conduction coefficient of the medium. The vector $\underline{q}_{rad}$ represents the radiative heat flux and t denotes the time. The divergence of the radiative flux equals

$$\underline{\nabla} \cdot \underline{q}_{rad} = \int\limits_{\omega=0}^{4\pi} \frac{di}{dS} d\omega. \tag{2.9}$$

Integrating the transport equation for radiative intensity (equation (2.5)) over ω, and combining the result with equation (2.9), yields

$$\underline{\nabla} \cdot \underline{q}_{rad} = \int\limits_{\omega=0}^{4\pi} \alpha\left(i_b(S) - i(S,\omega)\right) d\omega. \tag{2.10}$$

As the integrated black body intensity over all wavelengths is not dependent on ω, this equation simplifies to

$$\underline{\nabla} \cdot \underline{q}_{rad} = 4\pi\alpha\left(i_b - \bar{i}\right), \tag{2.11}$$

with

$$\bar{i} = \frac{1}{4\pi} \int\limits_{\omega=0}^{4\pi} i(\omega) d\omega. \tag{2.12}$$

Substituting the expression for $\underline{\nabla} \cdot \underline{q}_r$ in the energy equation, (2.8) can be written as

$$\rho c_p \left(\frac{\partial T}{\partial t} + \underline{u} \cdot \underline{\nabla} T\right) = \underline{\nabla} \cdot k \underline{\nabla} T - 4\pi\alpha\left(i_b - \bar{i}\right), \tag{2.13}$$

which gives the required relation between i and i_b. For problems involving only radiation, the equation reduces to

$$i_b = \bar{i}. \tag{2.14}$$

2.3 The discrete ordinate method

In the previous section, the transport equation for radiation intensity was derived. This equation describes the change of radiation intensity along a certain path length through the medium. As radiation travels along a path in space in any direction, the number of directions in which the radiation intensity can be derived is infinite. In order to calculate an intensity distribution, only a discrete number of directions is solved, and the radiation intensity is discretised over this set of directions (ordinates). This way of discretisation is known as the discrete ordinate method.

For a non-scattering, grey medium equation (2.5) holds

$$\frac{d i(S)}{d S} = \alpha \left(i_b(S) - i(S) \right).$$
$$(2.5)$$

In a general coordinate system, this equation is written as

$$-\underline{\zeta} \cdot \underline{\nabla} i = \alpha \left(i - i_b \right).$$
$$(2.15)$$

with $\underline{\zeta}$ the direction vector. For a 3-*D* Cartesian coordinate system, this direction vector is derived in appendix 1. This transport equation for radiation intensity can be solved using the discrete ordinate method. The hemispherical solid angle is discretized into *M* ordinates, each having a typical number *m* and a corresponding solid angle ω_m. The orientation of ordinate *m* is determined by the corresponding direction vector $\underline{\zeta}_m$. The intensity in ordinate *m*, i_m, is supposed to be constant inside the solid angle ω_m. The transport equation for radiation intensity for ordinate *m* is now derived by integrating (2.15) over the solid angle ω_m. Then after rearranging the terms in the equation one finds

$$-\underline{\xi}_m \cdot \underline{\nabla} i_m = \alpha \left(i_m - i_b \right), \qquad\qquad m = 1 .. M \quad (2.16)$$

with $\underline{\xi}_m$ equal to

$$\underline{\xi}_m = \omega_m^{-1} \int\limits_{\omega_m} \underline{\zeta} d\omega. \qquad\qquad m = 1 .. M \quad (2.17)$$

Equation (2.16) forms a set of *M* equations with *M* + 1 unknowns. However, combined with the energy equation and the Navier-Stokes equations a solvable set of equations is formed. This can be used to solve the intensities, the velocities and the temperatures.

Plane discrete ordinate method with $\alpha = 0$

The muffle of an industrial conveyor belt furnace is usually filled with nitrogen, which is a non absorbing nor scattering medium. Therefore in a real furnace a situation with $\alpha = 0$ and $\sigma_s = 0$ occurs. For this situation, the discrete ordinate equations (2.16) are simplified to

$$\underline{\xi}_m \cdot \underline{\nabla} i_m = 0. \qquad\qquad m = 1 .. M \quad (2.18)$$

Remember that though no radiation is absorbed or emitted by the medium, there is still radiative transfer between the furnace walls and the different objects in the furnace. Though equation (2.18) looks very simple, the complexity of the radiation problem is mainly determined by the boundary conditions at the walls, which will be discussed later.

As mentioned in section 1.3, a 2-*D* (two-dimensional) cross-sectional model is preferred for calculating the heat fluxes in the furnace. As radiation is in principle always 3-*D*, it cannot just be solved as a 2-*D* phenomenon. However, by taking into account some conditions, a semi 2-*D* approach can be used in solving the radiation problem, which is from now on referred to as a plane radiation approach.
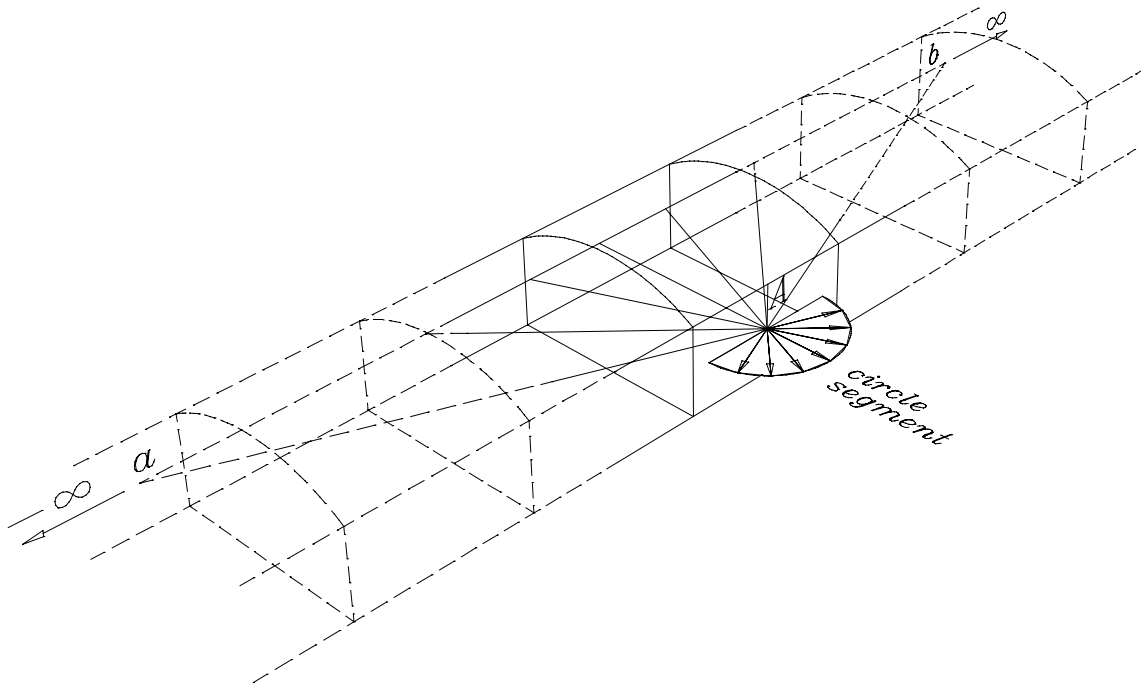
Figure 2.2. Radiation in an infinitely long muffle.

Plane radiation problems consist of radiation in infinitely long tubes, where the radiation intensity does not vary in axial direction. As mentioned, the muffle is a relatively long tube compared to its cross-sectional dimensions, and a semi 2-*D* approach is used for the radiation problem in the muffle. The radiation problem in an infinitely long muffle is depicted in Figure 2.2. As in axial direction no variations in cross-sectional shape and boundary conditions occur, the radiation intensity that is sent out from the line *a-b* is constant.

In the case of a real furnace, the muffle contains a non absorbing medium, and therefore, the radiation intensity remains constant while passing through the medium. All the radiation originating from line *a-b* falling on point *A* is enclosed by a circle segment as indicated in Figure 2.2. This implies that the incident radiation in that circle segment at point *A* is constant. Therefore the ordinates in a plane radiation approach can be shaped as depicted in Figure 2.3. The ordinates are numbered from $m = 1 .. M$. The azimuthal angle φ in the cross-sectional plane must be discretized, while the polar angle ϑ is integrated from 0 to π [rad].

In Figure 2.4 a 2-*D* representation of plane ordinates in the muffle geometry is shown. Plane ordinates can be defined by a direction vector ζ_m and two bounding vectors ζ_m^+ and ζ_m^-. The radius of the segments drawn
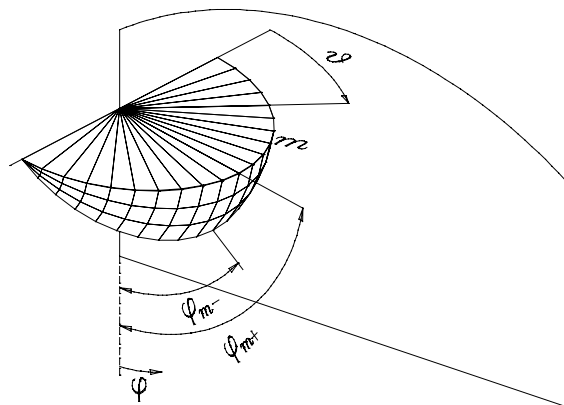
Figure 2.3. Plane ordinate inside the 2-D muffle geometry.

in the figure can be used as a measure for the radiation intensity in that direction.

When the set of discrete ordinates used is known, the integration in equation (2.17) can be carried out. The results for a general 3-*D* ordinate and for a plane ordinate as used in the furnace are shown in appendix 2.

2.4 Boundary conditions

Since the discrete ordinate equations are first order linear differential equations, only one boundary condition along a path coordinate S in direction ζ_m is needed. As boundary condition, for each ordinate m the intensity is prescribed at the walls where

Figure 2.4. Two-dimensional representation of a plane ordinate in the muffle.

direction ζ_m is originating from. The intensity coming from a wall consists of emitted and reflected intensity. The emitted radiation from a wall depends on the wall temperature. The reflected intensity at a wall depends on the intensity field inside the medium and the reflective properties of the wall.

General radiation behaviour at walls

Consider a certain amount of radiative intensity i_{in} incident to a wall. The radiation will partly be absorbed or reflected at the wall, and partly be transmitted through the wall, as depicted in Figure 2.5. The part of the radiation which is absorbed equals

$$i_{a_w} = \alpha_w i_{in_w}, \qquad (2.19)$$

with α_w the absorption coefficient of the wall, and i_{in_w} the intensity of the incident radiation at the wall. For a wall reflection coefficient ρ_w the reflected part of the radiation intensity equals

$$i_{r_w} = \rho_w i_{in_w}. \qquad (2.20)$$

The transmitted part at last equals

$$i_{t_w} = \tau_w i_{in_w}, \qquad (2.21)$$

Figure 2.5. Incident radiation at a wall.

with τ_w the transmission coefficient of the wall. As the incident radiation to a wall will be either absorbed, reflected or transmitted, the following relation for the coefficients always holds

$$\alpha_w + \rho_w + \tau_w = 1. \qquad (2.22)$$

For an opaque wall there will be no transmission, hence $\tau_w = 0$. All incident radiation will be either absorbed or reflected, and equation (2.22) reduces to

$$\alpha_w + \rho_w = 1. \qquad (2.23)$$

The wall will also emit a certain amount of radiation, which equals

$$i_{e_w} = \varepsilon_w i_{b_w}. \tag{2.24}$$

If the wall is a grey body in thermodynamic equilibrium, then

$$\alpha_w = \varepsilon_w. \tag{2.25}$$

The general equations derived in this section will be used to determine the boundary conditions for the discrete ordinate equations. Therefore the equations need to be discretized over the discrete ordinate directions. For example the emitted intensity from a wall depends on the emission coefficient of the wall, as given in equation (2.24). Assuming diffuse emission, the emitted intensity from wall w is equal in all outgoing directions m', and can be calculated directly from equation (2.24) for each incoming ordinate m:

$$i_{e_{w,m'}} = \varepsilon_w i_{b_w} = \frac{\sigma \varepsilon_w T_w^4}{\pi}. \qquad m' = 1 .. M \tag{2.26}$$

The reflection at the walls is more complicated and is treated in the next section.

Reflection at the walls

Introduction

With the reflection coefficient ρ_w at the wall the reflected intensity for every incoming ordinate m can be derived as in equation (2.20), giving:

$$i_{r_{w,m}} = \rho_w i_{in_{w,m}}. \qquad m = 1 .. M \tag{2.27}$$

In general the reflection characteristic of a wall is a mixture of partly specular and partly diffuse reflection, as depicted in Figure 2.6. Therefore, the reflected intensity into an outgoing ordinate m' depends on reflective properties of the wall.
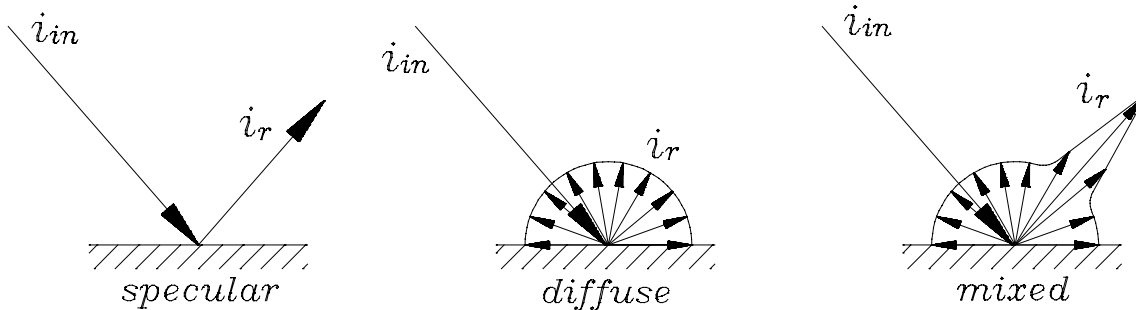
Figure 2.6. Specular, diffuse and mixed reflection against a wall.

Furthermore, the reflected intensity depends on the orientation of the wall with respect to the set of ordinates. Some ordinates will only partly fall in to the wall, as depicted in Figure 2.7. From these ordinates a smaller amount of energy falls in to the wall than from completely striking ordinates. As this amount of energy is not neccessarily reflected to an equally sized outgoing ordinate, the intensities cannot be used directly in the calculations. One has to calculate the amount of incoming energy to the wall from every ordinate, and divide this energy over the outgoing ordinates, while taking into account the reflective properties of the wall. For dividing the energy over the reflected ordinates, several coefficients must be defined.

The boundary coefficients

As mentioned, in the discrete ordinate method the hemispherical solid angle is divided into M solid angles ω_m, and the amount of incoming intensity from a solid angle to a wall depends on the orientation of the solid angle to that wall. In Figure 2.7 a 2-*D* projection of an ordinate m falling in to wall w is depicted (see also Figure 2.4). The part of the solid angle that falls in to the wall is defined as the boundary coefficient $c_{w,m}$ of the wall and that solid angle. Therefore, the part of the energy in the ordinate that falls in to the wall equals $c_{w,m}$, and the part that does not hit the wall equals $1 - c_{w,m}$. The derivation of the boundary coefficients is explained in more detail in appendix 3.
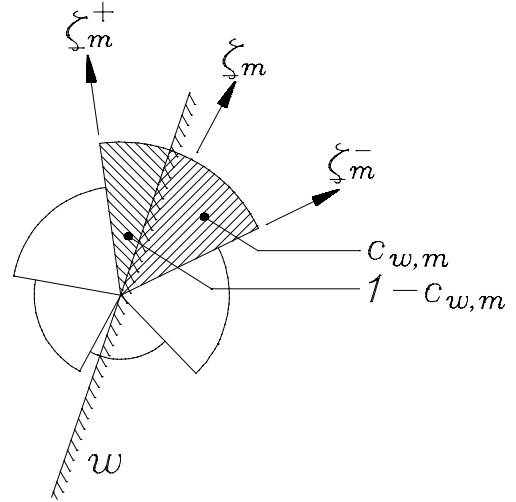
Figure 2.7. Parts of an ordinate that are incident to and coming from wall w.

The mirror coefficient of a wall

For characterisation whether a wall is specularly or diffusively reflecting, a mirror coefficient s_w is defined. This coefficient is equal to the part of the energy that is reflected specularly at the wall. The reflected energies from an incoming ordinate m can then be derived as

$$q_{r,spec_m} = s_w q_{r_m} \, , \qquad\qquad m = 1 .. M \quad (2.28)$$

$$q_{r,dif_m} = \left(1 - s_w\right) q_{r_m} . \qquad\qquad m = 1 .. M \quad (2.29)$$

The reflected energy from ordinate m can in turn be calculated using the wall reflection coefficient. Analogous to equation (2.20) it follows that

$$q_{r_m} = \rho_w q_m . \qquad\qquad m = 1 .. M \quad (2.30)$$

Calculation of the reflected intensity

The reflected intensity to ordinate m' is calculated by dividing the reflected energy by the solid angle $\omega_{m'}$ corresponding to ordinate m'

$$i_{r_{m'}} = \frac{q_{r_{m'}}}{\omega_{m'}} . \qquad\qquad m' = 1 .. M \quad (2.31)$$

The reflected energy to ordinate m' can be calculated by summation of all specularly and diffusively reflected energies from all incoming ordinates m

$$q_{r_{m'}} = \sum_{m=1}^{M} \left(q_{r,spec_{m \to m'}} + q_{r,dif_{m \to m'}} \right) . \qquad\qquad m' = 1 .. M \quad (2.32)$$

The specularly and diffusively reflected parts originating from ordinate m were already calculated using the equations (2.28) and (2.29). In order to determine how these parts are divided over the reflected ordinates m', two additional coefficients are defined, so that

$$q_{r,spec_{m \to m'}} = c_{spec,w_{m \to m'}} q_{r,spec_m} \, , \qquad\qquad m , m' = 1 .. M \quad (2.33)$$

$$q_{r,dif_{m \to m'}} = c_{dif,w_{m \to m'}} q_{r,dif_m} . \qquad\qquad m , m' = 1 .. M \quad (2.34)$$

The coefficients $c_{spec_{w,m \to m'}}$ and $c_{dif_{w,m \to m'}}$ depend on the boundary coefficients. The derivation of these coefficients is explained in appendix 4. Combining the equations (2.28) to (2.34), the

reflected intensity to ordinate m' can be derived.

$$i_{r_{w,m'}} = \frac{\rho_w \sum_{m=1}^{M} \left(c_{spec_{m \to m'}} s_w + c_{dif_{m \to m'}} \left(1 - s_w\right)\right) q_m}{\omega_{m'}} . \qquad m' = 1 .. M \quad (2.35)$$

For an evenly divided ordinate set, $\omega_{m'} = \omega_m$ and so it follows that

$$i_{r_{w,m'}} = \rho_w \sum_{m=1}^{M} \left(c_{spec_{m \to m'}} s_w + c_{dif_{m \to m'}} \left(1 - s_w\right)\right) i_m . \qquad m' = 1 .. M \quad (2.36)$$

2.5 Finite element model

As the discrete ordinate equations are differential equations, they can be solved using the finite element method. The geometry is divided into a certain number of elements. In the SEPRAN package (Segal, 1995) various standard elements are available, like linear and quadratic, square and triangular, and upwind elements. For approximating the integrated equations over the elements, a choice can be made between several numerical integration rules, like Newton-Cotes or Gauss schemes. For complex geometries the use of triangular elements is the most practical because of their high geometrical flexibility. In general it is not neccessary to use the same element mesh for the flow and the radiation problem. However, for simplicity in the present study all the equations are solved on the same mesh, using the same element density. As in the Navier-Stokes equations the derivative of the pressure is one degree less than those for the velocity, at least quadratic elements are preferred for solving the flow. For linearization of the Navier-Stokes equations Newton iterations are used. The solution is calculated by the penalty function method in combination with Crouzeix-Raviart elements (Cuvelier, 1986).

In the case that a combined convective/radiative problem is calculated, also for the radiation problem quadratic triangles are used. When only solving a radiation problem, one can also choose for linear elements. For the radiation problem, the choice whether or not to use upwind elements depends on the geometry, as will be shown in section 2.6. Also in this section the relation between the number of ordinates for discretizing the radiation and the mesh density will be mentioned, as well as the choice for the numerical integration scheme.

2.6 Numerical tests

Radiation between two infinite plates

As a first test case, the radiation problem between two infinite parallel plates is considered. The exact solution for the energy transfer between the plates is (Siegel and Howell, 1992)

$$q = \frac{\sigma\left(T_2^4 - T_1^4\right)}{\varepsilon_1^{-1} + \varepsilon_2^{-1} - 1}, \qquad (2.37)$$

with q the heat flux between the plates, T_1 and T_2 the plate temperatures and ε_1 and ε_2 the emission coefficients of the plates. Using
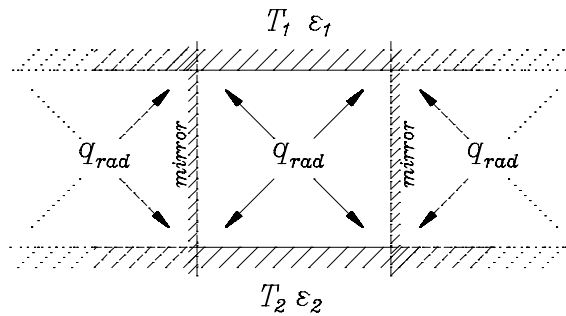

Figure 2.8. Radiation between two infinite plates.

ε_1	ε_2	q_{exact} [W/m^2]	$q_{calculated}$ [W/m^2]		
1.0	1.0	$1.7425565 \cdot 10^3$	$< 1.7425572 \cdot 10^3$	..	$1.7425546 \cdot 10^3 >$
0.75	1.0	$1.3069174 \cdot 10^3$	$< 1.3069180 \cdot 10^3$	..	$1.3069062 \cdot 10^3 >$
0.5	1.0	$8.7127827 \cdot 10^2$	$< 8.7127816 \cdot 10^2$	..	$8.7127875 \cdot 10^2 >$
0.25	1.0	$4.3563913 \cdot 10^2$	$< 4.3563913 \cdot 10^2$	..	$4.3564070 \cdot 10^2 >$
0.75	0.5	$7.4680994 \cdot 10^2$	$< 7.4689697 \cdot 10^2$	..	$7.4677029 \cdot 10^2 >$
0.5	0.5	$5.8085218 \cdot 10^2$	$< 5.8093657 \cdot 10^2$	..	$5.8076863 \cdot 10^2 >$
0.25	0.5	$3.4851131 \cdot 10^2$	$< 3.4856724 \cdot 10^2$	..	$3.4837574 \cdot 10^2 >$

Table 2. Exact and calculated values for the heat flux between two infinite plates.

the radiation model, this problem can be calculated as a cavity with mirroring side-walls. By placing two mirrors ($\varepsilon_w = 0$ [-] and $s_w = 1$ [-]) opposite to each other an infinite geometry is created (Figure 2.8). Several calculations have been performed with $T_1 = 200$ [℃] and $T_2 = 100$ [℃], using different values of the emission coefficients. In all the calculations, the geometry was divided into 236 quadratic triangular elements, resulting in a total of 513 nodal points. The radiation was discretized using 128 ordinates. For all the calculations the energy fluxes through the plates were calculated to be constant over the plate width, as could be expected from the symmetrical character of the problem. The calculated and exact values for several situations are given in Table 2. For the calculated heat fluxes two values are given, which are the values obtained at the two different walls. These values differ because of truncation errors when the desired relative accuracy of 10^{-5} is reached. The solution for $\varepsilon_1 = \varepsilon_2 = 0.5$ [-] is also plotted as the solid line in Figure 2.9. As can be seen in the table, a very good agreement is reached between the numerical radiation model and the exact solutions. Therefore it can be concluded that the implementation of the radiation model with the mirroring and diffusively reflecting walls can be trusted.

Specular versus diffuse reflection

The difference between specular and diffuse reflection can be shown using the same geometry as above, but with the mirroring side-walls replaced by diffuse reflectors ($\varepsilon_w = 0$ [-] and $s_w = 0$ [-]). For a situation with $\varepsilon_1 = \varepsilon_2 = 0.5$ [-] the calculated heat flux between the plates lies between 490 and 523 [W/m^2], as shown in Figure 2.9. The graph shows erratic values at the corner points of the cavity ($x = 0$ and $x = 1$). This occurs since the surface normal, which is used in the calculation of the heat flux, is undefined in a corner point. Therefore the values of the heat flux in the corners cannot be trusted. The flux is not constant over the plate width any more, which is expected since a diffuse reflector does not give a symmetric boundary condition like the

Figure 2.9. Heat flux through the plates for diffuse (dashed) and specular reflecting side-walls (solid).

mirror did. Furthermore, the heat flux values are lower than the value found with mirroring side-walls. This can be explained because opposite to the mirroring side-walls, the diffusely reflecting side-walls directly reflect radiation to the originating wall. So the hot

wall gets more radiation back, and the cold wall will get less radiation. Therefore the heat flux between the walls is lower with diffusely reflecting side-walls.

Number of ordinates versus mesh density

For solving the discrete ordinate equations, both a discretisation in space and in solid angle have to be made. In this section it is investigated whether the degrees of refinement of both discretisations are coupled. To this end, a pure radiation problem in the furnace geometry is considered. As the furnace contains a non-absorbing medium, a pure radiation problem is solved using the discrete ordinate equations (2.18) in combi-
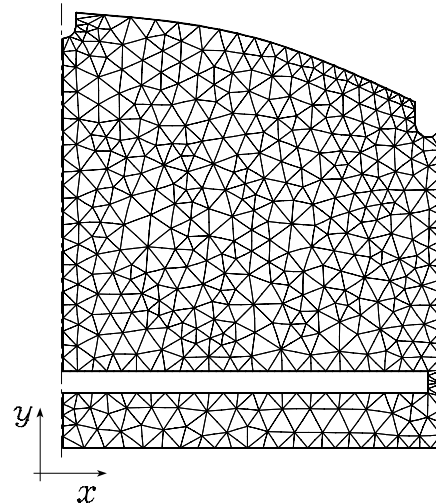
Figure 2.10. Furnace geometry and element mesh used in the radiation calculations.
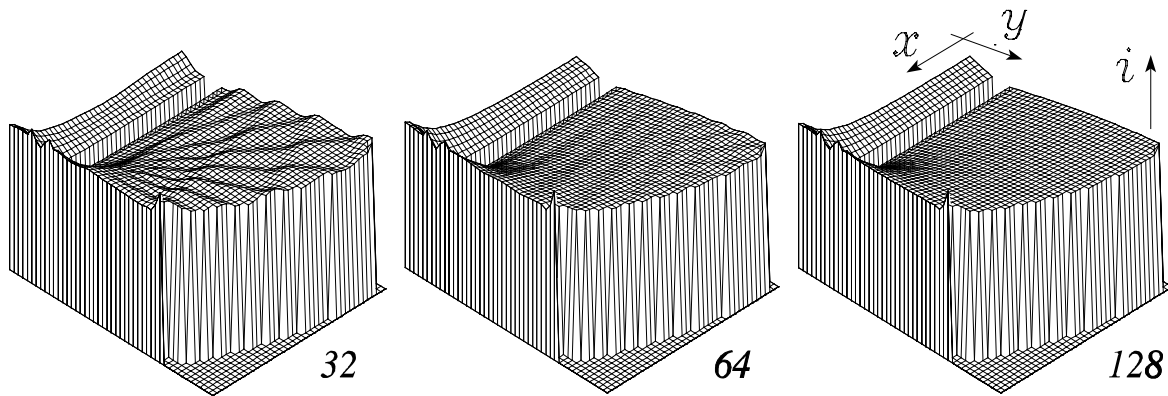
Figure 2.11. Calculated mean intensity fields for 32, 64 and 128 discrete ordinate directions.

nation with the reduced energy equation (2.14). The furnace geometry is symmetrical, so only half of the domain is calculated. The calculation domain is depicted in Figure 2.10. The walls on the left hand side (dashdotted line) are modelled as perfect mirrors in order to prescribe symmetrical boundary conditions. The geometry was divided into 891 quadratic triangular elements, which is also shown in Figure 2.10. All the walls except the symmetrical boundaries are modelled as black absorbers. The muffle walls were set to 400 [℃] and the belt was set to a uniform temperature of 100 [℃].

The radiation problem was solved using 32, 64 and 128 discrete ordinate directions. In Figure 2.11 for the three cases the mean intensity (equation (2.12)) is plotted, which
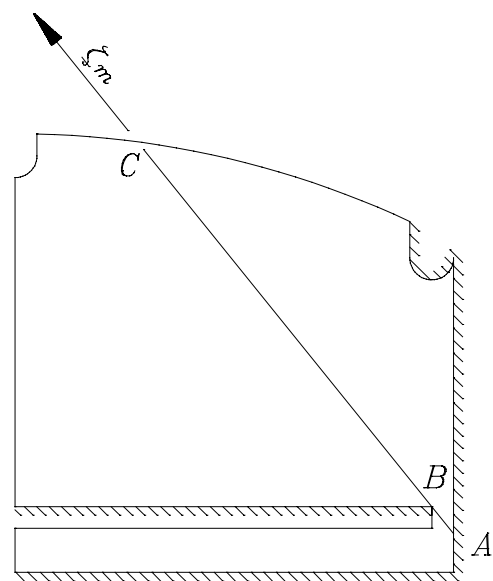
Figure 2.12. Direction ζ_m hitting a corner of the belt.

was simply calculated by adding up all directional intensities and dividing them by the total number of directions. As the heat fluxes at the walls are also calculated by adding the directional intensities, the averaged intensity field is comparable to a heat flux. As can be seen in the figure, only the calculation with 128 directions gives a smooth solution field, while for less directions oscillations appear.

The appearance of oscillations can be explained as follows. When calculating the intensity field in ordinate m, boundary conditions are prescribed on the walls radiation is coming from. For ordinate m as defined in Figure 2.12, these are the hatched walls. The intensity originating from the cold walls of the belt is lower than the intensity that is coming from the hot muffle walls. For directions that hit the inner facing corner of the belt, like direction ζ_m in Figure 2.12, in the part of the geometry at the left hand side of line *A-B-C* the intensity i_m will be determined by a cold wall of the belt, while in the part at the right hand side of the line the intensity is determined by the hot muffle walls. On line *B-C* the intensity field contains a discontinuity. The exact solution field for ordinate m is depicted in Figure 2.13. As the mean intensity fields shown in Figure 2.11 have been calculated by averaging the discontinuous intensity fields for all ordinates, the discontinuities in the ordinate intensities will show up as waves in the mean intensity field along all the ordinates used in the calculation. The more ordinates are used, the smaller the influence of one single discontinuous solution will be, and the smoother the mean intensity field will be.

Figure 2.13. Exact solution for the intensity in direction ζ_m.

The number of ordinates neccessary for calculating smooth average intensity fields depends on the mesh density. First of all, when the oscillations are smaller than the element width, they cannot appear in the finite element solution. Therefore, oscillations are avoided when the number of ordinates is so large that the maximum distance between two neighbouring ordinates containing discontinuities is less than the width of one element in every position of the mesh. As the distance between two ordinates increases for an increasing path length through the medium, the maximum distance between ordinates appears at the maximum path length. For the mesh used in the furnace calculations, the maximum distance the rays travel is from the upper right corner of the belt to the upper left corner of the muffle. The maximum distance between the discontinuities occurs in the upper left corner. When $\Delta\varphi_m$ equals the angle width of one ordinate, the distance between two neighbouring ordinates equals $\Delta\varphi_m \, S_{max}$ (Figure 2.14). For the distance approximately being equal to the width of an element Δx_{el}, the number of ordinates is
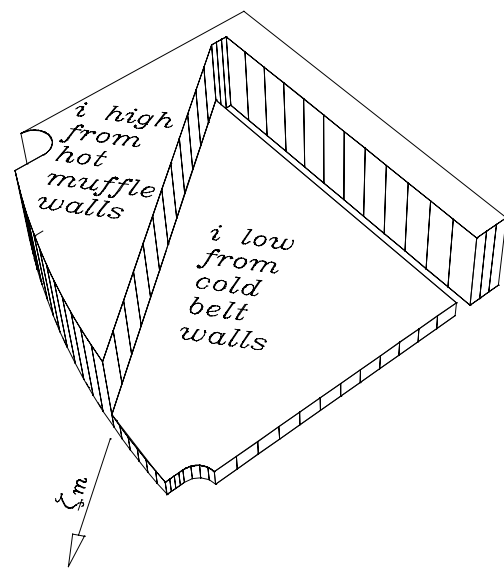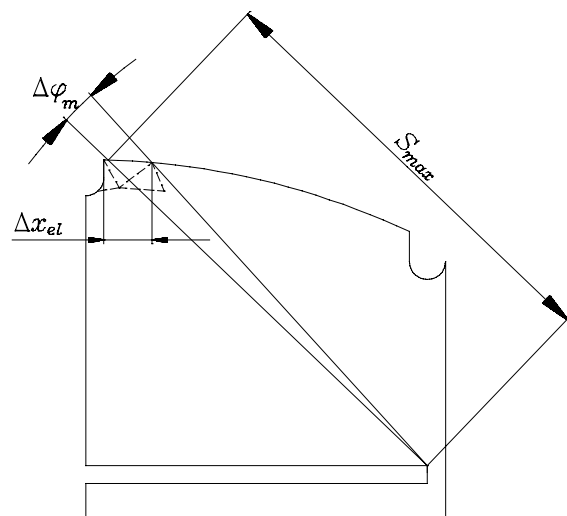

Figure 2.14. Global dimensions for calculating the theoretical minimum number of ordinate directions.

found from:

$$M = \frac{2\pi}{\Delta\varphi_m} \approx \frac{2\pi S_{max}}{\Delta x_{el}}.$$ (2.38)

For the mesh used in the furnace calculations (Figure 2.10), the value for *M* equals 212. As can be seen in Figure 2.11, already 128 ordinates appeared to be enough to calculate a smooth solution.

The fact that the number of ordinates needed in practice is smaller than the theoretical amount of equation (2.38), can be explained as follows. When solving the discrete ordinate equations using the finite element method, the solution fields may contain discontinuities as shown in the exact solution. However, on a mesh with a finite number of elements a discontinuity will be smeared out over some region. How much the discontinuity is smeared out depends on the integration and discretization schemes used in the calculation. Various discretization schemes have been investigated in literature (Liu, Becker and Pollard, 1996). An upwind discretization scheme will smear out the discontinuity over a relatively large distance, while a scheme without upwind will give a better approximation of the exact solution. Also a finer mesh or a higher order integration scheme will give a better approximation of the discontinuous solution. The integration scheme used also depends on the type of elements used. A Newton Cotes integration scheme in combination with quadratic elements causes a singular matrix (see appendix 5), but the more accurate Gauss integration scheme gives no problems. The effect of smearing out discontinuities will have a decreasing influence on the appearance of waves in the mean intensity fields. Test calculations show that the minimum required number of ordinates is about half the theoretical number, derived in (2.38). Therefore, for the radiation problem in the furnace, the mesh of Figure 2.10 is chosen to be combined with 128 ordinates.

Radiation in concave geometries

In literature, several discretization schemes are used in combination with the discrete ordinate method (Liu, Becker and Pollard, 1996). From this study it appears that for concave geometries an upwind scheme must be used to avoid oscillations in the solution field around inner facing corners. The furnace geometry is typically a concave geometry because of the inner facing belt. The need for upwind elements is demonstrated by calculating a typical radiation problem in the furnace geometry. All walls are considered black surfaces, and the muffle temperature is set to 200 [℃] while the belt is set to 100 [℃]. The same mesh as in Figure 2.10 is used for the calculations. In Figure 2.15 and Figure 2.16 calculated solutions along an ordinate are shown. The solution in Figure 2.15 was calculated using standard (no upwind) elements, while the solution in Figure 2.16 was found using streamline upwind/Petrov-Galerkin elements (Brooks and Hughes, 1982), which are standard available in the SEPRAN package.

As seen, the solution field calculated without upwind elements contains a lot of oscillations, while the upwind solution is far better. The appearance of oscillations for non-upwind elements can be explained as follows. When calculating the intensity field in ordinate *m*, boundary conditions are prescribed on the walls where radiation is coming from. For an ordinate *m* these are the hatched walls in Figure 2.12. If ordinate *m* hits an inner facing corner of the geometry, like a corner of the belt as depicted in Figure 2.12, then on the line *A-B* two boundary conditions are prescribed. Since the discrete ordinate equations are first order differential equations, only one boundary condition must be prescribed for calculating the solution along an ordinate. The second boundary condition therefore causes the oscillations (see also appendix 6). In an upwind scheme the downstream boundary condition will get a low weight, causing the solution to be mainly determined by the upstream one. Still the upwind solution shows one oscillation near the discontinuity.

This will always appear because the finite element method is not capable of representing the exact solution, which is discontinuous as already mentioned in the previous section.
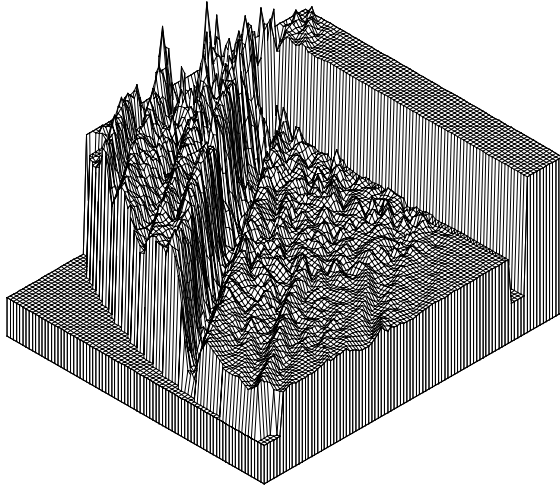

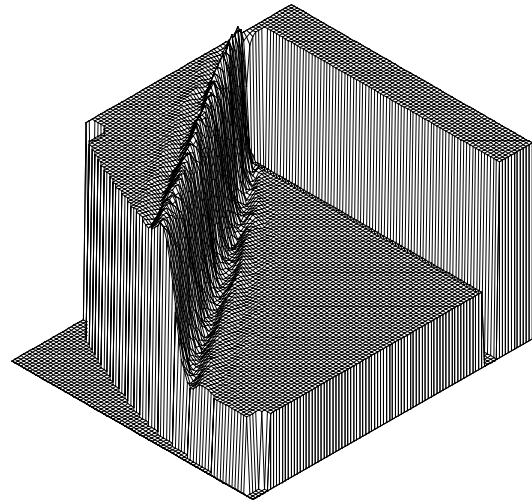*Figure 2.15. Solution calculated using standard elements.*

Figure 2.16. Solution calculated with upwind elements.

CHAPTER 3. THE FURNACE MODEL

Heat transfer in conveyor belt furnaces can be split into two basic phenomena. First of all, there is the heat transfer from the muffle to the belt with the products, which consists of radiation, conduction and convection through the medium inside the muffle. The second phenomenon is conduction through the belt and the products. Radiative heat transfer has already been dealt with in chapter 2. In order to describe the other phenomena appearing in the furnace their governing equations are described in the first sections of this chapter. In later sections, the coupling between the several phenomena and the structure of the furnace model are explained.

3.1 Governing equations

Radiation and energy transfer

The equations for radiation and energy transfer have already been discussed in the previous chapter. For the radiative transport the discrete ordinate equations for a non-absorbing medium will be used, which were derived to be

$$\underline{\xi}_m \cdot \underline{\nabla} i_m = 0. \qquad\qquad m = 1 \;..\; M \quad (2.18)$$

For non-absorbing media, the absorption coefficient $\alpha = 0$ and the general energy equation (2.13) reduces to

$$\rho c_p \left(\frac{\partial T}{\partial t} + \underline{u} \cdot \underline{\nabla} T \right) = \underline{\nabla} \cdot k \underline{\nabla} T. \qquad (3.1)$$

The Navier-Stokes equations for natural convection

The flow inside the furnace can be described by the Navier-Stokes equations. For calculating natural convection, the Boussinesq approximation is a very common method used in literature (Oberbeck, 1888). However, because temperature differences inside the muffle are relatively large, use of the Boussinesq approximation is not allowed and a fully temperature-dependent approach must be followed (Gray and Giorgini, 1976). The set of equations consists of the conservation laws for mass and momentum, given by

$$\frac{\partial \rho}{\partial t} + \underline{\nabla} \cdot (\rho \underline{u}) = 0, \qquad (3.2)$$

$$\frac{\partial (\rho \underline{u})}{\partial t} + \underline{\nabla} \cdot (\rho \underline{u}\, \underline{u}) = -\underline{\nabla} p + \underline{\nabla} \cdot \eta \underline{\nabla}\, \underline{u} + \rho \underline{g}. \qquad (3.3)$$

The second term in the left hand side of the momentum equation (3.3) can be written as:

$$\underline{\nabla} \cdot (\rho \underline{u}\, \underline{u}) = \underline{u}\, \underline{\nabla} \cdot (\rho \underline{u}) + \rho \underline{u} \cdot \underline{\nabla}\, \underline{u}. \qquad (3.4)$$

By combining equation (3.4) with the momentum equations, while also substituting the continuity equation, equations (3.2) and (3.3) can be reduced to:

$$\rho \left(\frac{\partial \underline{u}}{\partial t} + \underline{u} \cdot \underline{\nabla}\, \underline{u} \right) = -\underline{\nabla} p + \underline{\nabla} \cdot \eta \underline{\nabla}\, \underline{u} + \rho \underline{g}. \qquad (3.5)$$

As all the material parameters in the equations are in principle temperature-dependent, a coupling exists between the Navier-Stokes equations and the energy equation. Natural convection is therefore caused by gradients in material parameters throughout the medium.

Conduction through the belt

Like for the medium, also for the belt an energy equation can be derived. As the belt is made of steel, no convective or radiative heat transfer will occur, and a transient energy equation involving only conductive heat transfer remains:

$$\rho_b c_{p,b} \frac{\partial T_b}{\partial t} = \underline{\nabla} \cdot k_b \underline{\nabla} T_b \; .$$
(3.6)

In this equation ρ_b is the density, $c_{p,b}$ is the heat capacity and k_b is the conduction coefficient of the belt. All these parameters are assumed to be temperature independent, which is a good assumption for a metal belt.

3.2 Heat fluxes at the walls

Because the belt is heated up by radiative and convective heat fluxes coming from the medium, the transient conduction equation for the belt (equation (3.6)) is coupled to the radiation and convection equations for the medium (equations (2.18), (3.1) and (3.5)). Therefore, the radiative and convective heat fluxes at the belt surface must be calculated from the radiation and convection solutions in the medium.

The radiative heat flux

For determining the energy flux through an infinitesimally small surface dA on a wall, the projection dA_p of dA viewed from the solid angle $d\omega$ has to be determined. In Figure 3.1 the differential surfaces and the solid angle have been depicted. The dimensions of dA_p equal:

$$dx_p = dx \sin(\varphi), \; dy_p = dy \sin(\vartheta).$$
(3.7)

From this the area dA_p equals

$$dA_p = \sin(\varphi)\sin(\vartheta)dA .$$
(3.8)

The incident radiative power $Q_{rad,in}$ in [W] can be found by integrating the incident radiation intensity over the solid angle $d\omega$, giving:

$$Q_{rad,in} = \int_\omega i_{in_w} dA_p d\omega .$$
(3.9)

Figure 3.1. Incident solid angle $d\omega$ on a surface dA.

The incident energy flux $q_{rad,in}$ of the wall then equals:

$$q_{rad,in} = \frac{Q_{rad,in}}{dA} = \int_\omega i_{in} \frac{dA_p}{dA} d\omega .$$
(3.10)

As in the discrete ordinate method the solid angle is divided into M ordinates, each with a constant intensity i_m, the integral can be written as a summation of integrals over each solid angle ω_m, giving

$$q_{rad,in} = \sum_{m=1}^{M} i_{in_m} \int_{\omega_m} \frac{dA_p}{dA} d\omega .$$
(3.11)

The solid angle $d\omega$ as depicted in Figure 3.1 equals

$$d\omega = \sin(\vartheta)\, d\varphi\, d\vartheta, \qquad (3.12)$$

and for plane ordinates as depicted in Figure 3.2 then holds $0 \leq \vartheta \leq \pi$ and $(\varphi_m^- - \varphi_w) \leq \varphi \leq (\varphi_m^+ - \varphi_w)$. From the combination of equations (3.11) and (3.8) it follows that

$$q_{rad,in} = \frac{\pi}{2} \sum_{m=1}^{M} i_{in_m} \left(\cos\left(\varphi_m^- - \varphi_w\right) - \cos\left(\varphi_m^+ - \varphi_w\right) \right).$$

$$(3.13)$$

The net radiative heat flux is calculated by subtraction of the incident flux from the emitted heat flux:

$$q_{rad,net} = q_{rad,e} - q_{rad,in} = \sigma T^4 - q_{rad,in}. \qquad (3.14)$$

If the dimensionless energy flux is defined as

Figure 3.2. Plane ordinate at a wall.

$$q^* = \frac{q}{\sigma \Delta T T_0^3}, \qquad (3.15)$$

then the dimensionless energy flux can be calculated as

$$q_{rad,net}^* = \frac{T^4}{\Delta T T_0^3} - \frac{1}{2} \sum_{m=1}^{M} i_{in_m}^* \left(\cos\left(\varphi_m^- - \varphi_w\right) - \cos\left(\varphi_m^+ - \varphi_w\right) \right), \qquad (3.16)$$

with

$$i_{in_m}^* = \frac{\pi i_{in_m}}{\sigma \Delta T T_0^3}. \qquad (3.17)$$

The convective heat flux

The convective energy flux near a wall can be calculated using Fourier's law.

$$q_{c,in} = -k \left. \frac{\partial T}{\partial n} \right|_w, \qquad (3.18)$$

with $dT/dn|_w$ the temperature gradient perpendicular to the wall. Using the dimensionless heat flux as given in equation (3.15), the dimensionless energy flux by convection is derived to be

$$q_{c,in}^* = -\frac{k}{\sigma L T_0^3} \frac{\partial T^*}{\partial n^*}. \qquad (3.19)$$

Total heat flux

In order to calculate the total amount of heat added to the products or the belt in a time-step Δt the total amount of incident energy per unit length at a wall has to be calculated according to:

$$Q_{in}'^* = \int_{x^*} \left(q_{rad,net}^* + q_{c,in}^* \right) dx^*. \qquad (3.20)$$

3.3 Non-dimensionalization

The total system of equations involving radiative, conductive and convective heat transfer inside the furnace medium is given by the set of equations (3.2), (3.3), (2.13) and (2.5). For the belt, the transient conduction is described by equation (3.6). These equations can be written in nondimensional form using the following variables:

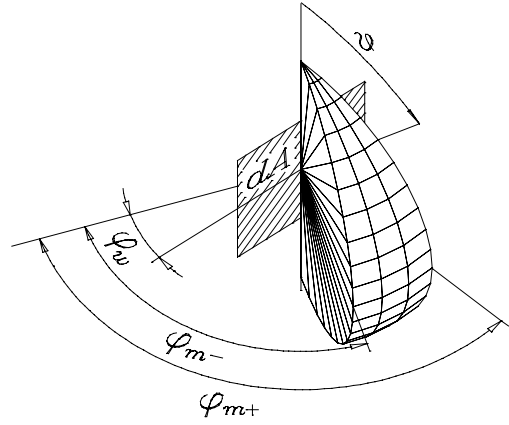$$\underline{u}^* = \frac{u}{U} \quad , \quad t^* = \frac{t}{\tau} \quad , \quad p^* = \frac{p - \rho_0 L g y^*}{\rho_0 U^2} \quad , \quad \underline{g}^* = \frac{\underline{g}}{g}$$

$$\underline{\nabla}^* = L \underline{\nabla} \quad , \quad i^* = \frac{\pi}{\sigma \Delta T T_0^3} i \quad , \quad T^* = \frac{T - T_0}{\Delta T} \quad . \tag{3.21}$$

The nondimensional set of equations for the medium now becomes:

$$Sr \frac{\partial (\rho / \rho_0)}{\partial t^*} + \underline{\nabla}^* \cdot \left(\frac{\rho}{\rho_0} \underline{u}^* \right) = 0, \tag{3.22}$$

$$\frac{\rho}{\rho_0} \left(Sr \frac{\partial \underline{u}^*}{\partial t^*} + \underline{u}^* \cdot \underline{\nabla}^* \underline{u}^* \right) = -\underline{\nabla}^* p^* + \frac{1}{Re} \underline{\nabla}^* \cdot \frac{\eta}{\eta_0} \left(\underline{\nabla}^* \underline{u}^* \right) + \frac{\rho - \rho_0}{\rho_0} \frac{\underline{g}^*}{Fr}, \tag{3.23}$$

$$\frac{\rho c_p}{\rho_0 c_{p,0}} \left(Sr \frac{\partial T^*}{\partial t^*} + \underline{u}^* \cdot \underline{\nabla}^* T^* \right) = \frac{1}{Pe} \underline{\nabla}^* \cdot \frac{k}{k_0} \left(\underline{\nabla}^* T^* \right) - \frac{1}{PeN} \left(i_b^* - \bar{i}^* \right), \tag{3.24}$$

$$\frac{d i^*(S^*)}{d S^*} = \alpha L \left(i_b^*(S^*) - i^*(S^*) \right). \tag{3.25}$$

For the belt, the nondimensional energy equation is

$$\frac{1}{Fo} \frac{\partial T_b^*}{\partial t^*} = \underline{\nabla}^* \cdot \underline{\nabla}^* T_b^*. \tag{3.26}$$

The nondimensional numbers used in the equations are defined as:

$$Re = \frac{\rho_0 U L}{\eta_0} \quad , \quad Pr = \frac{c_{p,0} \eta_0}{k_0} \quad , \quad Pe = Re Pr,$$

$$Sr = \frac{L}{U \tau} \quad , \quad Fr = \frac{U^2}{g L} \quad , \quad N = \frac{k_0}{4 \alpha \sigma T_0^3 L^2} \quad , \quad Fo = \frac{k_b \tau}{\rho_b c_{p,b} L^2}, \tag{3.27}$$

with *Re* the Reynolds number, *Pr* the Prandtl number, *Pe* the Péclet number, *Sr* the Strouhal number, *Fr* the Froude number, *Fo* the Fourier number and *N* a conduction-radiation parameter. *N* depicts the relative importance of conductive to radiative energy transport through the medium. For a non absorbing medium, this parameter approaches infinity. Then the last term in the energy equation vanishes, and the coupling via the medium between the radiation and the energy equation also disappears. However, the equations are still coupled via the boundary conditions at the walls. For a non-absorbing medium the equations (3.24) and (3.25) simplify to

$$\frac{\rho c_p}{\rho_0 c_{p,0}} \left(Sr \frac{\partial T^*}{\partial t^*} + \underline{u}^* \cdot \underline{\nabla}^* T^* \right) = \frac{1}{Pe} \underline{\nabla}^* \cdot \frac{k}{k_0} \left(\underline{\nabla}^* T^* \right), \tag{3.28}$$

$$\frac{d i^*(S^*)}{d S^*} = 0. \tag{3.29}$$

For a typical furnace problem as described in this study, the air temperatures can vary between 20 [℃] and 400 [℃] (see also Figure 3.8). The width of the muffle is used as reference length L, which is 344 [mm]. The value for the characteristic velocity U is set to 10^{-2} [m/s], which is the typical order of magnitude of the velocities occuring by natural convection. The value for the characteristic time $\tau = 10^4$ [s], which is the typical heating time for the belt. For the temperature ranges corresponding to two time levels in Figure 3.8 (t = 2000 [s] and t = 6000 [s]), the non-dimensional ratios appearing in the Navier-Stokes and the energy equations for the medium are given in the following table.

Non-dimensional number	t = 2000 [s] $\quad T_{muffle} \approx 80$ [℃], $T_{belt} \approx 20$ [℃].	t = 6000 [s] $\quad T_{muffle} \approx 380$ [℃], $T_{belt} \approx 280$ [℃].
$Sr\ \rho/\rho_0$	$4.2 \cdot 10^{-3}$	$4.1 \cdot 10^{-3}$
$Re^{-1}\ \eta/\eta_0$	$5.4 \cdot 10^{-3}$	$1.6 \cdot 10^{-2}$
$Fr^{-1}\ (\rho - \rho_0)/\rho_0$	$7.0 \cdot 10^3$	$6.2 \cdot 10^3$
$Sr\ (\rho\ c_p)/(\rho_0\ c_{p,0})$	$4.1 \cdot 10^{-3}$	$4.0 \cdot 10^{-3}$
$Pe^{-1}\ k/k_0$	$7.4 \cdot 10^{-3}$	$2.2 \cdot 10^{-2}$
Gr	$1.8 \cdot 10^8$	$2.0 \cdot 10^7$

Table 3. Typical values for the non-dimensional numbers in the furnace for a temperature history as in Figure 3.8.

The coefficient in the buoyancy term of the Navier-Stokes equation ($Fr^{-1}\ (\rho-\rho_0)/\rho_0$) can get relatively large, which points to strong buoyant effects. These occur utmost in the low temperature range, due to the material properties of air. As the flow may be unstable, it is expected that for low temperatures the Navier-Stokes solver will require small time steps in order to calculate an accurate flow field. For the region above the belt, a comparison is made to Henkes (1990) who calculated natural convection in a square cavity at different Ra numbers, with $Ra = Gr\ Pr$. Here Ra is the Rayleigh number and Gr the Grashof number, which is also given in Table 3. It can be simply derived that the buoyancy term used in this study for a linearly temperature-dependent density equals

$$\frac{\rho - \rho_0}{\rho_0}\frac{1}{Fr} = \frac{Gr\,T^*}{Re^2}. \tag{3.30}$$

From this equation Gr can be calculated, which corresponds to $Gr \approx 2 \cdot 10^8$ [-] for the low temperature range and $Gr \approx 2 \cdot 10^7$ [-] for the high temperature range. Remark that these values are independent of the chosen U-value. As $Pr = O(1)$, also the Rayleigh number will be $O(10^8)$ for the low temperature range. As determined by Henkes (1990) the flow in a square cavity tends to get unstable from this point. Although the situation in the furnace is slightly different from the situation in a square cavity, it is expected that also in the furnace the flow can get nearly unstable in the low temperature range. The Rayleigh-Bénard cells below the belt tend to get unstable from $Ra_D \approx 5 \cdot 10^4$ [-], with Ra_D based on the diameter D of the cells. In the furnace, D equals the space below the belt (≈ 20 [mm]). In the low temperature range, Ra_D nearly gets $5 \cdot 10^4$ [-], and the flow below the belt can get nearly unstable as well. Therefore, in the furnace model a very small timestep is taken for the flow calculation in the low temperature range.

For $\tau = 10^4$ [s] the coefficient $1/Fo$ in the transient conduction equation for the belt equals 2.8 [-]. As $1/Fo = Sr\ Pe$, also for the air a Fourier number can be calculated. For the typical furnace problem of Figure 3.8, $1/Fo_{air}$ varies between 0.1 [-] and 0.6 [-]. This shows that transient temperature fluctuations are weaker in the belt than in the medium. Therefore, for the conduction calculation in the belt a larger timestep can be used.

3.4 Marching procedure

In a real furnace, a 3-*D* heat transfer problem occurs. However, calculating 3-*D* heat transfer involving radiation, conduction and convection in a furnace is very complex and costs a lot of computing time and memory storage. As the muffle is a tube with a relatively large length compared to its cross-sectional dimensions, and as the axial temperature varies smoothly, heat transfer in a zone may be assumed to be nearly 2-*D*. In that case a 2-*D* model can be used to calculate the heat transfer in a cross-section. The temperature history of the products can then be calculated using a so called marching procedure. The furnace is marched through in a finite number of time-steps as depicted schematically in Figure 3.3. For each time-step the temperature, velocity and intensity fields are calculated in a 2-*D* cross-section. Then the heating rates for the belt and the product are calculated in order to determine their new temperatures. These new temperatures serve as input for the 2-*D* calculation at the next time-step, when the products and the belt have moved further into the furnace. The axial temperature profile of the muffle is taken into account by updating the boundary conditions for the muffle in each time-step. Additionally, 3-*D* heat transfer effects, as will be determined in chapter 5, determine extra source terms in the governing equations.
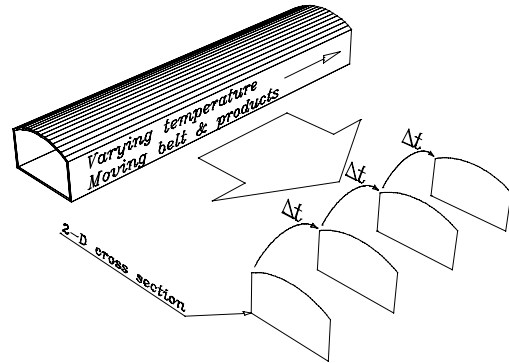
Figure 3.3. Dividing the furnace problem in a finite number of timesteps (marching procedure).

In Figure 3.4 the structure of the numerical model is depicted schematically. At the beginning of the calculation, the muffle, the medium and the belt are in an initial state, which determines the boundary conditions at time t_0. Using these boundary conditions, the discrete ordinate equations are solved to calculate radiative heat fluxes to the belt, while the convective heat fluxes are calculated by solving the Navier-Stokes equations and the energy equation. The boundary conditions for the discrete ordinate equations consist of emitted and reflected radiation intensities at the walls. As the reflected intensities depend directly on the incident intensities, they have to be calculated iteratively. Therefore, solving the discrete ordinate equations for given wall temperatures requires an iteration loop in which the reflection boundary conditions are updated. The numerical time-step suitable for solving the transient Navier-Stokes and energy equations may not be the same as the time-step used in the total marching procedure (Δt). Therefore, one marching time-step contains a time-loop in which the Navier-Stokes and the energy equations are solved. The calculated heat fluxes to the belt serve as boundary conditions for a transient conduction calculation for the belt. Just like for the Navier-Stokes and the energy equations, the time-step for this transient calculation is smaller than the marching procedure time-step, and an inner time-loop is used. At this point, the temperature field of the belt at $t + \Delta t$ is calculated. Furthermore, the muffle temperature follows a certain profile in time, and has changed over the timestep Δt. Using the new surface temperatures of the muffle and the belt, and the new velocity field for the medium, the boundary conditions for the discrete ordinate equations and for the Navier-Stokes and the energy equations are updated. Then the calculation of the next marching time-step Δt can start.
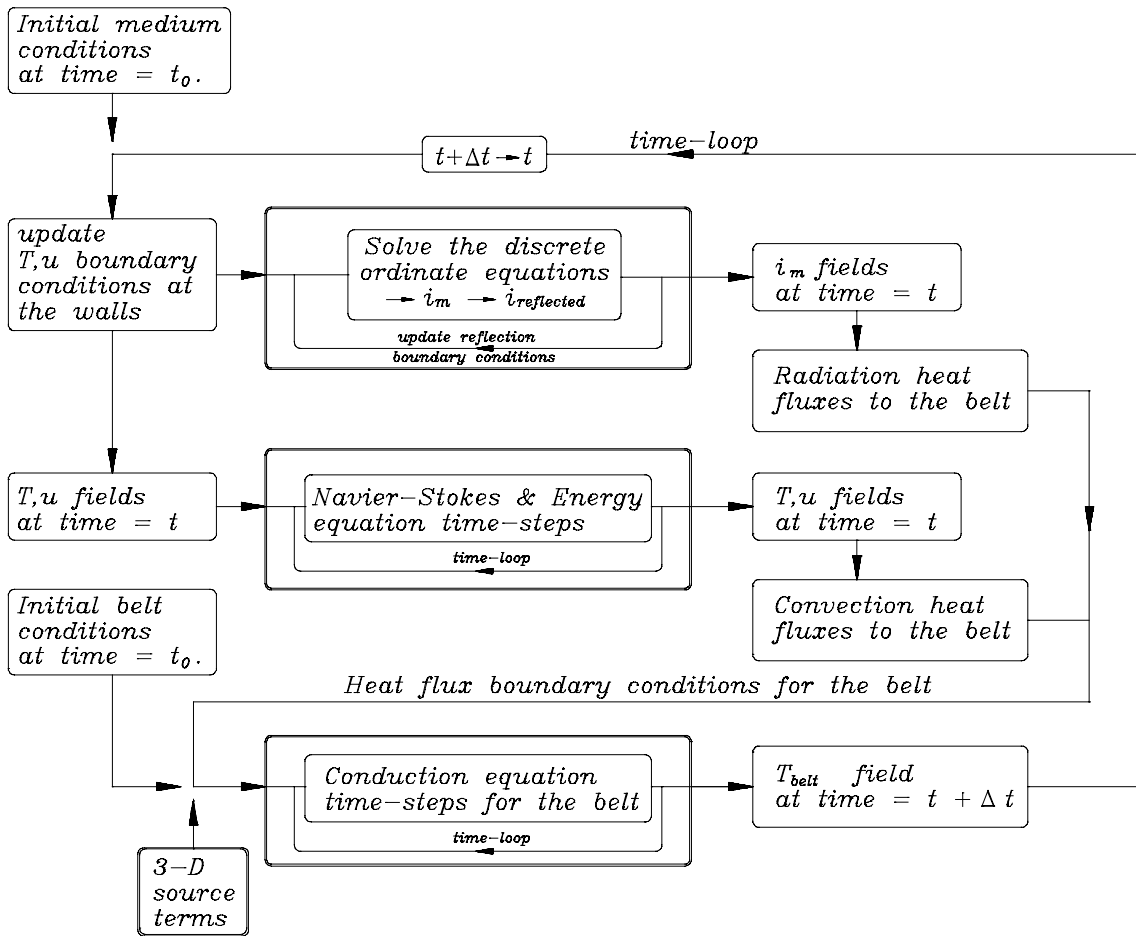
Figure 3.4. Flowchart of the furnace model.

The time-loop runs until the total amount of time which should be calculated is reached. When calculating a steady situation, the boundary conditions are kept at a determined level from a certain time-step, and the calculation will run until the difference between subsequent solution fields has become negligible.

3.5 Numerical tests

Boussinesq versus fully temperature-dependent approach

As mentioned in section 3.1, the Boussinesq approximation is not valid for solving natural convection in the furnace. In order to get an idea of the error in the Boussinesq solution, the flow field in a typical cross-section of the muffle was calculated using both the Boussinesq approximation and the completely temperature-dependent solver. The Boussinesq equations can easily be derived from the temperature-dependent equations ((3.22) to (3.24)) by setting all material properties to a constant value, except for the density in the gravity term of the Navier-Stokes equation (3.23). In the calculations a steady situation was considered with the muffle temperature put equal to 400 [℃] and with an assumed uniform belt temperature of 250 [℃].

In Figure 3.5 the streamlines of the flow inside the muffle calculated with the two different approaches are depicted. The solid lines correspond to the temperature-dependent solution, whereas the dashed lines depict the Boussinesq solution. As can be seen, differences

occur in the two velocity fields, as could be expected because of the high temperature differences inside the muffle.

For the furnace model it is important to know whether the two methods also give different results for the heat fluxes to the belt. In Figure 3.6 the calculated heat fluxes using the two methods are given. As can be seen, the heat flux calculated with the Boussinesq approximation is lower than the heat flux calculated with the temperature-dependent model. The relative difference between the heat fluxes is graphed in Figure 3.7, and appears to vary between 3% at the middle of the belt and about 2% near the side. These differences are not very high, but are not always negligible for critical production processes. As it also costs hardly any extra computing time, the full temperature-dependent approach will be used in the furnace model.
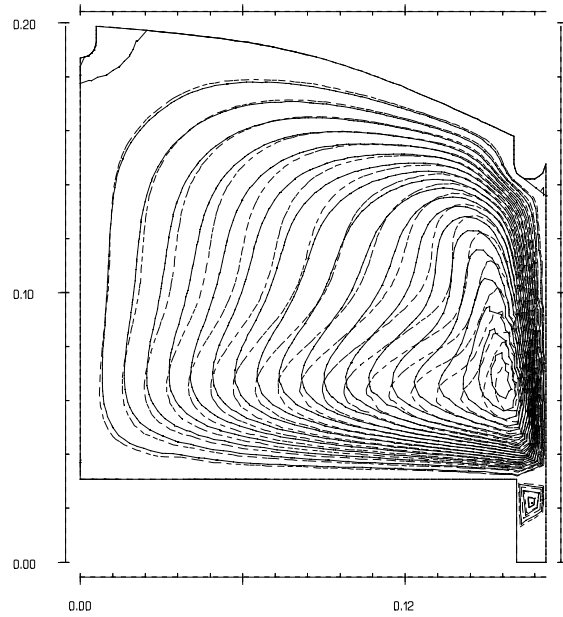

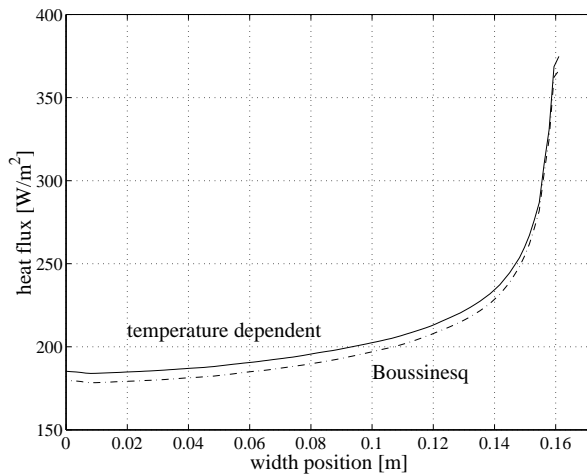*Figure 3.5. Comparison between Boussinesq (dashed) and temperature-dependent (solid) solutions.*

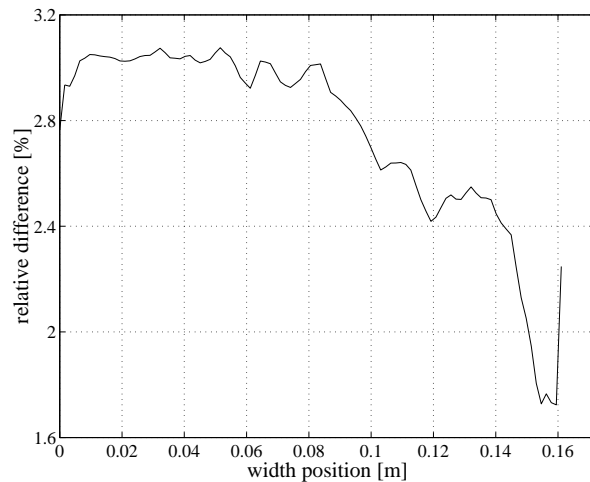*Figure 3.6. Convective heat fluxes to the belt with products for the two different approaches.*

Figure 3.7. Relative difference in heat fluxes to the belt.

Example of a furnace calculation

In this section a real furnace problem is calculated. In order to be able to compare the numerical results with a measurement, the prescribed muffle temperature profile in the calculation is equal to the measured temperature profile in the middle of the bottom of the muffle for measurement set 2 (see section 5.2). This temperature is relatively low compared to the muffle temperatures elsewhere in the muffle cross-section, but as the differences between the muffle temperature profiles are small, it is used as uniform muffle temperature in the calculation. Following this temperature profile the muffle is warmed from room temperature to a temperature of 400 [℃] with a ramp rate of 5 [℃/min], as show in Table 6 in

Figure 3.8. Muffle temperature profiles, and measured (dashdot) and calculated (solid) plate temperature profiles.

section 5.2. The properties of the muffle and the plates are given in appendix 7. By assuming symmetry in the middle of the muffle, only half the furnace has to be calculated. The half muffle geometry is divided into 3387 quadratic triangular elements, and the half belt is divided into 700 elements. For the marching procedure 100 time-steps are used, with each timestep divided into 3000 smaller time-steps for solving the Navier-Stokes equations. The temperature profiles of the product plates are calculated. In Figure 3.8 the muffle temperature history is plotted, together with the calculated and measured temperature histories of the product plate in zone 2. As can be seen in the figure, the measured and calculated temperature profiles of the plates agree quite well. In the measurement the plate heats up slightly faster than calculated. This can be explained because the muffle temperature in the measurement varies as a function of the cross-sectional position, while in the calculation a uniform (and relatively low) muffle temperature is prescribed.

In Figure 3.9 and Figure 3.10 the calculated temperature fields for the medium in the muffle are given at $t = 2000$ [s] and $t = 6000$ [s]. Both time levels are also indicated in Figure 3.8 by solid vertical lines, to show the positions on the temperature profile.
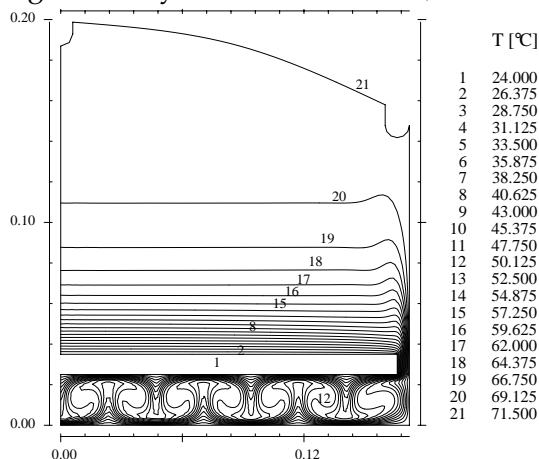
Figure 3.9. Temperature contour lines for the air inside the muffle at t = 2000 [s].
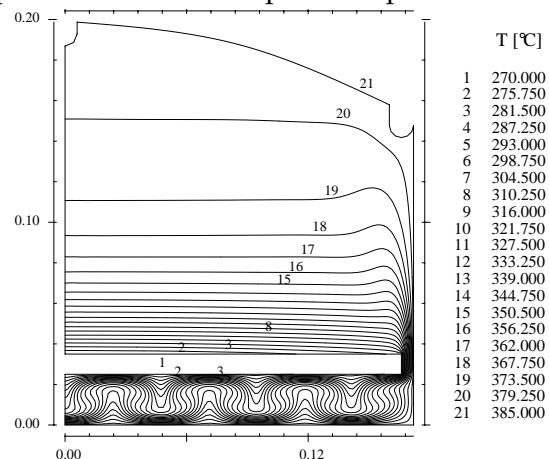
Figure 3.10. Temperature contour lines for the air at t = 6000 [s].

From the contour plots for the medium temperature it follows that the largest temperature gradients occur near the side of the product plate. The shape of the contour lines below

the product plate is caused by Rayleigh-Bénard convection, which gets less strong at higher temperatures, as also follows from the difference between Figure 3.9 and Figure 3.10. The contour lines near the top surface of the product plate are approximately parallel to the plate surface, which indicates that temperature gradients in width direction near the plate surface are relatively small.
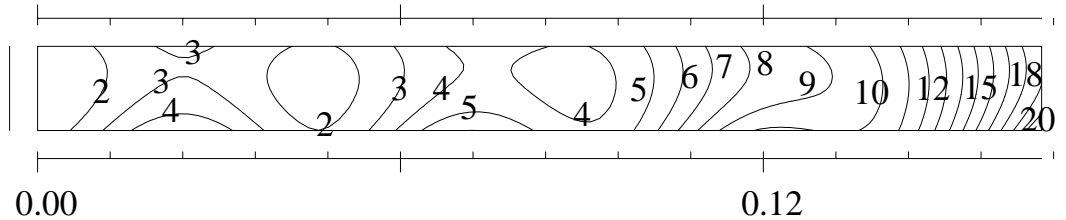
Figure 3.11. Temperature contour lines for the belt at t = 2000 [s]
(level 1, T = 25.20 [°C] and level 21, T = 26.45 [°C]).
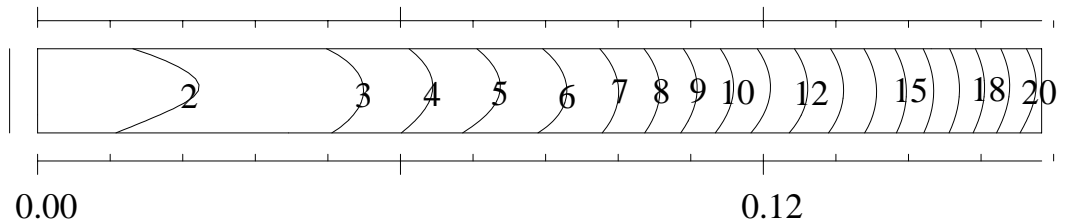
Figure 3.12. Temperature contour lines for the belt at t = 6000 [s]
(level 1, T = 279 [°C] and level 21, T = 292 [°C]).

In Figure 3.11 and Figure 3.12 the contour plots for the temperature of the product plate at t = 2000 [s] and t = 6000 [s] are depicted. The pattern of alternately occuring high and low temperatures in the central part of the belt at t = 2000 [s] is caused by the Rayleigh-Bénard convection. This is a very small effect, but it is visible in the contour plot because at this time the temperature in the central part of the belt is quite uniform. At t = 6000 [s] the influence of the heat fluxes from the side overrule the Rayleigh-Bénard effect, and the temperature gradients in the belt are much larger.
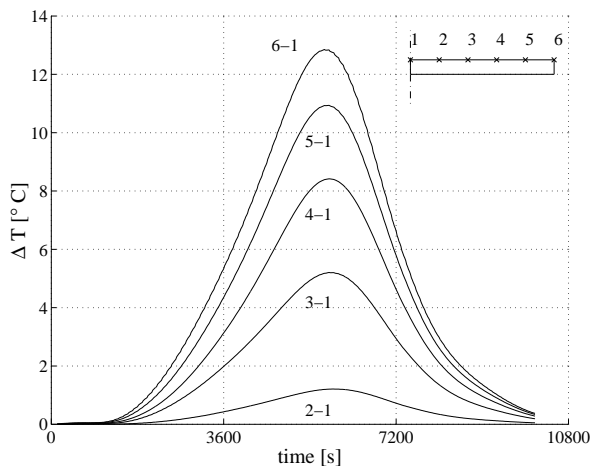
Figure 3.13. Calculated temperature differences compared to the middle of the belt.
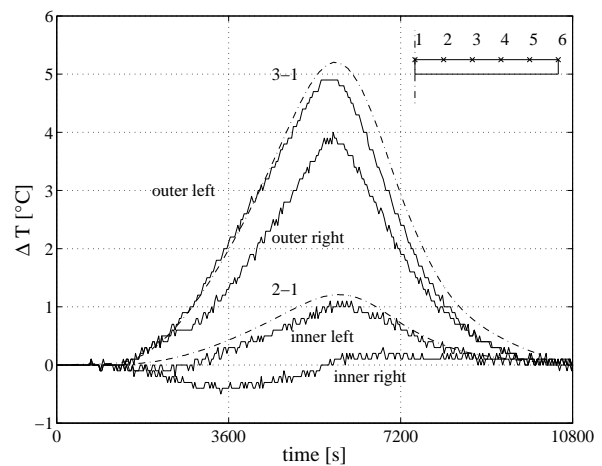
Figure 3.14. Measured (solid) and calculated temperature differences (dashdot).

In Figure 3.13 the temperature differences over the width of the belt compared to the temperature in the middle are plotted as a function of time. In the figure there are five graphs. The two lowest graphs correspond to positions of thermocouples in the experimental set-up (respectively 55 and 110 [mm] from the middle of the belt), and can therefore also be compared to measurements. The three higher graphs correspond to positions further to the side of the belt, being 138, 156 and 166 [mm] from the middle. The last point corresponds to the outer corner of the belt. As expected the temperature differences increase for positions further towards the side of the belt. The maximum temperature differences occur at t = 5900 [s]. In Figure 3.14 the calculated and measured temperature differences over the width of the belt are compared. The calculated temperature differences are plotted as dashdotted lines, and the measured temperature differences are plotted as solid lines. Since only half the furnace is considered (due to the assumption of symmetry), there are only two calculated temperature difference profiles, one for the outer and one for the inner thermocouple position. However, in the measurement the temperature distribution over the belt width was found to be non-symmetric. This is caused by a temperature difference between the left and the right side of the muffle. Therefore, four measured graphs are presented. The two lowest graphs correspond to the inner thermocouples, and the two highest graphs correspond to the outer thermocouples. As can be seen in the figure, a good agreement is reached between the model and the measurement.

It can be concluded that a 2-*D* model has been developed which is capable of calculating the temperature differences over the width of the belt with satisfactory accuracy. As it is a 2-*D* model, the influence of 3-*D* heat transfer effects will be analyzed in the next sections. Also the model is quite complex. Because of the large amount of time-steps necessary for calculating the flow phenomena the calculations cost a lot of computing time. Therefore, in the next sections further simplifications of the model will also be investigated, in order to make a design tool for fast furnace calculations.

CHAPTER 4. THE EXPERIMENTAL SET-UP

The experimental set-up has to serve two purposes. First the heat transfer phenomena inside the muffle must be analysed to validate the numerical model. Information is needed whether the flow inside the muffle is quasi-steady and symmetric, so that the used Navier Stokes solver is suitable for calculating the flow in the muffle. Besides, it has to be investigated whether the numerically predicted vortex structures actually appear inside the muffle. The second purpose of the experimental set-up is the determination of 3-D heat transfer effects. As these effects are taken into account separately in the numerical model by using source terms, an estimation of these effects is needed.

4.1 Design aspects

In order to validate the numerical model and to estimate 3-D effects, an experimental set-up is designed in which air temperatures as well as surface temperatures of the muffle and the belt with products can be measured. For investigating the flow properties, visualization is a suitable and very percepting technique. Therefore, a flow visualization system is designed. For determining 3-D effects the set-up must be capable of simulating both 2-D and a 3-D situations.

Muffle geometry

Because of cost limitations, the muffle is made of steel 310. Compared to the nickel-chromium alloy used in industrial conveyor belt furnaces, steel 310 is a lot cheaper, but also less temperature resistant. However, it can still be used for temperatures up to 600 [℃], which is assumed to be high enough for investigating the desired phenomena. Furthermore, the amount of zones is also limited due to cost aspects and the available electrical power in the laboratory. Hence, a length of 3 zones is chosen for the test-rig. The zones have equal dimensions as in a

Figure 4.1. Cross-sectional dimensions of the muffle.

real furnace, with a length of 300 [mm] and cross-sectional dimensions as depicted in Figure 4.1. Also the heating elements and the insulation package surrounding the muffle are the same as in an industrial conveyor belt furnace. The muffle temperatures for each zone are controlled using 3 PID controllers, one for the top, one for the bottom and one for the two sides. Using these controllers the muffle can be heated up smoothly to a certain set point temperature. They also can be configured to heat up the muffle with a user chosen ramp-rate, being the amount of degrees centigrade per minute temperature rise. The determination of the control parameters is discussed in section 4.3.

Because of the relatively short length of the muffle, the orifices at the ends could disturb the flow and temperature in the muffle much more than in a real conveyor belt furnace. In order to be able to prescribe a well defined situation in the muffle, the muffle ends will therefore be closed using so called 'head sides'. These are two heated plates that both have an own controller in order to prescribe their temperature. Because the muffle ends are closed, a conveyor belt cannot be used in the set-up. Therefore, the conveyor belt will be simulated as described in the next section.

Simulation of the belt speed

In a real conveyor belt furnace, the axial muffle temperature profile is prescribed by the different zone temperatures, as depicted by the (*T*,*x*)-graph in Figure 4.2. In order to create a certain product temperature history, the belt with the products is transported through this temperature profile while being pulled through the muffle. As a conveyor belt system is very expensive, and also the in- and outlet orifices would disturb the situation inside the muffle too much because of its short length, in the test-rig the conveyor belt is simulated in a special way. Instead of pulling a belt along a temperature profile, in the test-rig a temperature profile is pulled along the belt, while the belt is kept at a steady position.

Figure 4.2. Short test-rig 'walking along' a real conveyor belt furnace.

This is realized by varying the muffle temperature of the furnace in time, so that at each moment the axial temperature profile $T_{set-up}(t)$ in the test-rig equals a part of the total temperature profile of the real furnace at position $x_{set-up}(t)$ (Figure 4.2). In this way the belt and the products get the same temperature history as they would have in a real furnace.

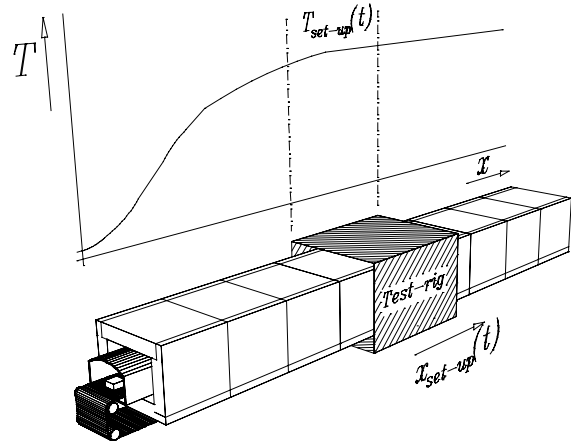By simulating the conveyor belt as described above, a cheaper and better conditionable test-rig can be built. However, the method of belt simulation causes an extra problem. In a conveyor belt furnace used in an industrial environment, the belt speed is usually about 180 [mm/min], and the axial temperature gradient between neighbouring zones can be about 150 [℃]. For a zone width of 300 [mm] a temperature gradient in time (ramp rate) of 90 [℃/min] is obtained for the belt with the products. In order to create an equivalent situation in the experimental set-up, the total test-rig must be heated with the same ramp rate. This costs a lot of extra energy, since in the test-rig not only the belt with the products is heated. Also the muffle and the heating elements with the stones and the insulation package need to be heated, which all have a large heat capacity. Therefore the maximum possible ramp rate for the test-rig is probably much lower than the value obtained in a real furnace. In order to deal with this difference, the influence to the heat transfer will be analysed, and consequences with respect to the conveyor belt used in the test-rig will be determined.

Temperature differences between the muffle and the belt with products cause heat transfer in the furnace. As the temperature differences between the muffle and the belt or plates must be the same for the real furnace and for the test-rig, also for both situations the heat transfer must be the same. In a real furnace the heat transfer between the muffle and the belt is in equilibrium with the transient heating of the belt. Assuming that heat transfer between the muffle and the belt is pure radiative, this means that

$$\sigma \varepsilon_b A_b F\left(T_m^4 - T_b^4\right) = m_b c_{p,b} \frac{\partial T_b}{\partial t}. \tag{4.1}$$

In this equation ε_b and A_b are the emission coefficient and the heat exchanging surface of the belt respectively. F is a configuration factor, T_m and T_b are the muffle and belt temperatures, m_b is the mass and $c_{p,b}$ the specific heat capacity of the belt. For the test-rig, an equivalent equilibrium exists, and a similar relation can be derived. In order to be able to vary properties in an easy way, the belt of the real furnace is modelled by product plates in the test-rig. These are steel plates with similar dimensions as the original belt, but with

a thickness which will be determined by the heat transfer phenomena. The heat transfer equation for the test-rig becomes

$$\sigma \, \varepsilon_p A_p F \left(T_m^4 - T_p^4 \right) = m_p c_{p,p} \frac{\partial T_p}{\partial t} \; , \tag{4.2}$$

with subscript p denoting the plate properties. For an equivalent situation in the test-rig compared to the real furnace, T_p and T_b should be equal all the time. From a combination of the equations (4.1) and (4.2) it follows that

$$\frac{m_b c_{p,b}}{\varepsilon_b A_b} \frac{\partial T_b}{\partial t} = \frac{m_p c_{p,p}}{\varepsilon_p A_p} \frac{\partial T_p}{\partial t} , \tag{4.3}$$

where the configuration factor F has been assumed to be equal for both situations because of the almost equal dimensions of the belt and the plates. As both the plates and the belt are made of some kind of steel, the values for the specific heat capacities can be assumed to be approximately equal. However, a conveyor belt used in practice has a larger heat exchanging surface due to its woven structure, which will also cause radition to be absorbed more effectively. Therefore, it can be posed that

$$\left(\varepsilon A \right)_b = \zeta \left(\varepsilon A \right)_p \; , \tag{4.4}$$

with $\zeta > 1$. The woven structure of a real conveyor belt is depicted in Figure 4.3. The spacing between the wires (d) is about equal to the wire diameter (about 3 [mm]). There-fore, the heat exchanging surface of a con-veyor belt equals about twice the surface of a flat plate. Furthermore, radiation will be absorbed better because of the open struc-ture. As the absorption coefficient of the belt material lies between 0.4 and 0.6 [-], an increase in absorption with a factor 1.5 looks reasonable. Therefore, the value of ζ is estimated to be equal to 3. With the value of 90 [°C/min] in mind, the ramp rate for

Figure 4.3. The woven structure of the conveyor belt.

the test-rig is estimated to be one tenth of this value. Combining this with equation (4.3), it follows that $m_p \approx 3 \, m_b$. The belt mass is about 2 [kg/zone], which would result in an equi-valent plate mass of 6 [kg/zone]. A steel plate of approximately 8 [mm] thick would be sufficient, but available steel plates of 9 [mm] thick were used. With a measurement it will be tested whether approximately equal temperature differences occur in the test-rig as in the real furnace.

A remaining difference between the product plates and a real conveyor belt is the heat conduction inside the plate or the belt. As the plates are made of solid material, and the belt has a woven structure, the heat conduction coefficient is probably larger for the plates than for the belt. This will result in lower temperature differences over the width of the plate than would occur when using a real conveyor belt. However, the plates satisfy for testing the numerical model, because one can also model a solid plate instead of a con-veyor belt. As an extra benefit the conduction coefficient of a solid plate is better deter-mined than for a woven structure like the conveyor belt. Comparisons between the nume-rical model and the set-up will therefore be made using solid product plates. Calculations for lower conduction coefficients, as valid for a real conveyor belt, can always be done afterwards.

Steady experiments

In a steady experiment, the belt plates have to be cooled in order to prevent them from heating up due to the higher muffle temperature. Therefore, for steady experiments the belt plates are replaced by so called 'düsenfelds'. A düsenfeld is constructed as shown in Figure 4.4. It consists of a closed box, containing a plate with an array of small holes. By blowing compressed air through a pipe that is connected to the bottom compartment of the düsenfeld, the bottom compartment is set to high pressure. Because of the high pressure air is blown through the plate with the holes, and a jet array is created that cools the top plate of

Figure 4.4. Construction of a düsenfeld.

the düsenfeld. This top plate is the substitute for the belt surface in the set-up. The compressed air is drained away through two additional pipes that are connected to the top region of the düsenfeld.
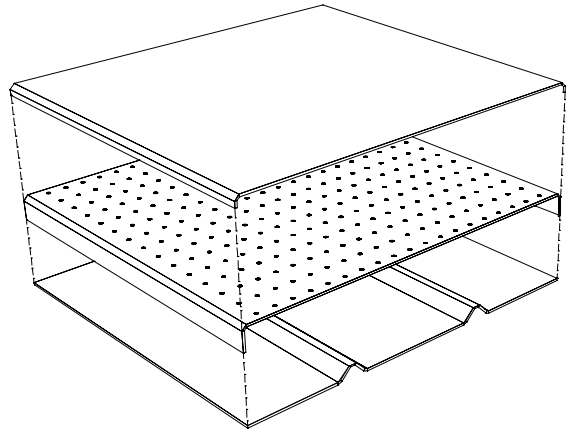
Axial temperature gradients

As the furnace model used is a 2-*D* model, the heat transfer effects in the muffle are theoretically split into 2-*D* effects, occuring in a cross-section of the muffle, and in 3-*D* axial heat transfer effects. The 2-*D* effects depend on cross-sectional temperature gradients, which are local temperature differences between the muffle and the belt. These temperature differences mainly depend on the belt speed in a real furnace. So realistic 2-*D* heat transfer effects can be simulated in the test-rig by using an equivalent heating ramp rate in the experimental set-up as described in the previous section. The 3-*D* heat transfer effects represent the heat transfer between the belt and neighbouring zones, and are determined by axial muffle temperature gradients. Therefore, 3-*D* effects are expected to be independent of the belt speed or the ramp rate. Equivalent 3-*D* heat transfer effects as in a real furnace can be simulated in the test-rig by prescribing the same axial temperature gradient between neighbouring zones. As the test-rig contains the same type of elements and the same zone dimensions as a real furnace no problems are expected in realizing this axial gradient.

Measurement methods

Temperature measurements

In the test-rig both air temperatures and surface temperatures have to be measured. When validating the numerical model, measured surface temperatures of the muffle are used in the model to prescribe the boundary conditions. The calculated air and surface temperatures of the product plates are then compared to the values measured in the experiment. Because of the high temperatures that can occur in the test-rig, all temperatures are measured using thermocouples. The surface temperatures are measured using 35 type *K* thermocouples, which are welded to the muffle and plate surfaces at positions as depicted in Figure 4.5. In the middle zone (zone 2) the largest number of thermocouples is situated, as for this zone the measurements will be compared to the numerical model. To measure a temperature profile, each muffle wall of zone 2 contains three thermocouples. As the temperature differences over the width of the product plate are of main interest, five thermo-

couples are distributed over the width of the plate in zone 2. The thermocouples in the other zones and on the head sides are used to measure the axial temperature gradient. Therefore, one thermocouple per muffle wall is enough for zone 1 and zone 3. The temperature of each head side is measured using three thermocouples. The exact positions of all these termocouples are given in appendix 8.

In zone 2 also the air temperatures are measured. This is done using 11 type *S* thermocouples, which are carried by a frame to hold them at certain positions in the middle cross-section of the muffle (exact positions are given in appendix 8). The reason for choosing type *S* instead of type *K* thermocouples is the lower emission coefficient. During a measurement, radiation from the hot muffle walls will give the thermocouples a higher temperature than the temperature of the air surrounding them. In order to decrease this disturbing effect, the emission coefficient of the thermocouple material must be as low as possible. Furthermore, using small thermocouples will also decrease this effect. Therefore the type *S* thermocouples are produced from 0.1 [mm] thick thermocouple wires, which are carried by thicker wires that are connected to a frame. The construction of such a thermocouple is given in Figure 4.6. More detailed information about the dimensioning of these thermocouples is given in Limpens (1997).

Flow visualization

Figure 4.5. Positions of the type K thermocouples for measuring surface temperatures.
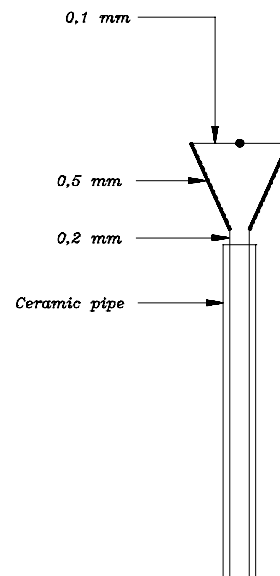
Figure 4.6. Construction of a type S thermocouple used for air temperature measurements.

In order to investigate the flow phenomena inside the muffle a flow visualization system was designed. With this system the flow phenomena in the middle cross-section of the muffle can be visualized by using smoke and a light sheet. The global construction of the visualization system is given in Figure 4.7. The muffle was made optically accessible in the middle of zone 2 by making a gap in the insulation package and the heating elements at both sides of the furnace, and by installing quartz windows in the side-walls of the muffle. Using two light sources, a light sheet is created in the middle cross-section of the muffle. Smoke is injected through two injection pipes. To study the flow behaviour of the smoke in the middle of the furnace, a system of lenses is installed in one head side of the muffle. Smoke was chosen to visualize the flow, because it follows the air flow at the expected flow velocities (a few centimeters per second) very well, and also because it is very easy to inject into the furnace. After injecting smoke into the muffle, one has to wait a certain amount of time until the injection disturbances have damped out. Therefore, the smoke must stay visible long enough. Tobacco smoke appeared to be the best suitable for use in visualization experiments because it is very well temperature resistant, and because it
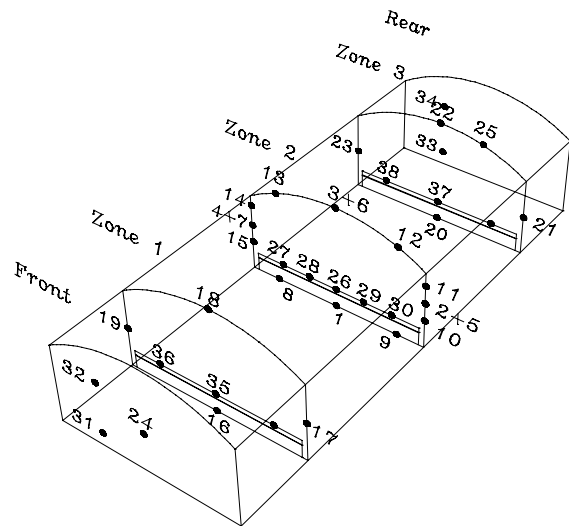
remains visible for a long time. By using a camera and a video recorder the flow behaviour can be recorded. More details about the design of the system of lenses and the rest of the test-rig can be found in Verhaar (1999).
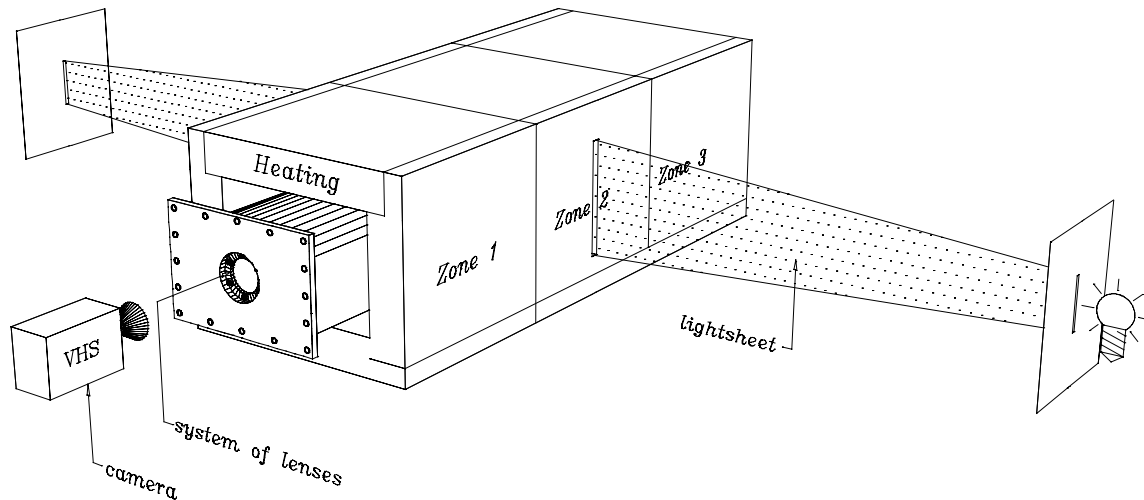
Figure 4.7. Visualization system for investigating flow patterns in the muffle.

4.2 Measurement strategy for determining 3-D effects

In order to determine the 3-*D* heat transfer effects, a comparison is made between a transient 3-*D* measurement and an equivalent 2-*D* measurement. In a 3-*D* measurement the furnace is heated up with a specific ramp rate and with a certain axial temperature gradient over the zones. The equivalent 2-*D* measurement has the same ramp rate, and exactly the same muffle temperature history for the thermocouples in zone 2 as the 3-*D* measurement. The only difference is that in the 2-*D* measurement no axial temperature gradients occur. Because the muffle temperature history in zone 2 for both measurements is the same, differences in the plate temperature histories in zone 2 can only be caused by 3-*D* effects. By comparing the plate temperature histories of both measurements, the influence of 3-*D* heat transfer effects is determined.

As mentioned above, the muffle temperature histories of zone 2 in a set of measurements (a 3-*D* measurement and an equivalent 2-*D* measurement) must be equal. The two measurements are always done at different moments in time. Besides, for a 3-*D* measurement a different start-up strategy is being used as for a 2-*D* measurement. Usually the two measurements are performed on separate days, at about the same clock time. The time shift between the measurements is defined as the clock-time difference on separate days. Two typical tempera-
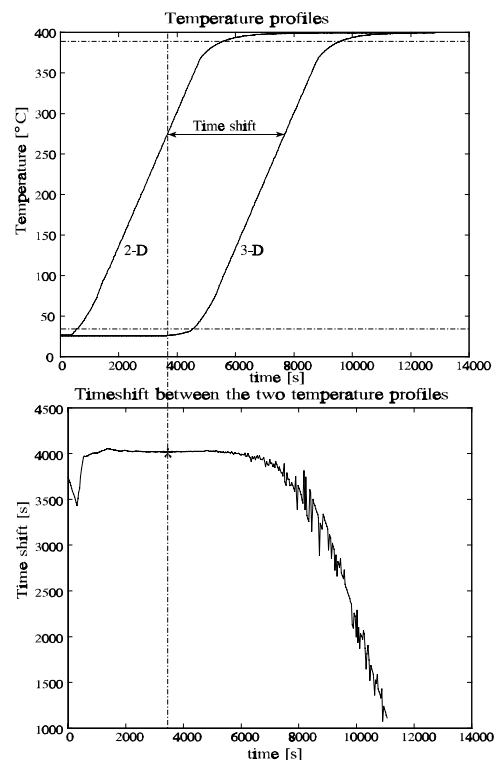

Figure 4.8. Time shift between two temperature profiles at one position of the muffle, obtained in a 2-D and a 3-D experiment.

ture profiles for a 2-*D* and a 3-*D* measurement at one position in the muffle are given at the top in Figure 4.8. As can be seen, the temperature histories are shifted about 4000 [s] in time. Also, the time shift is equal to 4000 [s], while the time delay between the measurements is several days plus 4000 [s]. In order to determine whether two temperature histories fit, the time shift between the time histories is calculated as function of time. This time shift is then plotted in a so called shift graph, as seen at the bottom in Figure 4.8. When the two temperature histories fit, the time shift is constant over time. However, when one of the temperature profiles contains a horizontal part, the time shift in this part is undetermined. As the furnace temperature profiles always start and end with a horizontal slope, the time shift can only be accurately determined in between the dashed horizontal lines in Figure 4.8. As can be seen in the shift graph, in this example two temperature profiles were used, which are shifted approximately 4000 [s].
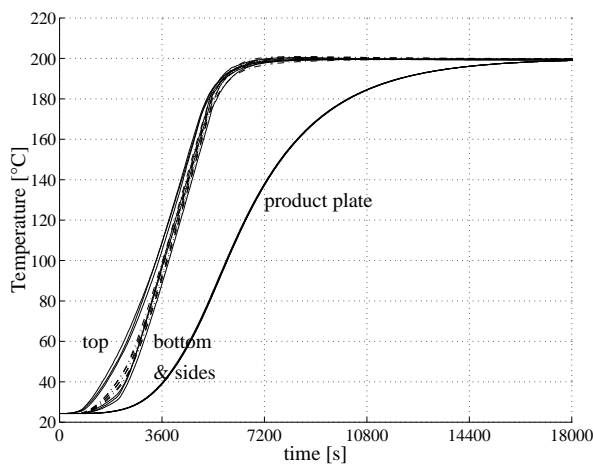

Figure 4.9. Temperature history for zone 2 in the 3-D experiment.
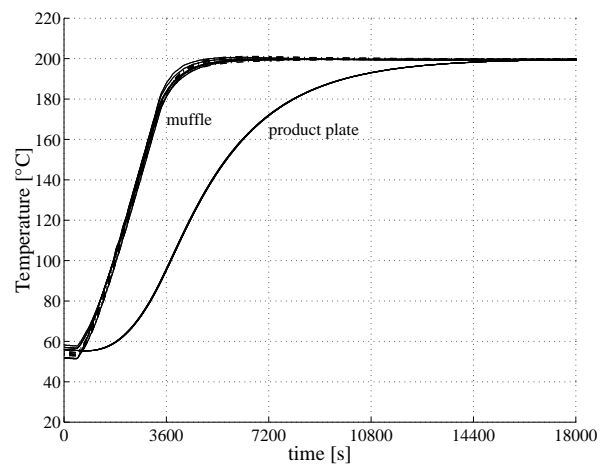
Figure 4.10. Temperature history for zone 2 in the 2-D experiment.

For each measurement set the time shifts for all muffle temperature histories in the 2-*D* and in the 3-*D* measurement must be checked to be constant and equal. Only when all temperature histories of the thermocouples in zone 2 have an equal and constant time shift, the measurements can be used to determine 3-*D* effects. In order to check whether it is possible to make an equivalent 2-*D* measurement for a certain 3-*D* measurement, a test with the experimental set-up was done with a set point of 200 [℃] and a ramp rate of 3 [℃/min]. The axial temperature gradient in the 3-*D* measurement was created by switching on the neighbouring zones of the furnace

Figure 4.11. Time shift graphs for zone 2.

subsequently, with time intervals of 20 minutes. In this way, an axial temperature gradient of about 60 [℃/zone] is expected. The temperature histories for both measurements are given in Figure 4.9 and Figure 4.10. As can be seen in the figures, the muffle was heated up in about an hour and a half, and differences between the muffle temperatures during one measurement remained low, which indicates a uniform muffle temperature at every moment. Also the heat capacity of the product plates appeared to be large enough to

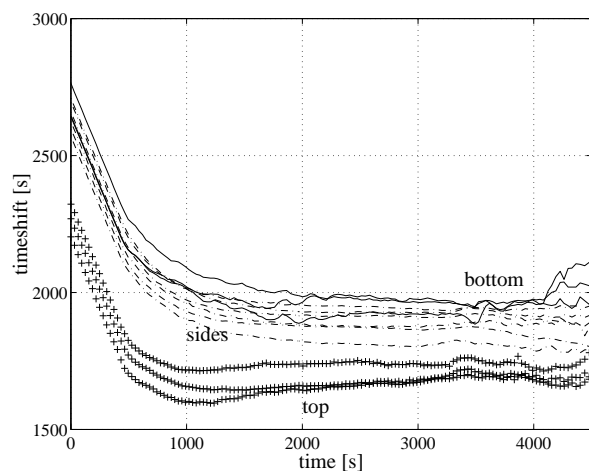create a significant temperature difference between the plates and the muffle. The plates were heated up in about 4 hours.

The time shift graphs for the thermocouples in zone 2 are depicted in Figure 4.11. As can be seen, between 1000 [s] and 4000 [s] the graphs are approximately horizontal, so the separate temperature histories for the thermocouples in zone 2 are comparable during this period. However, the time shift for the top temperature histories appears to differ from the shifts for the sides and the bottom. This is caused by a higher top temperature in the warming-up traject of the 3-*D* measurement, as can be seen also in Figure 4.9. Therefore the measurements are not completely equivalent, and cannot be used for determination of 3-*D* effects. For creating an equivalent set of measurements a higher top temperature in the 2-*D* experiment is necessary.
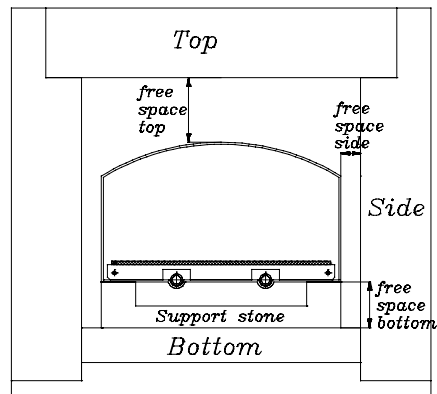
Figure 4.12. Free space between the muffle and the heating elements.

The higher top temperature occuring in the 3-*D* measurement can be explained from a difference in 3-*D* radiative heat transfer from the heating elements to the outer muffle surface. This 3-*D* radiative heat transfer is stronger for the top because the free space between the top elements and the top of the muffle is larger than the free space between the sides and the muffle, as shown in Figure 4.12. At the bottom the support stones will also block 3-*D* radiative transfer, giving less 3-*D* effects than at the top.
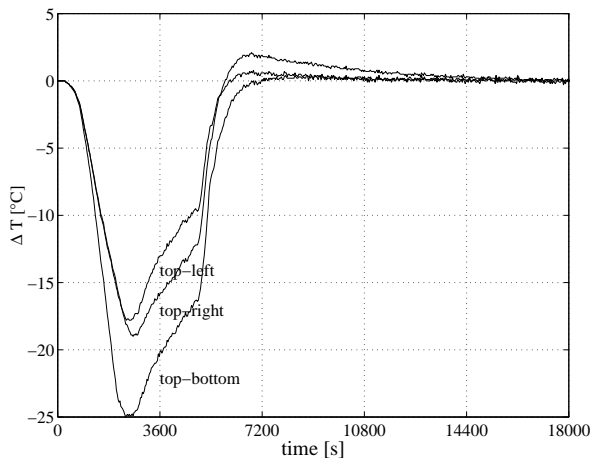
Figure 4.13. Temperature differences between the top thermocouples and the other muffle thermocouples in zone 2.
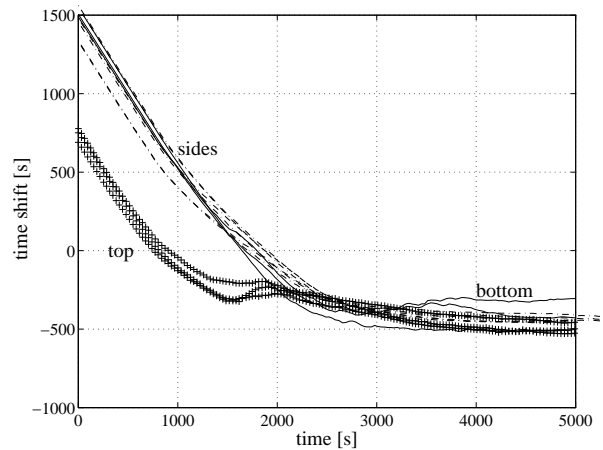
Figure 4.14. Time shift graphs for zone 2 with a preheat for the 2-D measurement of 20 [℃].

As mentioned above, it is necessary to have an increased top temperature of the muffle in the 2-*D* measurement in order to create a set of two comparable measurements. This is realised by preheating the top of the muffle at the start of the 2-*D* measurement. The amount op preheat is determined from the 3-*D* measurement, which therefore always has to be done first. For the 3-*D* measurement shown above the temperature difference

between the top control thermocouple and the other control thermocouples in zone 2 are graphed in Figure 4.13. As can be seen in the figure, the differences are maximum at the start of the measurement, measuring 25 [℃] for the top-bottom difference and about 18 [℃] for the top-side differences. From this result, the top preheat for the equivalent 2-*D* measurement must be chosen between 18 [℃] and 25 [℃]. A value of 20 [℃] was chosen for the preheat, and a new 2-*D* measurement was done. The time shifts between this measurement and the 3-*D* measurement are presented in Figure 4.14. The time shifts for zone 2 are now all within a much narrower band. Only for one bottom thermocouple a time shift value is found which is a bit higher than the other shift values. However, the other bottom thermocouple shifts appear to be relatively low compared to all the other shifts (they are in the low region of the band). Therefore, it can be concluded that there is no valid indication that the bottom temperature histories for the two measurements are significantly different. The measurement set seems to be good enough for being used to investigate 3-*D* heat transfer effects.

4.3 Determination of the control parameters

In this section the heating up of the furnace is studied. This is done to predict a certain temperature history for given values of the control parameters. Also suitable values of the control parameters are determined, so that the furnace temperature reaches the set point in a smooth way.

The electrical power a PD controller puts to the heating elements is calculated as

$$Q_{el} = K_p \left(T_{set} - T_m \right) + K_p \tau_d \frac{\partial}{\partial t} \left(T_{set} - T_m \right), \quad (4.5)$$

with Q_{el} the electrical power, T_{set} the set point temperature, T_m the actual (measured) temperature, K_p the proportional action, and τ_d the differentiation time of the controller. This power is constrained by zero and a certain maximum value.

$$0 \leq Q_{el} \leq Q_{max}. \quad (4.6)$$

The proportional action is defined as

$$K_p = \frac{Q_{max}}{T_p}, \quad (4.7)$$

with T_p the proportional band. This is in fact the offset from the set point temperature over which the output power is proportionally varied from maximum to zero, as given in Figure 4.15. The proportional band and the differentiation time are control parameters to be set by the user. In order to determine suitable values for the control parameters, a simplified model of the furnace has been made.
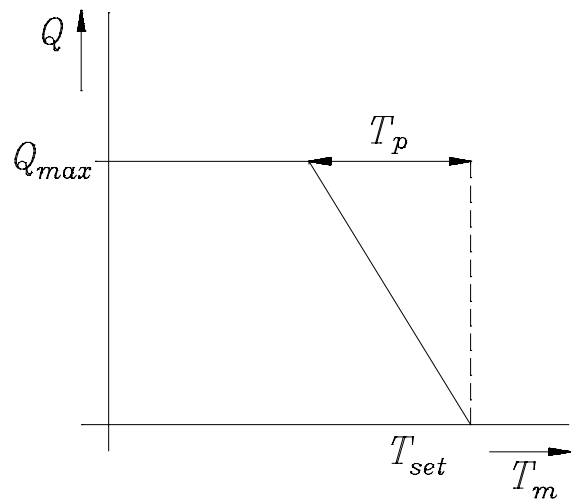

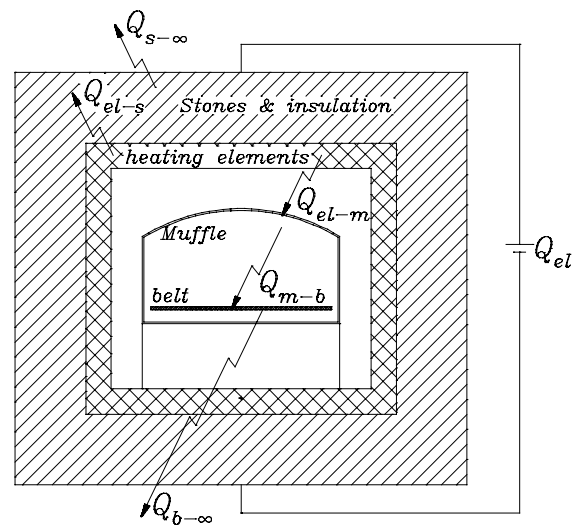*Figure 4.15. Power output for the proportional controller action.*

Figure 4.16. Simplified model for the heat transfer in the furnace.

In the simplified model, the insulation package, the heating elements, the muffle and the belt are all treated as isothermal bodies with a certain mass and heat capacity. The heat fluxes between these bodies are given in Figure 4.16, where $Q_{b-\infty}$ equals the heat flux from the belt to the environment of the furnace by cooling, and $Q_{s-\infty}$ is the heat loss from the insulation package to the environment. The transient energy equations for the accompanying bodies are now given by

$$\left(m c_p\right)_{el} \frac{\partial T_{el}}{\partial t} = Q_{el} - Q_{el-m} - Q_{el-s} , \qquad (4.8)$$

$$\left(m c_p\right)_m \frac{\partial T_m}{\partial t} = Q_{el-m} - Q_{m-b} , \qquad (4.9)$$

$$\left(m c_p\right)_s \frac{\partial T_s}{\partial t} = Q_{el-s} - Q_{s-\infty} , \qquad (4.10)$$

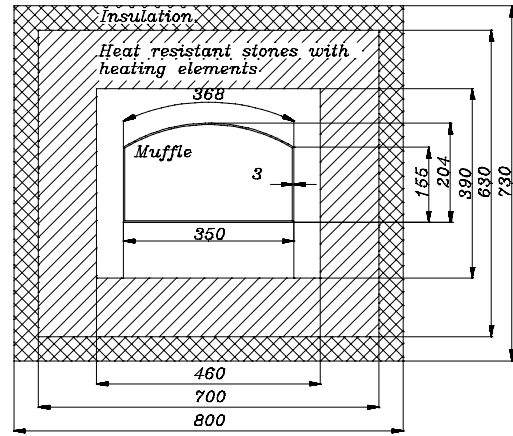$$\left(m c_p\right)_b \frac{\partial T_b}{\partial t} = Q_{m-b} - Q_{b-\infty} . \qquad (4.11)$$

In these equations *el* denotes the electrical heating elements, *m* denotes the muffle, *s* denotes the stones and insulation package, *b* denotes the belt and ∞ denotes the environment. The heat loss from the heating elements to the insulation package is caused by conduction. Taking the temperature at half of the thickness of the insulation package as the characteristic insulation package temperature, this heat flux equals

Figure 4.17. Global dimensions of the insulation package.

$$Q_{el-s} = \frac{k_s A_s}{\frac{1}{2}h}\left(T_{el} - T_s\right). \qquad (4.12)$$

In this equation, T_{out} is the outer surface temperature of the furnace, and k_s, A_s and h are the conduction coefficient, the inner surface area and the thickness of the insulation package respectively. A_s and h can be determined using the global dimensions given in Figure 4.17, while k_s is known from material properties to equal approximately 0.26 [W/m K].

The heat loss from the insulation package to the environment is caused by natural convection. It can be calculated as

$$Q_{s-\infty} = h_c A_{out}\left(T_{out} - T_\infty\right), \qquad (4.13)$$

with h_c the heat transfer coefficient and A_{out} the outer surface area of the furnace. A linear temperature in the insulation package is assumed, causing the temperature difference between T_s and the outer surface temperature T_{out} of the furnace to be equal to the difference between T_s and T_{el}. Hence, for the outer surface temperature holds

$$T_{out} = 2 T_s - T_{el}. \qquad (4.14)$$

The heat fluxes between the heating elements, the muffle and the belt are assumed to be purely radiative. If the elements, the muffle and the belt are treated as black bodies, then the heat fluxes can be calculated as

$$Q_{el-m} = \sigma A_m\left(T_{el}^4 - T_m^4\right). \qquad (4.15)$$

$$Q_{m-b} = \sigma A_b\left(T_m^4 - T_b^4\right). \qquad (4.16)$$

The equations (4.8) to (4.16) form a coupled system of differential equations, describing the temperature history of the heating elements, the muffle and the belt as function of their physical properties and the control parameters.

In order to determine suitable values for the control parameters an estimation of all physical properties has been made. The necessary surface area's are found to equal

$$A_m = 1.0 \left[m^2 \right] \quad , \quad A_b = 0.3 \left[m^2 \right] \quad , \quad A_s = 1.53 \left[m^2 \right] \quad , \quad A_{out} = 2 \left[m^2 \right]. \tag{4.17}$$

The value of h_c for the natural convection from the furnace outer surface to the environment is assumed to equal 10 [W/m^2 K]. Furthermore, for all the components, an estimation of the mass and heat capacity can be made based on their global dimensions. The heating elements consist of winded Kanthal wire, which is embedded in heat resistant stones as depicted in Figure 4.18. The stones serve as a heat equilibrating system, and also form a large part of the insulation package of the furnace. Therefore the stones have a very low thermal conductivity (0.26 [W/m K]), and only a small layer of the stones will heat up to the temperature of the Kanthal wires. In the model, this layer is modelled as the heating elements, while the rest of the stones is modelled as insulation package. As the spacing between the grooves in the stones equals 18 [mm], the heating element layer of the stones is assumed to be 9 [mm] wide, as hatched in Figure 4.18.
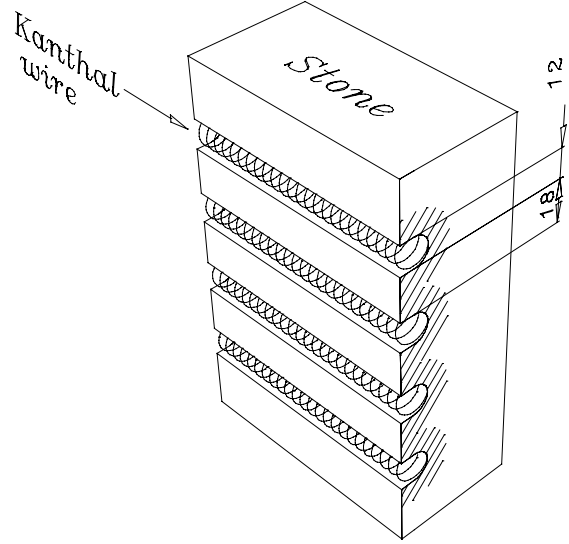
Figure 4.18. Construction of the heating elements.

Some global dimensions of the heating elements are given in Table 4. From these dimensions mc_p of the heating elements for all the zones can be calculated, which equals mc_p for the Kanthal wire plus mc_p for the stones. For the Kanthal wire holds a density ρ_{wire} = 7100 [kg/m^3] and a heat capacity $c_{p,wire}$ = 460 [J/kg K], and thus, mc_p for the total wire length of 217.05 [m] equals

$$\left(m c_p \right)_{wire} \approx 2227 \ [J/K]. \tag{4.18}$$

The stones have a density of ρ_{stone} = 721 [kg/m^3] and a heat capacity $c_{p,stone}$ = 1100 [J/kg K]. The value of mc_p is then equal to

$$\left(m c_p \right)_{stone} \approx 6649 \ [J/K]. \tag{4.19}$$

Adding the values for the wire and the stones, it is found that

$$\left(m c_p \right)_{el} \approx 8876 \ [J/K]. \tag{4.20}$$

The part of the stones that is not incorporated in the heating elements is treated as insulation package. Using the same material properties as above, the mc_p for this insulation package is calculated to equal approximately

Element	l_{groove} D_{core}	l_{wire} d_{wire}
Top	3400 [mm] 12 [mm]	29.70 [m] 2 [mm]
Bottom	3400 [mm] 12 [mm]	29.70 [m] 2 [mm]
Sides	3740 [mm] 12 [mm]	12.95 [m] 2 [mm]

Table 4. Global heating element properties.

$$\left(mc_p\right)_s \approx 200000 \; \left[J/K\right]. \qquad (4.21)$$

The muffle is made of steel, having a density of ρ_m = 7817 [kg/m^3] and a heat capacity equal to c_{pm} = 461 [J/kg K]. The global cross-sectional furnace dimensions are given in Figure 4.17, and from these, the cross sectional area of the muffle is calculated to equal A_{cm} = 3.07·10^{-3} [m^2]. Then over the heated length of l = 0.9 [m], $(mc_p)_m$ can be calculated as

$$\left(mc_p\right)_m = \left(\rho c_p\right)_m A_{cm}\, l \approx 9.9 \cdot 10^3 \; \left[J/K\right]. \quad (4.22)$$

In the experiments to be done, the belt is replaced by düsenfelds, which are also made of steel, just like the muffle. With the global dimensions given in Figure 4.19, $(mc_p)_b$ for the total amount of three düsenfelds is calculated to equal approximately

Figure 4.19. Global dimensions of a düsenfeld.

$$\left(mc_p\right)_b \approx 7.0 \cdot 10^3 \; \left[J/K\right]. \qquad (4.23)$$

Most experiments are done with the air cooling for the düsenfelds turned off, so $Q_{b-\infty}$ = 0. Now all the physical parameters in the model equations are known. After some numerical tests with the model for various values of the control parameters, it is found that a smooth temperature history from room temperature to 200 [°C] can be realized within an hour when T_p = 20 [K] and τ_d = 500 [s].

A test with the experimental set-up was done using these values for the control parameters for all controllers. The furnace appeared to heat up smoothly to the set point of 200 [°C]. Only the head sides of the furnace appeared to heat up slower than the zones, and also not to reach the set point, which must be caused by a larger heat loss to the environment and less powerfull heating elements. A smaller value for T_p will divide the maximum amount of output power over a smaller temperature range (Figure 4.15), and will therefore give better results in reaching the set point. Also a smaller value for τ_d will give a faster heating rate. Therefore, for the controllers of the head sides values of T_p = 3 [K] and τ_d =250

Figure 4.20. Measured temperature history for the middle zone.

[s] were chosen. For these settings, the measured temperature history for the middle zone is shown in Figure 4.20. As can be seen, the sides and the bottom have a common temperature history without overshoot or oscillations, which means that the estimated control parameters are suitable for these controllers. The top has a small overshoot, which indicates that a higher value for τ_d is required. Hence, a value of 600 [s] is chosen for the top elements.
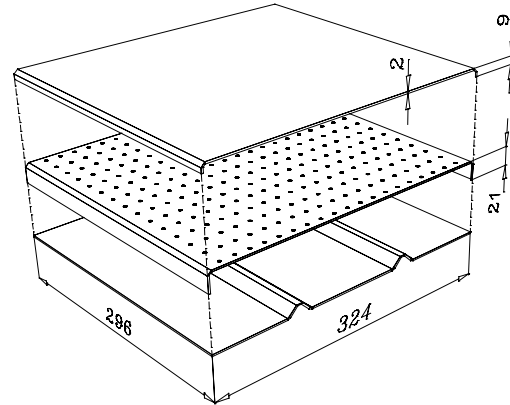
4.4 Test measurements

Test measurements for the type K thermocouples

The type *K* thermocouples used for the measurements of the surface temperatures are all taken from one batch of thermocouple wire. Therefore only the first and the last part of the wires are tested to agree with the standard thermocouple relations from Burns et al. (1993). It is assumed that all the thermocouple faults lie in between the faults of the first and the last part. As test measurements the temperature of melting ice and boiling water are determined.

The theoretical value of the boiling point of water was determined at an environmental pressure of 748,8 [mmHg]. As can be seen in Table 5, an absolute accuracy of about 0.5 [℃] can be achieved using the relations from Burns et al. (1993). The relative accuracy is much better (< 0.1 [℃]), which is more important for determining temperature differences. This is satisfactory according to the demands. Therefore, these relations will be used for the type *K* thermocouples during the measurements.

	First part	Last part	Theoretical value
Ice	-0.23	-0.20	0.00 [℃]
Boiling water	100.11	100.06	99.48 [℃]

Table 5. Calibration measurements for the type K thermocouple wire.

Steady temperature measurements in the furnace

In the furnace two types of thermocouples are used. The type *K* thermocouples are used to measure wall temperatures of the muffle and the düsenfelds. These thermocouples are connected to an electronic ice point thermocouple reference. For measuring the air temperatures type *S* thermocouples are used. These are positioned on a frame inside the furnace to measure the air temperatures at 11 points in the middle cross-section of the muffle. In order to check the consistency of the two types of thermocouples, the following test has been carried out.

The furnace was heated to 200 [℃], and kept steady at this temperature for about 5 hours. After this period of time, the whole muffle with the inclined air is in a steady situation with all temperatures at about 200 [℃]. In Figure 4.21, both the measured wall and air temperatures are shown. As can be seen from the figure, the muffle temperatures are all between 198 and 200 [℃]. The type *S* thermocouples for determining the air temperatures were calibrated to give a maximum of 1 [℃] inaccuracy in the range of 20 to 600 [℃]. Therefore, from Figure 4.21 it can be concluded that at a temperature level of 200 [℃] the temperatures measured by the type *S* thermocouples are about 1 or 2 [℃] lower than the temperatures measured by the type *K* thermocouples.
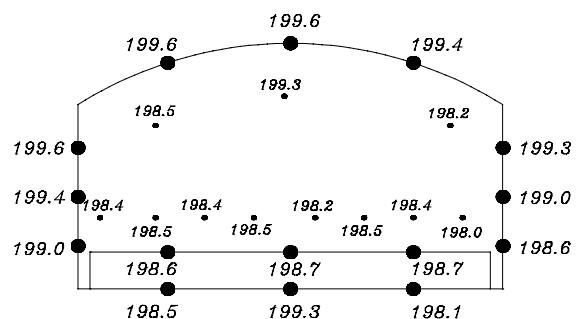

Figure 4.21. Measured surface temperatures of the muffle and the düsenfelds.

One reason for the observed difference could be an inaccuracy of the type *K* thermocouples, which would mean that they give an overestimation of the actual temperature. However, calibration of the type *K* thermocouples pointed out that they were accurate to

about 0.2 [℃] in the range between 0 and 100 [℃] (Table 5). Also, another steady measurement has been done with the furnace at room temperature. The furnace was cut of power for a weekend, and all the furnace walls including the head sides had reached a steady temperature of 19 [℃] (all temperatures were between 18.75 and 19.32 [℃]). In this case also the air temperatures were measured to be around 19 [℃], so no difference in the type *K* and the type *S* thermocouples could be found.

Another reason for the difference could be heat losses through the quartz windows in the middle zone. Heat transfer between the type *S* thermocouples and the colder environment might take place through these windows. Or the windows themselves could be colder than the muffle walls due to the gap in the heating elements and in the insulation package. To test this hypothesis, a steady experiment at 200 [℃] was done with the air thermocouples placed in zone 3. The values for the muffle temperatures in zone 3 and the air temperatures are depicted in Figure 4.22. As can be seen, the air temperatures are not underestimated, so the measured difference between the type *K* and the type *S* thermocouples in the middle zone must be caused by heat losses at the quartz windows.
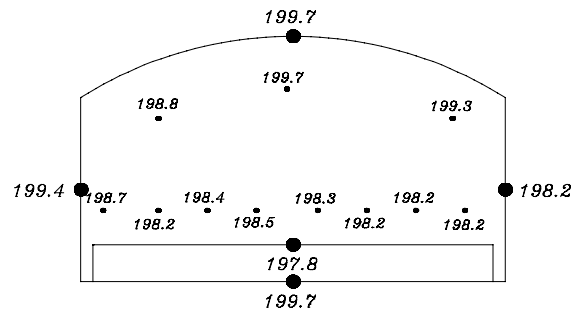

Figure 4.22. Muffle temperatures in zone 3.

By insulating the window orifices it was tried to reduce the heat losses. After insulation was installed, made of the same heat resistant stones used for the heating elements and the major part of the insulation package of the rest of the furnace, again a steady experiment at 200 [℃] was done. This time the temperature differences between the type *K* and the type *S* thermocouples decreased, but did not vanish totally. It is therefore concluded that due to the gap in the heating elements at the position of the light sheet a lower temperature at the quartz windows in the muffle will occur. This effect may disappear when the furnace is operated at higher temperatures, as then also the heat resistant stones will start to radiate, and a more uniform heat transfer will take place. However, the difference is only small (1 or 2 [℃]), so no large measurement errors are expected due to this cause.

Determination of the maximum ramp rate

By heating the test-rig at maximum power, the maximum ramp rate that can be obtained was determined. For the test measurement already performed in Figure 4.20, 100% power is sent to the elements during the largest part at the beginning of the heating process. In Figure 4.23 this first part of the temperature history for the muffle and the düsenfelds in the middle zone is depicted. As can be seen in the figure, the maximum temperature gradient in time that occured during this measurement can be calculated to be approximately 10 [℃/min]. As the furnace was heated at maximum power, this is the maximum temperature gradient that can be gained using the setup. With this amount of power, the düsenfelds
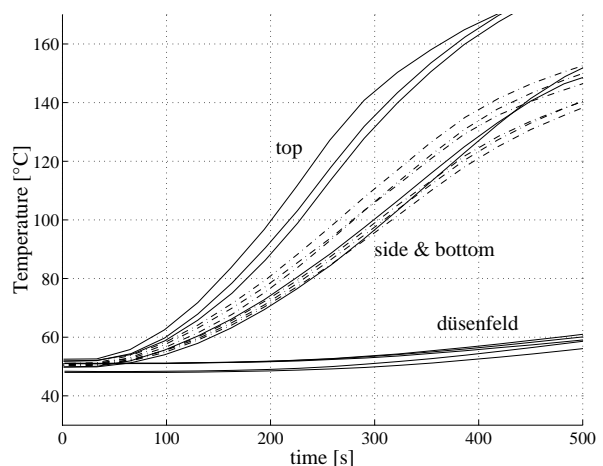

Figure 4.23. Temperature history in zone 2 for a ramp rate of 10 [℃/min].

are fully heated in about 10000 [s] when not cooled. The figure also shows that there are some differences between the various muffle thermocouples in the zone. First of all, the top is heated faster than the sides and the bottom, and furthermore, there are also some differences between the various side and bottom elements. These differences are caused by the differences in heat transfer inside the muffle. Also a temperature difference between the left and the right hand side of the furnace of about 1 to 2 [°C] is found, though the left and right side-elements are controlled by the same controller. This difference may be caused by a difference in resistance between the left and the right side elements.
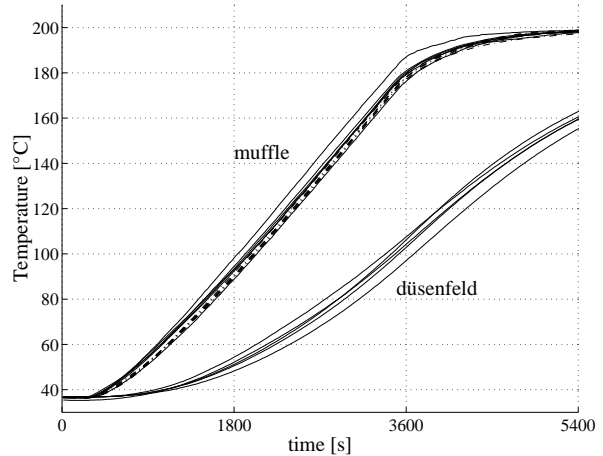
Figure 4.24. Temperature history in zone 2 for a ramp rate of 3 [°C/min].

By prescribing a ramp rate lower than 10 [°C/min], the observed temperature differences may disappear, because then strength differences between the heating elements do not count since they are not operated at maximum power. In order to check this, a measurement was done with a set point of 200 [°C] and a prescribed ramprate of 3 [°C/min] for all the zones. The measured temperature history for zone 2 is given in Figure 4.24.

As can be seen in the figure, the temperature differences between the muffle thermocouples have become much lower. This proves indeed that the differences in measured muffle temperatures were mainly caused by power differences between the heating elements, which manifest the most when they are controlled at maximum power. For creating well defined situations, the undefined differences between the muffle temperatures must be prevented. Therefore, in future measurements a prescribed ramp rate for the muffle temperatures will be used, which must be lower than 10 [°C/min] for preventing the elements from being controlled at maximum power.

CHAPTER 5. FURNACE ANALYSIS

With the experimental set-up, the numerical model can be validated and the source terms representing the 3-*D* heat transfer phenomena can be determined. In this chapter, first the 2-*D* steady flow phenomena in the muffle are investigated, and compared to the results of the Navier Stokes solver. Afterwards the importance of 3-*D* heat transfer effects in the muffle is investigated by comparing 2-*D* and 3-*D* measurements. The 3-*D* radiation effects are also investigated separately, using a simplified 3-*D* numerical model.

5.1 2-*D* Model validation

In order to validate the 2-*D* model used for calculating the natural convection in the muffle, some 2-*D* steady measurements were performed. These measurements will show whether the flow phenomena in the muffle remain steady and symmetric, as assumed in the model. Besides, it will be investigated whether the expected vortex structures actually occur in the muffle.

In a 2-*D* measurement, the three zones of the set-up have an equal temperature setting, so no axial temperature gradients occur. The head ends are covered by an aluminium foil, which has very good reflective properties. In this way 3-*D* radiation effects are minimized. Furthermore, in the experiment the düsenfelds are installed on the bottom of the muffle. The muffle temperature is kept constant at a certain temperature value. The top temperatures of the düsenfelds are also kept constant, but at a lower temperature by using air cooling. In this way, a well defined 2-*D* situation is created, which can be compared to a steady calculation. Because of the use of the düsenfelds, the maximum temperature for 2-*D* steady measurements is about 200 [°C].

Results obtained from the 2-*D* steady measurements are muffle and air temperatures, and a visualised flow pattern by using smoke injection. With the measured muffle temperatures used as boundary conditions in a calculation, the air temperatures and the flow pattern can be calculated and compared to the measurements.

2-D convection at 200 [°C]

In this experiment, the muffle wall temperatures were set to 200 [°C]. By using air cooling the temperatures in the middle of the düsenfelds were set to 168.8 [°C]. In Figure 5.1 the measured temperatures for the muffle walls are depicted. As can be seen in the figure, the axial temperature gradients in the muffle are very low, as they should be for approximating a 2-*D* situation. In Figure 5.2a the central cross-section of the muffle is depicted. At the sides of the düsenfelds, the temperatures appear to be higher because of the heat transfer from the muffle. Furthermore, there is a decreasing temperature profile in the height direction for the side-wall. The fact that the side-wall is hotter near the bottom is caused by extra heat added from the bottom elements which react on the cooling of the düsenfelds. In Figure 5.2c the flow field visualised by smoke injection in the furnace is shown. It consists of a counterclockwise rotating vortex, which is mainly situated in the upper part of the muffle.
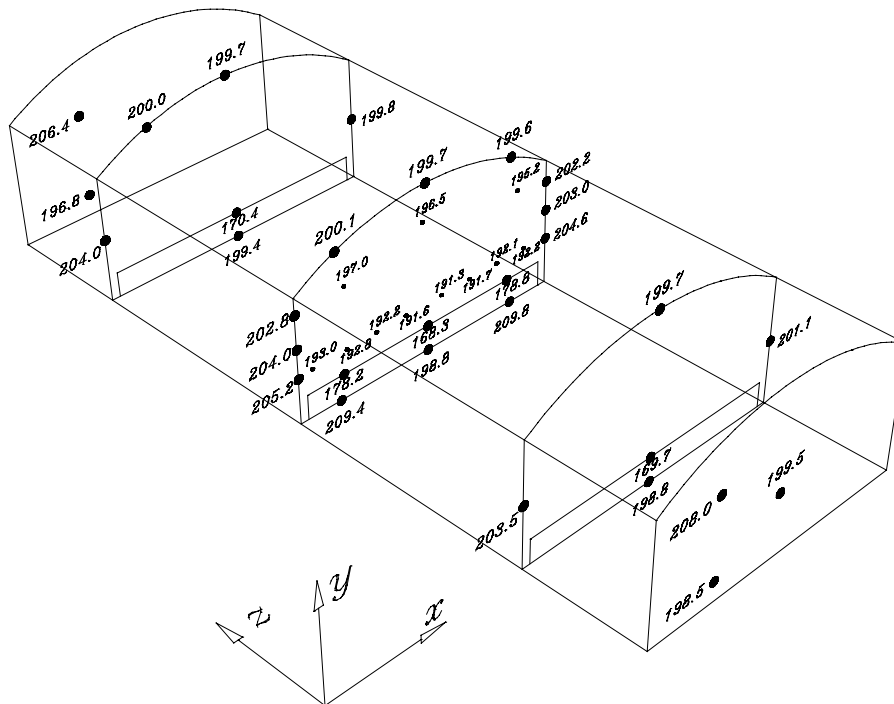
Figure 5.1. Measured muffle surface temperatures.

For the situation mentioned, a numerical calculation has been carried out. The measured muffle temperatures are taken as boundary conditions for the calculation. In Figure 5.2d streamlines for the calculated flow are given. The flow also consists of a counterclockwise rotating vortex which appears in the upper part of the muffle, just like the one obtained experimentally by visualisation. The calculated and the visualised flow patterns have a similar shape, and the centres of the vortices seem to appear at approximately the same positions. The maximum velocity is calculated to be about 4.5 [cm/s] and occurs near the side-wall of the muffle.

In Figure 5.2b, the calculated temperature profiles at the height positions where the air thermocouples are situated in the experiment are shown. For the lowest air thermocouples, the temperature varies between 193 and 194 [℃]. The temperature in the upper part of the muffle equals 200 to 202 [℃]. Comparing the calculated temperatures to the measured ones, it can be concluded that the calculated temperatures are about 2 [℃] (in the bottom region) to 4 [℃] (in the top region) higher than the measured temperatures. As mentioned in the previous section with the steady experiments for the whole furnace at 200 [℃], a part of this error may be systematically caused by heat losses at the quartz windows. However, the measured mutual temperature differences between the various air thermo-couples are similar to the calculated ones.

Several other 2-*D* steady measurements were carried out at a temperature of about 200 [℃], but with different temperature gradients along the muffle walls. These measurements showed that the flow phenomena in the muffle are strongly temperature-dependent. In Figure 5.3 and Figure 5.4 two muffle temperature settings for 2-*D* steady measurements are given. In Figure 5.5 and Figure 5.6 the visualised flow paterns are shown, while in Figure 5.7 and Figure 5.8 the calculated contour lines of the flow field are depicted. As can be seen in the figures, the flow indeed is highly temperature-dependent. For the left case, the top of the muffle is slightly colder than the sides. The visualization shows that the two counterclockwise rotating vortices appear in the upper region of the muffle. In the right case, the top temperature of the muffle is higher than the sides. Then the vortices appear
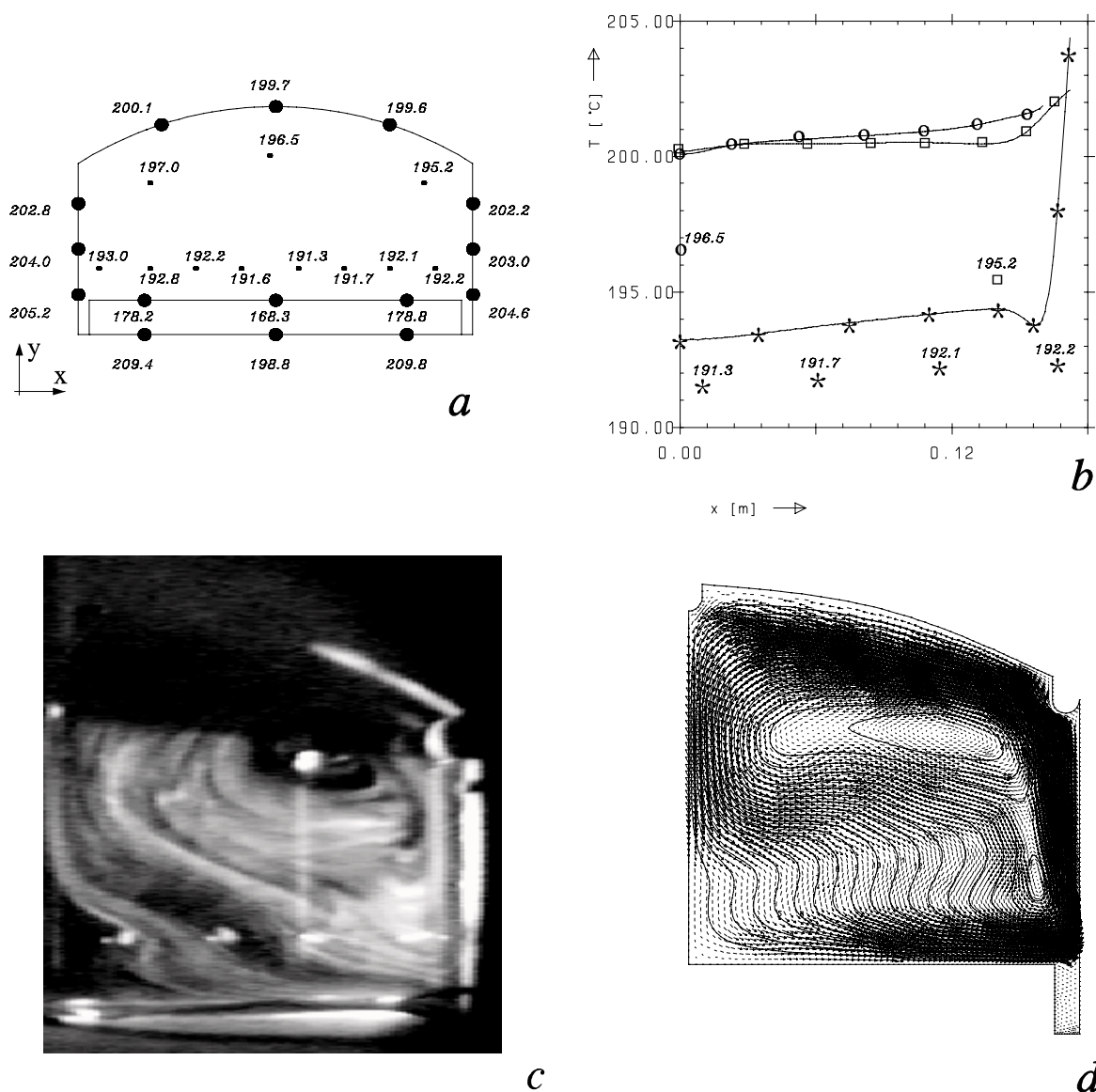
Figure 5.2. (a) Measured muffle and air temperatures, (b) comparison of measured (marker & value) and calculated (marker & solid line) air temperatures, (c) visualised flow pattern and (d) calculated flow pattern.

in the lower corners, and also have a different shape. This characteristic behaviour is also calculated numerically, showing a good agreement between the visualization experiment and the numerical model. As the calculated and measured temperature differences follow the same trends, it is concluded that the model is suitable for calculating flow patterns and temperature fields within an error range of a few degrees. This is good enough for making a design tool for furnace optimization.
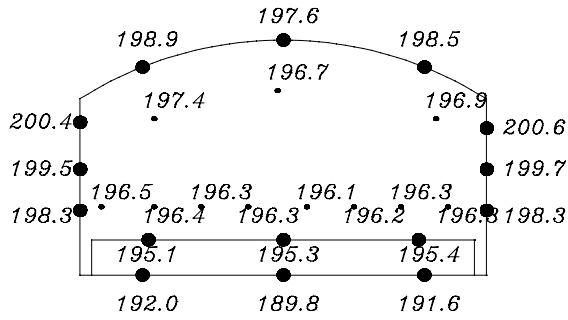
Figure 5.3. Muffle and air temperatures for steady 2-D measurement at 200 [℃].
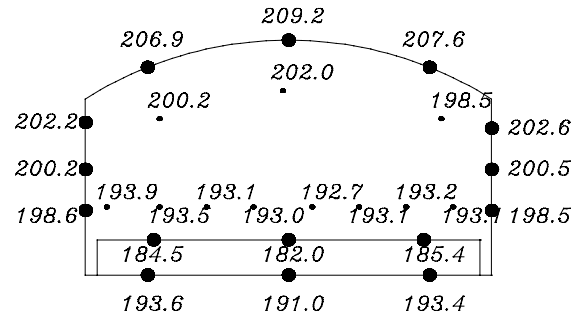
Figure 5.4. Muffle and air temperatures for steady 2-D measurement at 200 [℃].
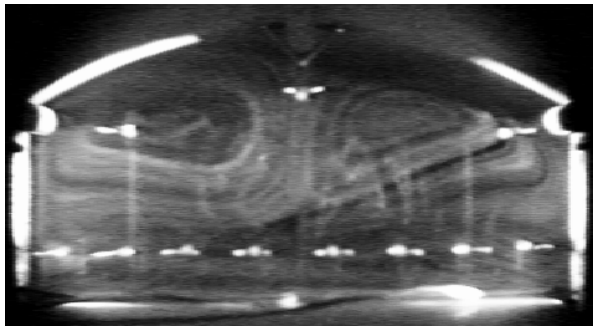
Figure 5.5. Visualized flow pattern for the temperature setting shown in Figure 5.3.

Figure 5.6. Visualized flow pattern for the temperature setting shown in Figure 5.4.

Figure 5.7. Calculated flow pattern for the temperature setting shown in Figure 5.3.

Figure 5.8. Calculated flow pattern for the temperature setting shown in Figure 5.4.

5.2 The influence of 3-D effects

The 3-*D* heat transfer effects in the muffle are expected to be dependent on the axial temperature gradient in the muffle, and also on the temperature gradient in time (the so called 'ramp rate'). Therefore several measurement sets were carried out, with for each set characteristic values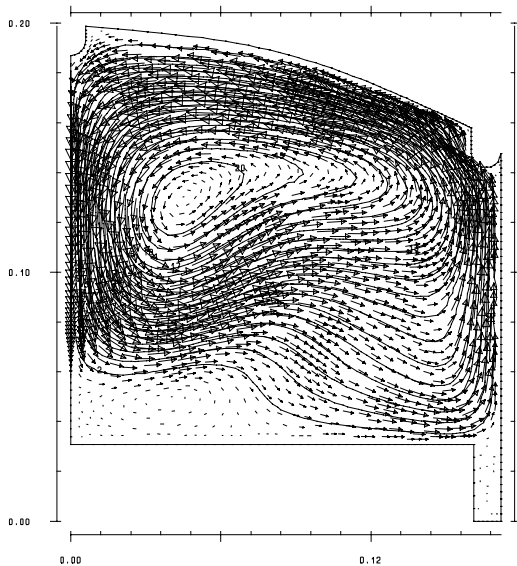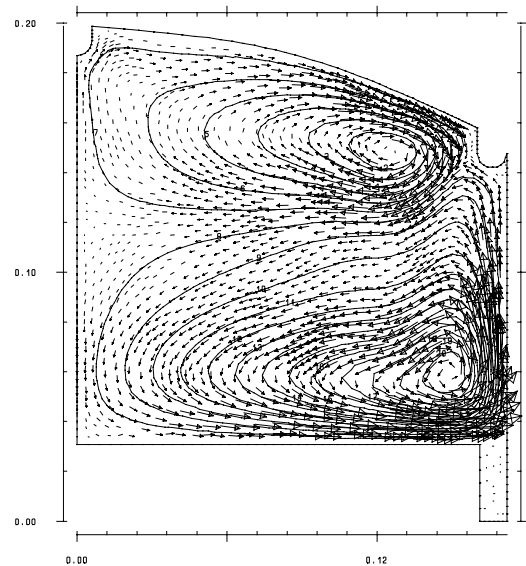 for the axial temperature gradient and for the ramp rate. As already mentioned in section 4.2, each measurement set consists of a 3-*D* and an equivalent 2-*D* transient measurement. The importance of 3-*D* effects can be deduced by comparing the plate temperatures in zone 2 for the 2-*D* and the 3-*D* measurement.

Experiments

Measurement sets

In order to measure the 3-*D* effects, measurements with different values for the ramp rate and the axial temperature gradient were done. Because the highest temperature differences are expected to occur at high temperatures, the variations of the ramp rate and of the axial temperature gradient were done at 600 [℃]. As the 3-*D* effects may also depend on the absolute temperatures in the muffle, measurements at different temperature levels were carried out. With product plates installed inside the muffle instead of the düsenfelds, the test-rig can go up to temperatures of 600 [℃]. In the following table the characteristic properties of the measurement sets are summarized.

Measurement set number	1	2	3	4	5
Set point [℃]	200	400	600	600	600
Ramp rate [℃/min]	3	5	5	8	8
Axial gradient [min/zone]	20	15	15	15	25
2-*D* preheat [℃]	20	25	25	30	50

Table 6. Parameters in the measurement sets.

In the table the set point and the ramp rate for each measurement set are given. The values for the ramp rate are chosen in such a way that the highest value is still below 10 [℃/min], see section 4.4. In a real conveyor belt furnace the ramp rate for the belt with products is much higher, but the measurement situation is equivalent to the real furnace situation because of the use of specially designed product plates instead of the conveyor belt, as mentioned in section 4.4. The axial gradient for the 3-*D* measurement is given in [min/zone], which is actually the time shift between ignition of the subsequent zones. The used preheat of the top of the muffle for the 2-*D* measurement, as motivated in section 4.2, is given in the next line of the table.

The temperature distribution was measured using the product plate in zone 2 of the test-rig. This product plate contains 5 thermocouples over its width, one in the middle, two at the inner sides and two at the outer sides. The side thermocouples are placed symmetrical with respect to the middle (thermocouples 26-30 and 35-38 in appendix 8). In each measurement, the temperature differences between the thermocouples at the sides and the thermocouple in the middle of the product plate were determined. A comparison between the 2-*D* and the 3-*D* measurement in one set shows the influence of 3-*D* heat transfer effects. By making comparisons between the several sets, the influence of various parameters can be investigated. The influence of the temperature level is investigated by comparing the measurement sets 1, 2 and 3. It has to be noticed that measurement set 1 besides a

lower temperature level also has a lower ramp rate. From a comparison between set 3 and set 4 the influence of the ramp rate is determined, and the influence of the axial gradient is determined by comparing set 4 to set 5. In the following sections the several influences mentioned will be investigated. A detailed description of the separate measurements can be found in appendix 9.

Influence of the absolute temperature level

The influence of the temperature level on the temperature uniformity is investigated by comparing the measurements from set 1, 2 and 3.
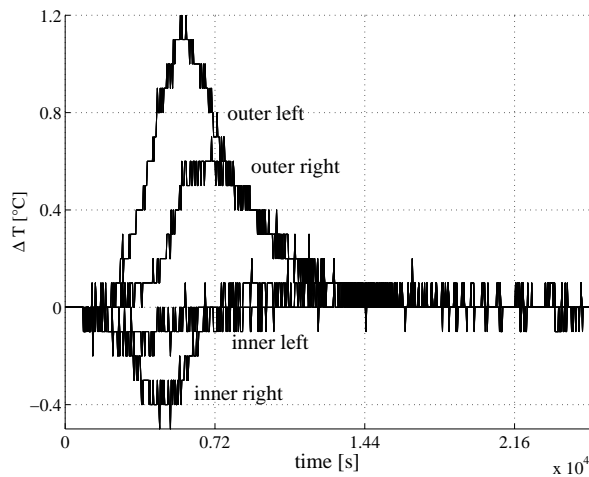

Figure 5.9. Temperature differences compared to the middle for the 3-D experiment in set 1.
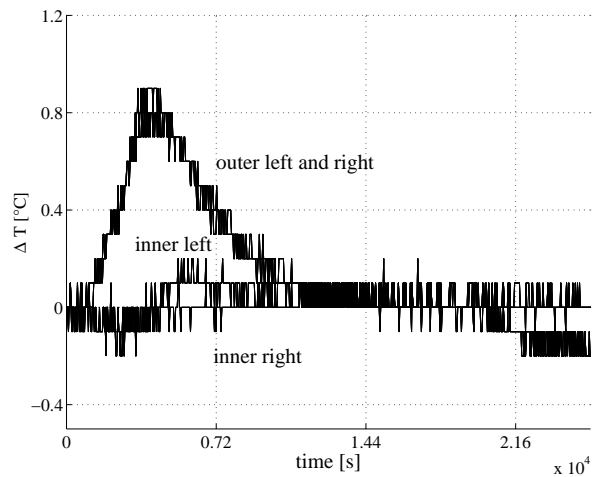
Figure 5.10. Temperature differences compared to the middle for the 2-D experiment in set 1.

In Figure 5.9 and Figure 5.10 the temperature differences for the 2-*D* and the 3-*D* measurement in set 1 are depicted. Each graph represents a temperature difference between a thermocouple at the side of the plate and the thermocouple in the middle, and is labeled using the name of the side thermocouple. So the graph labeled 'outer right' represents the temperature difference between the thermocouple at the outer right hand side of the plate and the thermocouple in the middle. As there are four thermocouples at the sides (two on the left and two on the right), there are also four temperature difference graphs. As can be seen in the figure, the differences are never higher than about 1 [℃]. Because this is about the thermocouple accuracy, no conclusions can be drawn from these graphs with respect to 3-*D* heat transfer effects. The only conclusion to be drawn is that in this low temperature range no significant differences occur.

Also for set 2 at a temperature level of 400 [℃] the temperature differences between the thermocouples at the sides and the thermocouple in the middle of the product plate in zone 2 were determined. These temperature differences are graphed in Figure 5.11 and Figure 5.12. As can be seen in the figures, the differences near the sides of the product plates are about 5 [℃], while the differences nearer to the middle of the belt are lower than 1 [℃]. A slight difference can be seen between the left and the right hand side of the furnace. The temperature differences are larger than in the previous measurement set, which shows that either an increase of temperature level or an increase of the ramp rate causes an increase in temperature differences. However, no significant difference in temperature uniformity is measurable between the 2-*D* and the 3-*D* situation, which means that the temperature differences are mainly caused by 2-*D* heat transfer effects.

Figure 5.11. Temperature differences compared to the middle for the 3-D experiment in set 2.
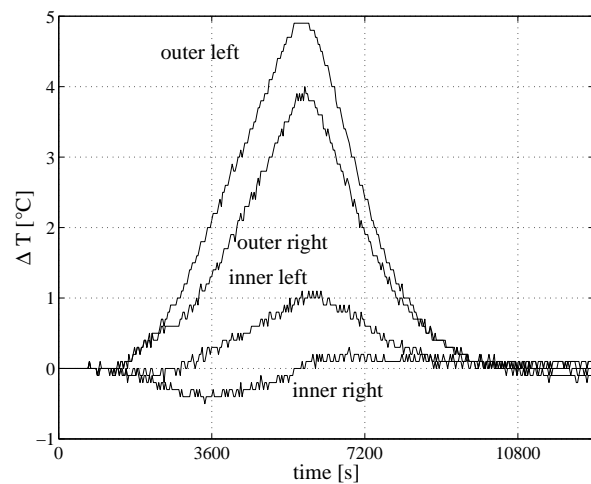
Figure 5.12. Temperature differences compared to the middle for the 2-D experiment in set 2.

For the measurements in set 3 the temperature differences compared to the middle of the product plate are graphed in Figure 5.13 and Figure 5.14. As can be seen in the figure, the differences are again about 5 [℃] for the outer thermocouples and about 1 [℃] for the inner thermocouples. As these differences are about the same as in set 2, it shows that the absolute temperature level is not of measurable influence to the temperature uniformity over the plate width. The difference between set 1 and set 2 is therefore likely to be caused by the difference in the ramp rate, which is an effect that will further be investigated in the next section. Also for set 3 the temperature differences are about equal for the 2-*D* and for the 3-*D* measurement. So, also in this measurement set 3-*D* effects appear to be negligible, despite the high temperatures.
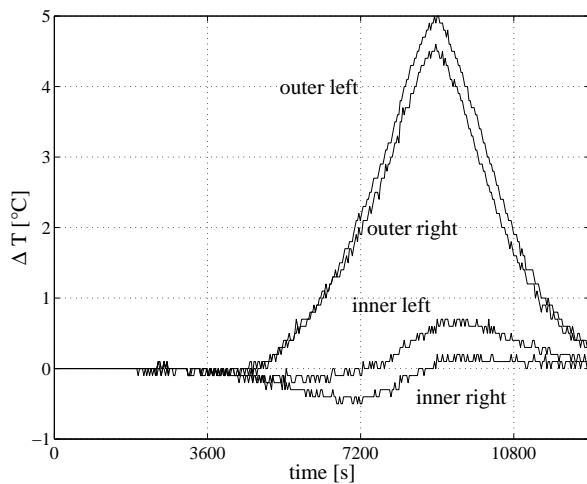

Figure 5.13. Temperature differences compared to the middle for the 3-D experiment in set 3.

Figure 5.14. Temperature differences compared to the middle for the 2-D experiment in set 3.

It can be concluded that for a ramp rate of 5 [℃/min] the maximum temperature over the width of the plate is about 5 [℃]. The absolute temperature level has no measurable influence to the temperature differences over the width of the plate. With respect to 3-*D* effects it can be concluded that they are of negligible influence to the temperature differences for the measurements in this section. An influence of the ramp rate on the temperature differences over the width of the plate is expected. This effect is investigated in more detail in the next section.

Influence of the ramp rate

The influence of the ramp rate is investigated by comparing set 3 to set 4. Both sets have the same set point temperature of 600 [℃], and the same axial gradient of 15 [min/zone] for the 3-*D* experiments. For set 3 with a ramp rate of 5 [℃/min], the temperature differences relative to the middle of the plate in zone 2 have already been given in Figure 5.13 and Figure 5.14. For a ramp rate of 8 [℃/min] (set 4) the temperature differences are given in Figure 5.15 and Figure 5.16.
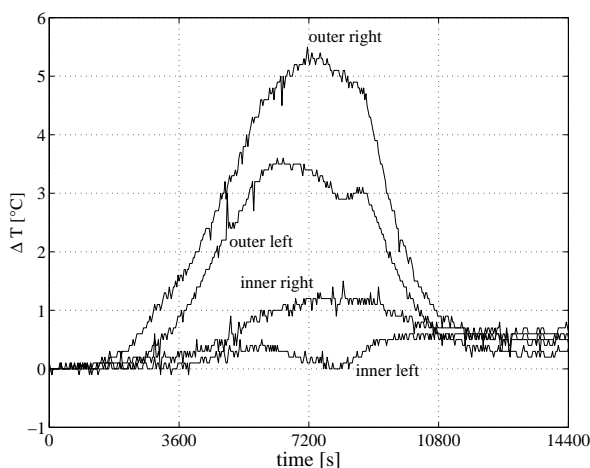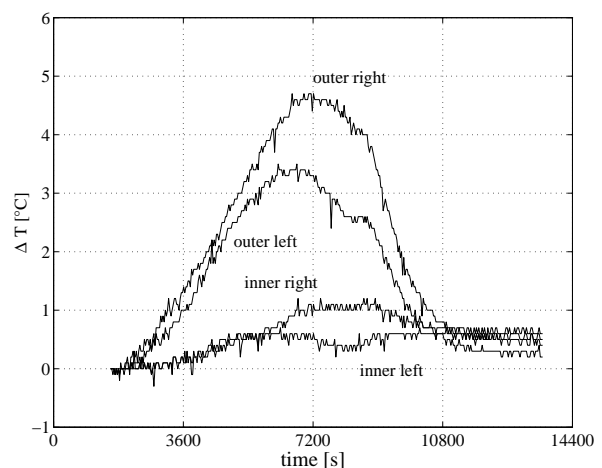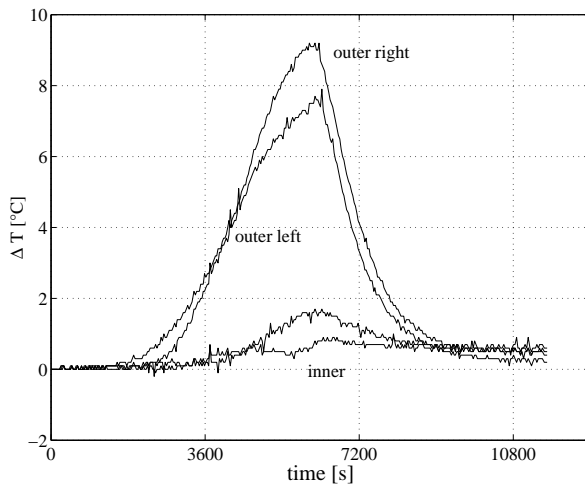

Figure 5.15. Temperature differences compared to the middle for the 3-D experiment in set 4.
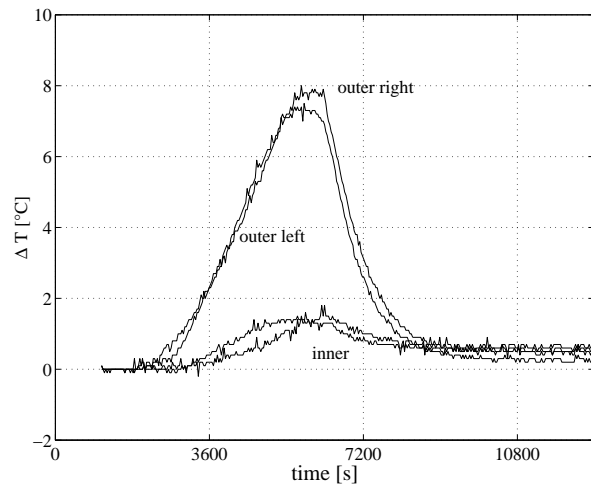
Figure 5.16. Temperature differences compared to the middle for the 2-D experiment in set 4.

For the outer right hand sides of the product plates the differences compared to the middle are about 9 [℃], while for the outer left hand sides this difference equals about 8 [℃]. The differences with the middle thermocouple for the inner side thermocouples are never larger than 2 [℃]. From comparing these results to the results of set 3 (Figure 5.13 and Figure 5.14), it can be concluded that the higher ramp rate causes higher temperature differences over the belt width. However, as can be seen in the figures, the differences between the 2-*D* and the 3-*D* measurement are still negligible. So also for the higher ramp rate 3-*D* effects appear to be of minor influence. Therefore the larger temperature differences when using a higher ramp rate must be caused by larger cross-sectional temperature gradients (2-*D* effects).

The increase of the 2-*D* effects for higher ramp rates can be understood using equation (4.2). For an increasing muffle temperature gradient in time, also the temperature gradient in time for the plates will increase. Because all the material parameters in equation (4.2) remain constant, an increasing plate temperature gradient must result in an increasing temperature difference between the muffle and the plates. This shows that for higher ramp rates the 2-*D* effects are increased. This is also confirmed by comparing measurement set 3 to set 2 and set 1. Despite a different set point temperature, the temperature differences

are about the same for set 2 and set 3, which also have the same ramp rate. In set 1 the ramp rate is less, and also the temperature differences are lower.

Influence of the axial temperature gradient

At last the influence of the axial temperature gradient is investigated by comparing set 4 to set 5. The axial temperature gradient in the test-rig was varied from 15 [min/zone] in set 4 to 25 [min/zone] in set 5. The increased value in set 5 resulted in a temperature difference of approximately 120 [℃] between neighbouring zones.

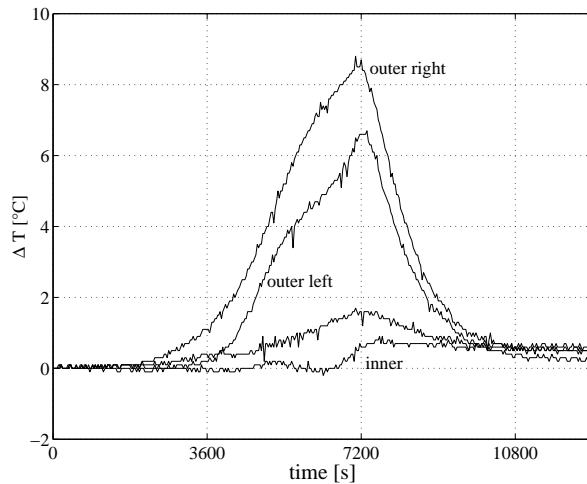*Figure 5.17. Temperature differences compared to the middle for the 3-D experiment in set 5.*
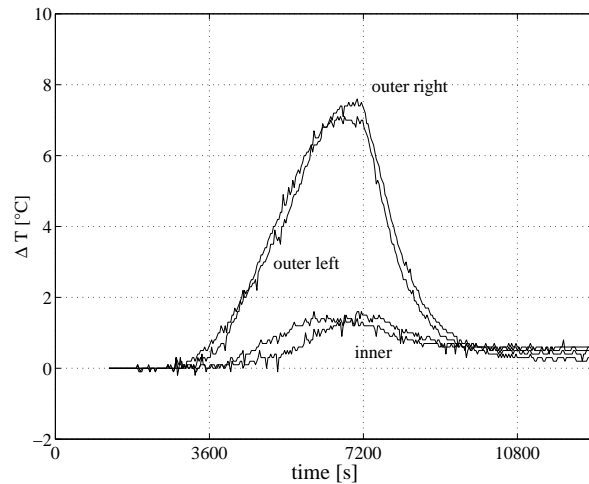
Figure 5.18. Temperature differences compared to the middle for the 2-D experiment in set 5.

The temperature differences between the thermocouples at the sides and the thermocouple in the middle of the product plate in zone 2 were determined. These temperature differences are graphed in Figure 5.17 and Figure 5.18. As can be seen, there is hardly any difference between the temperature differences found in set 4 (Figure 5.15 and Figure 5.16) and the results for set 5 with the higher axial gradient. Therefore, it is concluded that the higher axial temperature gradient had no effect on the temperature uniformity over the belt width, and that 3-*D* heat transfer effects in this case were negligible again.

Conclusions with respect to 3-D effects

From the measurements described above, it can be concluded that the absolute temperature level and the axial temperature gradient have only minor influence to the temperature differences over the width of the plates. Only the ramp rate appeared to have a significant influence to these temperature differences. Apparently an increasing ramp rate results in increasing 2-*D* heat transfer effects, while it does not have any consequences for 3-*D* effects. The influence of 3-*D* radiation effects is analyzed in more detail in the next section.

5.3 Estimation of the 3-D source terms

The 3-*D* effects in the furnace can be split up into 3-*D* radiative effects and 3-*D* convective effects. From the measurements in this section the total influence of 3-*D* heat transfer effects on the temperature uniformity of the belt appears to be negligible. This is however no prove that both 3-*D* radiation and 3-*D* convection are of negligible influence. Theoreti-

cally, radiation and convection might be two cancelling effects in the situations measured, while the effects themselves can be of major importance when treated separately. So for concluding that both effects are negligible, it has to be shown that one separate effect itself is of minor importance. In this section the 3-*D* radiative heat transfer is analysed numerically using a simplified 3-*D* radiation model, which is based on view factor calculations. This simplified model cannot handle complex geometries and material properties, but it is good enough to give an estimation of the 3-*D* radiation effects in the furnace. Explicit details about this model can be found in Verhaar (1999).

In the simplified radiation model, the muffle is treated as a rectangular box with diffusely reflecting walls. The bottom of the box is formed by the product plates, which in general have a low temperature, while the other walls of the box correspond to the upper part of the muffle in the test-rig. For determining the 3-*D* radiative heat transfer effects, a 3-*D* calculation has to be compared to a 2-*D* one. Calculating a 2-*D* radiation problem in the box can be done by modelling mirroring head ends. However, specular reflection is not available in the simplified model, and therefore making a 2-*D* radiation calculation with the simplified 3-*D* model is not easy. An approximation of the 2-*D* situation can be made by using diffuse reflective head ends. In this case the heat flux to the belt will be underestimated near the head ends, but for a box with a large enough axial dimension only a small difference with the 2-*D* situation is to be expected in the middle. Therefore first a 2-*D* situation is simulated with diffusely reflecting head ends in the 3-*D* radiation model, and the heat fluxes in the middle of the box are compared to a 2-*D* calculation using an analogous model with 2-*D* view factors. In this way the influence of the diffuse reflecting head ends is estimated, and it is also a validation of the 3-*D* model, since for a large enough axial dimension the results should approximately be the same. When both results for the heat fluxes agree, the influence of axial temperature gradients on the heat flux is investigated with the 3-*D* model.

Figure 5.19. Simple 2-D radiation problem.

The 2-*D* radiation problem analyzed is depicted in Figure 5.19. It consists of a rectangular geometry with a bottom wall of 150 [℃] and the other walls at 270 [℃]. In order to calculate a geometry similar to the test-rig, the width of the rectangle equals 340 [mm], and the heigth is 180 [mm]. The emission coefficient equals 0.4 [-] for all the walls. In the 3-*D* calculation also a geometry with the dimensions of the test-rig is used. Therefore, the axial length of the geometry equals 900 [mm] (3 zones), and the head sides are modelled as diffuse reflectors. For both the 2-*D* and the 3-*D* approach, the heat flux to the belt in the middle cross section was calculated. The results are depicted in Figure 5.20.

Figure 5.20. Heat flux to the bottom for the 2-D radiation problem, calculated with the 2-D and the 3-D model.

Comparing the graphs one can conclude that the 3-*D* model with diffusely reflecting head ends gives an underestimation of the

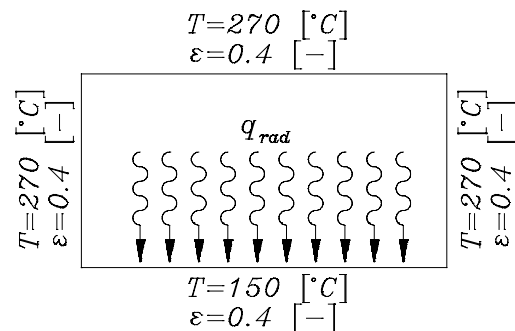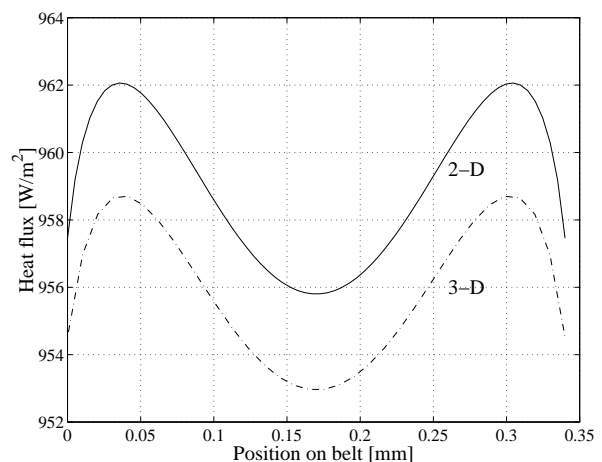2-*D* situation, as expected. However, the difference in the absolute values of the heat flux is only about 0.3%. Furthermore, the difference between the graphs is quite equal over the belt width. This means that the calculated temperature differences over the width of the belt are similar for both situations, and that the 3-*D* model can be used to investigate the effect of 3-*D* effects on the uniformity over the belt width.

A comparison between a 2-*D* and a 3-*D* situation was made using the 3-*D* model. The 2-*D* situation is the same as already mentioned in Figure 5.19, and the heat fluxes for the 2-*D* calculation determined with the 3-*D* model from Figure 5.20 are used as the 2-*D* heat fluxes in the comparison. In the 3-*D* situation a temperature gradient of 50 [℃] per zone was prescribed, by using the global data given in Table 7. In axial direction linear temperature profiles were prescribed to get a smooth profile as in a practical situation.

In Figure 5.21 the heat flux to the bottom in the middle of the furnace is plotted. As can be seen, for the 3-*D* situation the heat flux is larger than for the 2-*D* situation. The systematical difference between the two profiles can be explained because radiation is proportional to the difference in fourth powers of the surface temperatures. Therefore, the extra heat flux that the belt in zone 2 gains from zone 3 is more than the amount it gets less from zone 1. However, a higher over-all heat transfer will necessarily not cause extra temperature differences over the width of the belt. Extra temperature differences are caused by differences in the shape of the heat transfer profiles. Therefore, in Figure 5.22 the relative difference between the two heat flux profiles is shown. This relative difference is calculated by

Furnace wall		T [℃]	ε [-]
Muffle	Front	170	0.4
	Zone 1	220	
	Zone 2	270	
	Zone 3	320	
	Rear	370	
Belt	Zone 1	100	0.4
	Zone 2	150	
	Zone 3	200	

Table 7. 3-D test case used for determining 3-D radiation sources.

dividing the difference between the 3-*D* and the 2-*D* solution by the 3-*D* solution. The difference varies between 6.7% at the sides to 7.65% in the middle of the belt. It is concluded that there is a systematical difference of 6.7%. Extra differences in the profiles are at most about 1%.
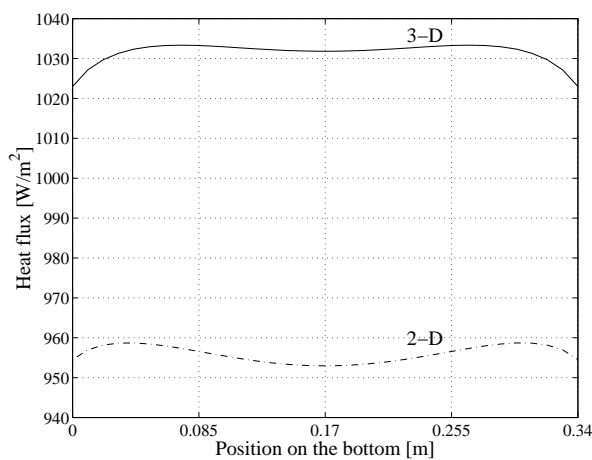

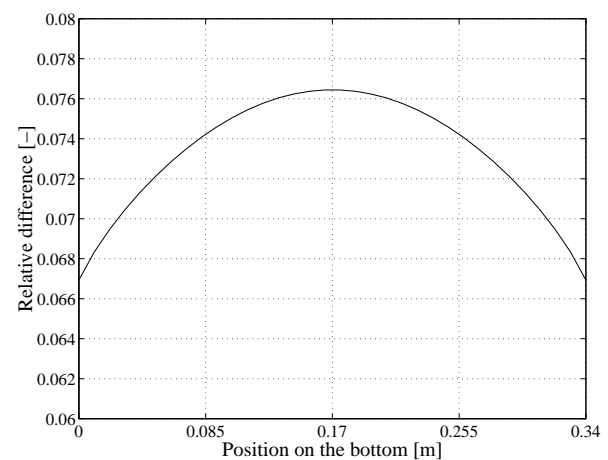*Figure 5.21. Heat flux to the bottom wall for the 2-D and the 3-D situation.*

Figure 5.22. Relative difference between the 2-D and the 3-D heat flux.

In order to estimate the influence of the difference in the heat flux on the uniformity of the temperature profile of the belt, two nearly identical calculations with the design tool of section 6.1 were done. In one calculation the 3-*D* effects are not taken into account, while in the other calculation the 3-*D* effects of Figure 5.22 are taken into account as 3-*D* source terms. In Figure 5.23 the temperature differences over the width of the belt are given for both calculations. As can be seen, there is hardly any difference in the absolute values of the temperature differences for both situations. When 3-*D* effects are taken into account, the maximum temperature differences occur a little bit earlier in time, because in this situation the heat flux to the belt is also systematically higher, which results in a faster heating.
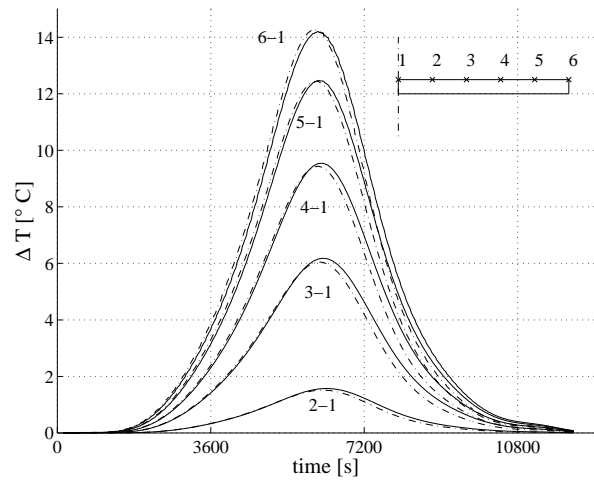
Figure 5.23. Temperature differences over the width of the belt without (solid) and with (dash-dot) 3-D radiation effects taken into account.

Therefore, one can conclude that 3-*D* effects have a significant effect on the absolute value of the heat flux to the belt, but are of negligible influence to the temperature differences over the width of the belt. This supports the statement that not only the sum of 3-*D* radiation and convection effects is negligible, but also each of the effects separately.

CHAPTER 6. DESIGN OPTIMIZATION

As the purpose of the numerical model is to serve as a design tool, fast calculations with an accurate prediction of the temperature differences over the belt width are aimed at. In the previous chapter, the influence of 3-*D* heat transfer effects on the temperature uniformity over the width of the belt appeared to be negligible. However, in the model still all the 2-*D* heat transfer effects are taken into account. Therefore, the model remains complex and calculations with the model are still very time consuming. In this chapter the order of magnitude of the various 2-*D* heat transfer modes will be analyzed and further simplifications to the model are made. After that, furnace calculations are done with the simplified model. The influence of various model parameters on the temperature uniformity over the width of the belt is investigated, and the influences of some design measures are discussed. At last a design proposal for a real conveyor belt furnace is given.

6.1 The design tool

The calculation of the flow in the furnace is the most time consuming part. This is caused by the very strong buoyant effects, as explained in section 3.3. Although the convective effects are strong, the influence of the flow phenomena on the heat transfer to the belt may be relatively small. In order to investigate the importance of convective effects in disturbing the temperature uniformity of the belt, the same furnace calculation as in section 3.5 is done, with the only difference that the gravity is set to zero. In this way only radiative and conductive heat transfer will warm up the belt. In Figure 6.1 the calculated temperature differences compared to the middle of the belt as a function of time are given. As can be seen in the figure the maximum tempera-

Figure 6.1. Temperature differences over the width of the belt, calculated without convective effects.

ture difference is about 19 [℃]. As expected, this difference occurs between the outer corner point and the middle of the belt. The differences decrease for positions nearer to the middle of the belt, but for none of the positions the differences are negligible.
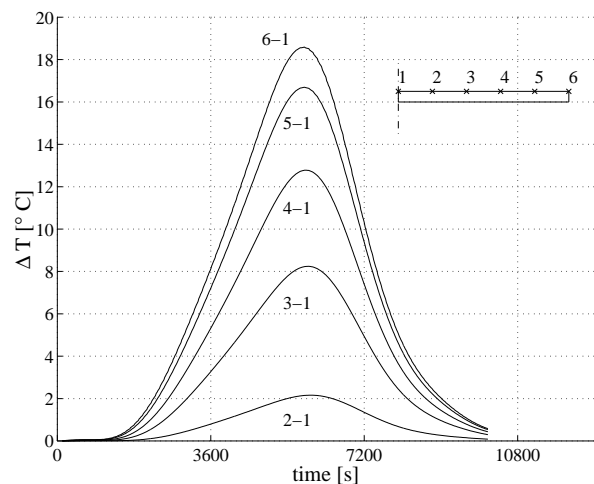
Comparing this to the result with convection taken into account, as shown in Figure 3.13, it can be concluded that convection has a decreasing effect on the temperature differences over the width of the belt. For the situation with convection, a maximum difference of 13 [℃] is calculated, so that the reducing effect of convection on the temperature differences in this case is about 30%. For both situations, the side of the belt is hotter than the middle. Therefore, the lower temperature differences with convection taken into account show that convective heat transfer is stronger in the middle of the belt than at the sides. This is due to the fact that the difference between the belt temperature and the air temperature is higher in the middle of the furnace than at the side. This variation in the temperature difference between the air and the belt surface is partly caused by the non-uniform plate temperature. For a uniform plate temperature the differences in convective heat transfer are expected to be less. Therefore, convection is assumed to be an adjusting effect instead of a main effect that disturbs the temperature uniformity over the width of the belt. Because calculating the convective heat transfer effects also costs a lot of computation time, they are not taken into account in the design tool. The design tool then still covers

the main disturbing effects, and it is suitable for optimizing the temperature uniformity inside the furnace.

For further simplification, it is investigated whether conduction through the medium is also negligible compared to radiative heat transfer. This is done by taking only the radiative fluxes into account when calculating the same furnace problem as above. The calculated temperature differences are given in Figure 6.2. Comparing Figure 6.2 to Figure 6.1, it appears that the calculated temperature differences for the two situations are significantly different. Therefore, it is concluded that conductive heat fluxes through the medium are not negligible. However, still a simplification to the model can be made with respect to the calculation of the conductive heat fluxes. In Figure 6.3 a typical contour plot for the temperature in a muffle cross-section is given. From the figure, it is clear that the temperature gradients are much larger at the side of the belt than at the top and bottom surfaces. Therefore, at the side of the belt conductive effects are strong, while at the top and bottom surfaces the conductive effects are relatively small. The conduction can be calculated in a simple way by Fourier's law. Instead of performing the complete finite element calculation for solving the energy equation, in the design tool conductive heat transfer is calculated only at the side of the belt as

$$q_k = -k \frac{\partial T}{\partial x}. \qquad (6.1)$$

The temperature gradient is approximated by dividing the temperature difference between the muffle side and the side of the belt by the distance between them. The calculated temperature differences using this simplified approach for the conductive fluxes are shown in Figure 6.4. As can be seen, the figure shows hardly any differences with Figure 6.1. This shows that calculating the conductive fluxes using Fourier's law at the side of the belt is a suitable simplification. It will be used in the design model instead of solving the energy equation.
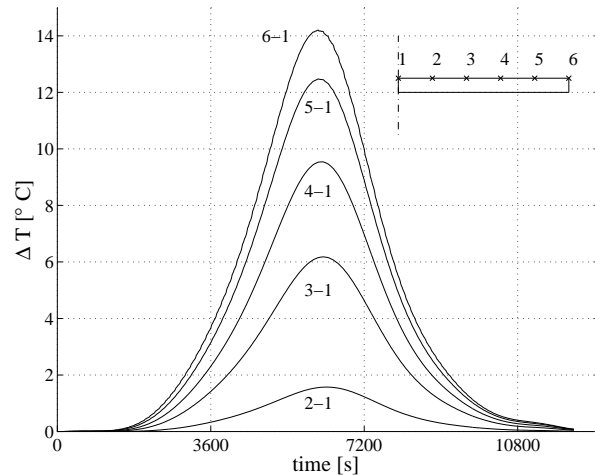

Figure 6.2. Temperature differences over the width of the belt when only radiative heat transfer is taken into account.
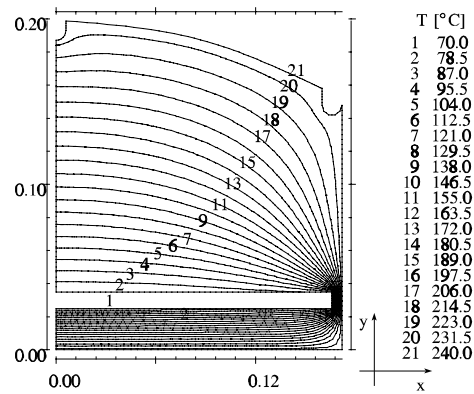

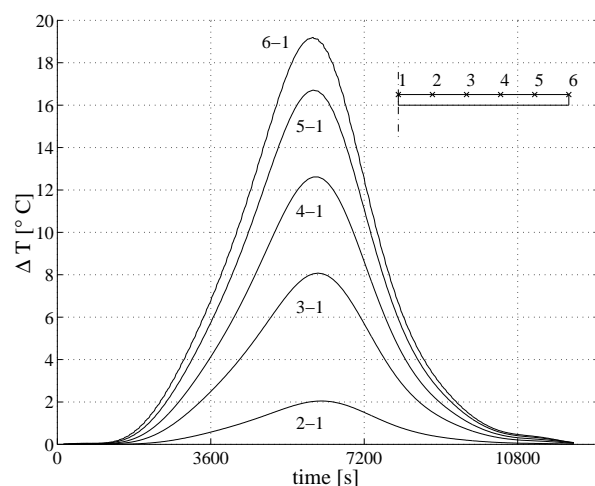*Figure 6.3. Contour lines for the temperature in a muffle cross-section.*

Figure 6.4. Temperature differences over the width of the belt, calculated without convective effects, and by using Fourier's law for the conduction at the side of the belt.

Comparison of the design tool to a measurement

The time-dependent muffle temperature profile in measurement set 2 was prescribed in the unsteady marching model in order to calculate the temperature profile of the product plates. In section 3.5, this was already done for the complete furnace model including convective heat transfer. For the same calculation done using the simplified design tool, the temperature differences are presented in Figure 6.4. The result of this calculation is compared to a measurement in Figure 6.5 and Figure 6.6. The calculated and measured temperature profiles in time are depicted in Figure 6.5, and the temperature differences over the belt width are shown in Figure 6.6.
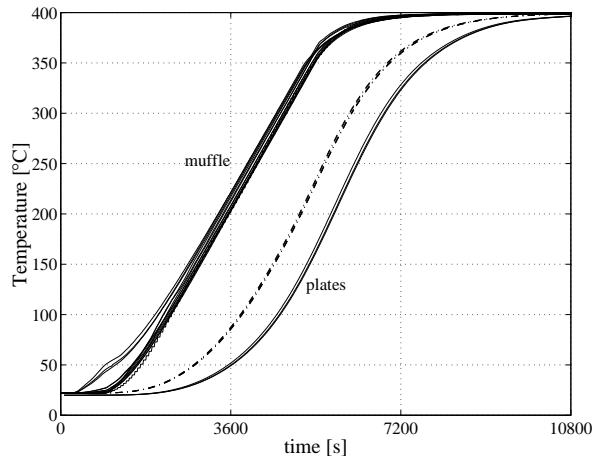

Figure 6.5. Muffle temperature profile, and measured (dashdot) and with the design tool calculated (solid) plate temperature profiles.
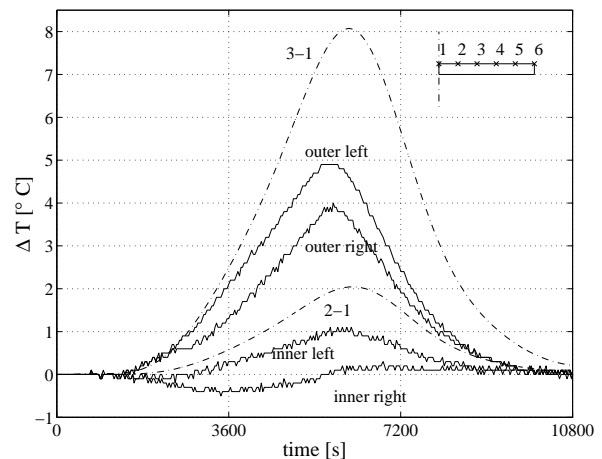
Figure 6.6. Measured (solid) and with the design tool calculated temperature differences (dashdot) at similar positions.

Figure 6.5 shows that in the measurement the plate warms up faster than calculated. This was also the case for the calculation with the complete model in section 3.5 (Figure 3.8), but now the differences between the measured and the calculated temperature histories are larger. This can be explained, because in the design tool the convective heat fluxes are not taken into account. The measured and calculated temperature differences over the width of the belt are shown in Figure 6.6. The calculated temperature differences using the design tool are approximately 3 [℃] higher than measured, which could also be expected, as in the design tool convective heat transfer is not taken into account.

6.2 Influences of the various heat transfer modes

In this section the design tool will be used to seek for an ideal furnace configuration, having a theoretical uniform temperature distribution over the width of the belt. Using the design tool the temperature differences over the width of the belt can be calculated as a function of the modelled heat transfer effects. By ruling out the several heat transfer effects one by one, insight is acquired on the maximum improvements that can be gained by reducing a certain heat transfer effect in a real furnace. It is tried to get as close as possible to an ideal situation with no temperature differences over the width of the belt.

As a reference the standard situation with all significant heat transfer effects involved is taken. The muffle temperature history used for all muffle walls is the profile of the muffle bottom in measurement set 2, being a realistic temperature profile going up to 400 [℃]. The result of this calculation was already shown in Figure 6.4.

No conduction from the sides

In order to find out which part of the temperature differences determined in the previous section is caused by conduction to the side of the belt, the same calculation was done with the conduction to the side of the belt being set to zero. This calculation was already presented in section 6.1, and the temperature difference graphs are depicted in Figure 6.2. From a comparison between Figure 6.2 and Figure 6.4 it appears that the maximum temperature difference obtained decreased to 14 [℃], so the conductive effect is responsible for about 5 [℃] at the side of the belt. Further to the middle of the belt the influence of the side conduction is less, as could be expected. From this result one can conclude that conduction from the sides has indeed a non negligible influence. However, by decreasing the conduction to the side of the belt, the temperature differences will decrease about 5 [℃] maximum. So one cannot build a uniform furnace by only decreasing the conductive effects at the sides. The remaining radiative effects appear to be more important, and therefore deserve more attention at this point.

No radiation and no conduction from the sides

Just like the conductive effects, also radiative heat transfer will appear at the side of the belt. Because heat transfer from the side of the belt will always disturb uniformity, a calculation was performed by setting the radiative fluxes to the sides of the belt to zero. This was done by modelling the side of the belt as a perfect mirror. The temperature differences calculated for this situation are depicted in Figure 6.7. As can be seen from the figure, the temperature differences have further decreased to about 5 [℃]. This is an improvement of about 9 [℃] maximum, showing that radiative heat fluxes through the sides of the belt play a very important role. Still disturbances in the temperature uniformity exist in this case. As the sides of the belt gain no heat fluxes any more, the remaining temperature differences must be caused by a non-uniform heat flux to the top and the bottom of the belt.
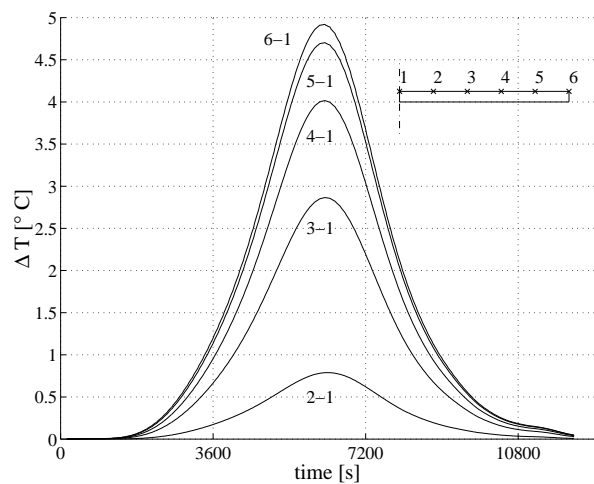
Figure 6.7. Temperature differences without conduction and radiation to the sides of the belt.

The non-uniformity in the heat flux can be caused by the reflection of radiation from the belt against the muffle. Because the muffle walls are reflective, radiation from the belt is reflected against the muffle walls and will partly fall back on the belt. In this way, the belt sees itself by reflection of radiation against the muffle walls. This effect will be stronger in the middle of the belt than at the sides. In the middle, more radiation will be reflected back to the belt directly via the muffle roof, while at the sides more radiation will be reflected back in two steps, first hitting a side-wall and then the roof. In this two step reflection less energy will be sent back to the belt, and the reflection effect is less strong. In order to check this effect another calculation was done.

A black muffle, no radiation and no conduction from the sides

As a black muffle is non-reflective, the non-uniformity caused by reflections against the muffle will disappear when doing a calculation with a black muffle. The muffle wall emission coefficients were all set to unity, and the calculation was started again. It is worth mentioning that in this case the belt itself still has the same reflective properties as in the previous calculations. The calculated temperature differences are now depicted in Figure 6.8. The remaining temperature differences are smaller than the numerical cut-off accuracy used in the routines, and are also completely negligible. Therefore, it can be concluded that in this situation no disturbing effects are present any more.
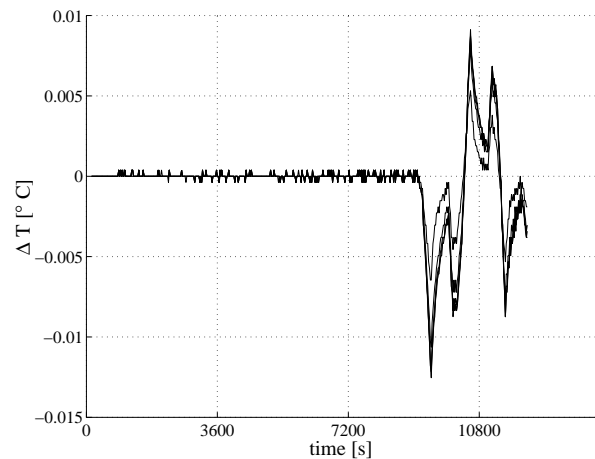

Figure 6.8. Temperature differences for a black muffle without heat fluxes to the side of the belt.

Analysis of the influence of the disturbing effects

As seen above, conductive and radiative fluxes through the sides of the belt and reflection of radiation against the muffle are the main causes for temperature differences over the width of the belt. By subsequently ruling out separate effects, an optimization path was followed to a theoretically uniform furnace design. An estimation of the influence of each separate disturbing effect on the temperature uniformity was determined by comparing the subsequent steps in the optimization path. However, the disturbing effects could have been ruled out in any other order, and any different path could have been followed to the ideal solution. As the several disturbing effects are not necessarily independent, following another optimization path might result into different values for the influences of the separate disturbing effects. In order to get a better idea about the separate influences, the temperature uniformity for each possible combination of disturbing effects has been calculated. In the top row of Table 8 all the possible combinations of disturbing effects are given (cond. = conductive fluxes through the sides of the belt, rad. = radiative fluxes through the side of the belt and ref. = non-uniform reflections of radiation against the muffle). In the second row the maximum temperature difference for each combination is given. Now the influence of each separate effect can be calculated by comparing combinations. This is done in the lower part of Table 8. For each cell, the left and right overlapping combinations just differ by one separate disturbing effect, which is shown in the left column of Table 8. The influence of this effect is determined by subtracting the temperature differences of the combinations. For each separate disturbing effect the influence is determined in four ways. As can be seen in Table 8, for each separate disturbing effect its influence is independent on the compared combinations within a range of about 1 [°C]. Therefore, it can be concluded that the several disturbing effects are more or less independent. The influence to the temperature uniformity is 4 to 5 [°C] for non-uniform reflections, 9 to 10 [°C] for radiative fluxes through the sides of the belt and about 5 [°C] for conductive fluxes through the sides of the belt.

Active disturbing effects	Cond. Rad. Ref.	Cond. Rad.	Cond. Ref.	Cond.	Rad. Ref.	Rad.	Ref.	None
ΔT_{max} [°C]	19	15	10	5	14	11	5	0
Influence of separate effects by subtraction of combined influences.								
Ref.	4		5		3		5	
Rad.	9							
		10						
					9			
							11	
Cond.	5							
		4						
			5					
				5				

Table 8. Influence to the temperature uniformity for all the possible combinations of disturbing effects and derived influences of the separate effects.

Design conclusions

As can be concluded from the analyses, a uniform furnace can be built by preventing all heat fluxes to the sides of the belt and by using a non-reflective muffle. However, this is a theoretical ideal situation, which cannot be realized in practice. A completely black muffle material might not exist, and a perfect mirroring belt side which also blocks all conductive heat transfer is not realizable in practice. However, the analyses have shown the influence on the temperature differences of each effect. It can be concluded that radiative effects are the most important cause for a non-uniform temperature profile over the width of the belt. Therefore, the most attention has to be paid to radiative effects, especially radiative fluxes to the sides of the belt. Besides, it is shown that convection has a reducing effect on the temperature differences over the belt width. Now one can try to build a furnace which resembles the ideal furnace as much as possible. Remaining temperature differences can then be minimized by other measures.

6.3 Design measures for improving the furnace design

In this section, practical measures for minimizing the disturbing effects will be mentioned. For determining the influence of a practical measure on the temperature distribution over the width of the belt, the practical measure is implemented in the theoretical ideal furnace. Then the practical measure is the only difference between the furnace calculated and an ideal furnace, and the temperature differences over the width of the belt are then purely caused by the deviation from the ideal situation caused by the practical measure. In this way, the sensibility for deviations from the theoretically ideal situation is investigated, and practical demands on the design are determined.

Minimization of the heat fluxes through the sides of the belt

Radiation shields at the sides of the belt

Using radiation shields, the radiative fluxes to the side of the belt can be minimized. The radiation shield is a vertical plate placed at the side of the belt. It must have a high reflection coefficient so that most of the radiation from the muffle sides is reflected instead of transported to the belt. For temperatures up to 600 [℃], aluminium is a suitable material because of its good reflective properties ($\varepsilon < 0.1$ [-] for a polished plate). The expected maximum temperature differences caused by heat fluxes through the radiation shields are calculated with the design tool. In stead of prescribing a heat flux equal to zero at the side of the belt, a radiation shield is implemented as a specular reflector with $\varepsilon = 0.1$ [-]. As can be seen in Figure 6.9, the maximum temperature difference approximately equals 3.5 [℃].
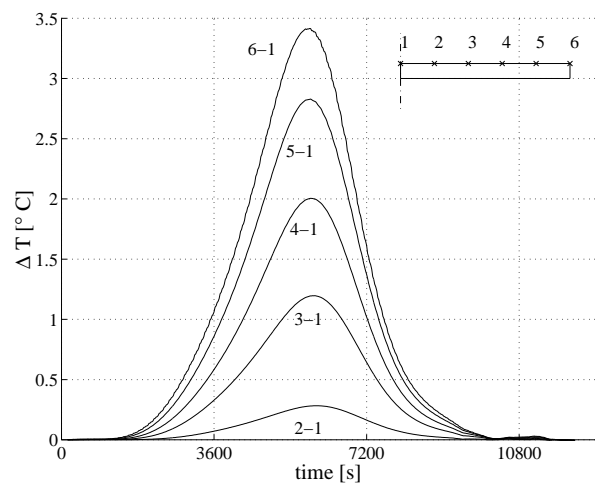
Figure 6.9. Temperature differences over the width of the belt when using radiation shields at the sides of the belt.

Minimization of the conduction heat transfer to the sides

This heat transfer mode is probably the hardest to decrease using practical measures. Because of the openings for the belt at both ends of the furnace, a vacuum environment is not possible in a conveyor belt furnace. A suitable solution is to use a gas with a low conduction coefficient. The best possible gas for this purpose is xenon gas. It is an inert gas, so it will not influence most production processes, and it is a very good insulator in comparison to other gases (Lide, 1994). It has a heat conduction coefficient that is less than 1/4 of the value for air, as depicted in Table 9.

T [K]	k_{air} [mW m^{-1} K^{-1}]	k_{xenon} [mW m^{-1} K^{-1}]
100	9.4	2.0
200	18.4	3.6
300	26.2	5.5
400	33.3	7.3
500	39.7	8.9
600	45.7	10.4

Table 9. The conduction coefficient for air and xenon at several temperatures (Lide, 1994).
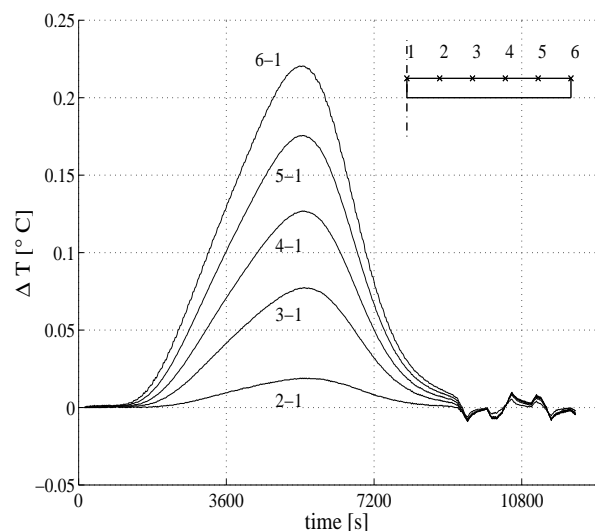
Figure 6.10. Temperature differences for xenon gas as medium inside the muffle.

With the given values for the conduction coefficient of xenon, a furnace calculation was done. In Figure 6.10 the temperature differences compared to the middle of the belt are plotted. The maximum temperature difference is only about 0.22 [℃], which is very low compared to the 5 [℃] difference caused by conduction when the muffle is filled with air (Table 8). One can conclude that using xenon gas instead of air is nearly as good as having no conductive effects, and that it is a very good medium for reducing the conductive effects at the sides of the belt.

As there might be production processes in which no xenon gas is allowed, or that require another conditioned atmosphere, an alternative for minimizing the conductive heat transfer to the sides of the belt is necessary. Another way of reducing the side conduction is local cooling. One can construct air cooled pipes along the sides of the conveyor belt, that are controlled in such a way that they drain away the right amount of energy to the environment. This amount of energy can again be calculated using the design tool, as the heat fluxes to the sides of the belt are calculated every time-step. In Figure 6.11 the conductive heat flux to the side of the belt is graphed against time for the standard situation as used in section 6.2.
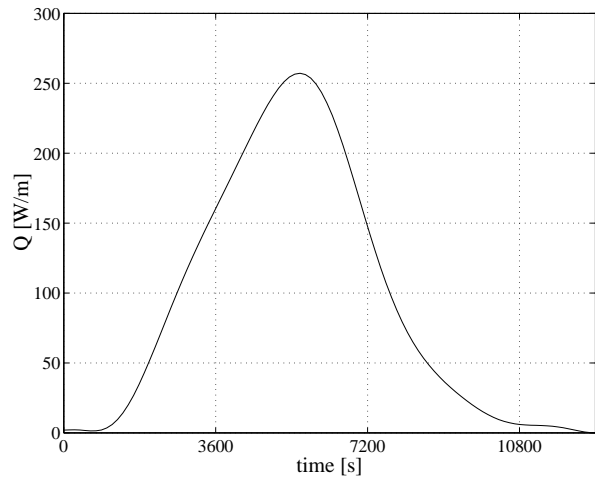

Figure 6.11. Conductive heat flux per unit of furnace length to the side of the belt.

As the heat flux is a function of time, and therefore also of axial position in a real furnace, the cooling system must be constructed to have several control units over the furnace's axial length. One might think of separate cooling units for each zone of the furnace.

Minimization of the reflections against the muffle

The non-uniform reflections against the muffle can be decreased by coating the muffle. In industry, ceramic coatings are available that have an emission coefficient of $\varepsilon > 0.9$ [-]. Therefore, a calculation is done with the emission coefficient of the muffle equal to $\varepsilon = 0.9$ [-]. In Figure 6.12 the calculated temperature differences over the belt width are given. As can be seen, the maximum temperature difference is less than 0.4 [℃], so a muffle emission coefficient of 0.9 is nearly as good as a totally black muffle.
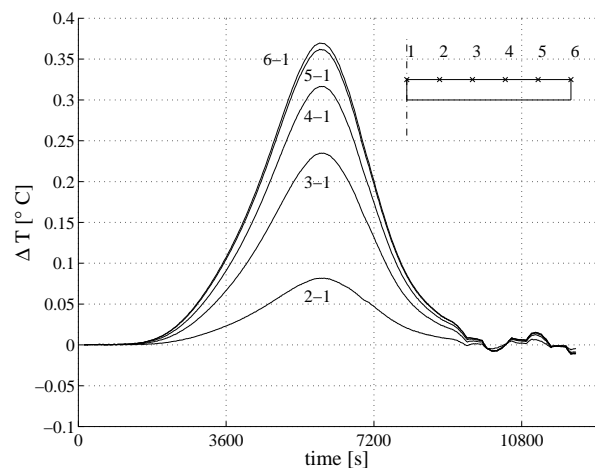

Figure 6.12. Temperature differences over the width of the belt for $\varepsilon_{muffle} = 0.9$.

Additional improvement measures

Controlling of the heating elements

Because of heat fluxes from the muffle sides to the sides of the belt, and also because of non-uniform radiative fluxes caused by reflection of radiation against the muffle walls, the belt temperature will be higher at the sides of the belt than in the middle. It might therefore be possible to decrease these disturbing effects by setting the side temperatures of the muffle to a lower temperature than the top and bottom temperatures. In an industrial

conveyor belt furnace, this can be done by using a lower setpoint temperature for the controllers of the side elements. In the test-rig, a lower side temperature can be realized by shifting the temperature histories for the side elements, which is easily done by switching on the side elements later than the top and the bottom elements. The best value for the time shift for the side elements can be determined using the design tool. The same muffle temperature history and furnace properties as in the beginning of this chapter were used as a standard situation in order to test the effect of shifting the side elements. The temperature differences relative to the middle of the belt without using a shift have been calculated to be about 19 [℃] (Figure 6.4).

In Figure 6.13 and Figure 6.14 the calculated temperature differences are depicted for two different time shift values for the side elements. As can be seen in the figures, shifting the side element temperature profiles influences the temperature differences as expected. Because during the warming up period the side elements are colder than the top and the bottom, first the temperature differences will have a negative value, which points at a lower belt temperature at the side of the belt than in the middle. Later in the heating traject the heat fluxes to the sides of the belt will get stronger, just like in the situation without a shift, and the temperature differences become positive again. However, they will not increase to the value of 19 [℃] obtained without a shift any more. The maximum temperature difference relative to the middle can be minimized by using such a time shift that the negative and positive temperature differences have about the same values. As shown in Figure 6.14 for this situation the best shift is about 2600 [s]. This shift value is highly situation dependent, so for other furnace configurations or muffle temperature histories the value has to be determined again by new design tool calculations. From this, one can conclude that shifting the side element temperature profile will not decrease the temperature differences to zero. In fact the differences remain, but one can shift them into positive and negative regions to minimize their maximum absolute values.
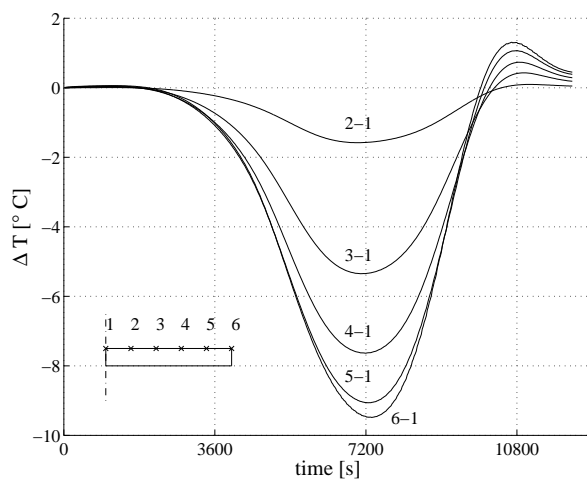

Figure 6.13. Temperature differences using a time shift of 4000 [s] for the side elements.
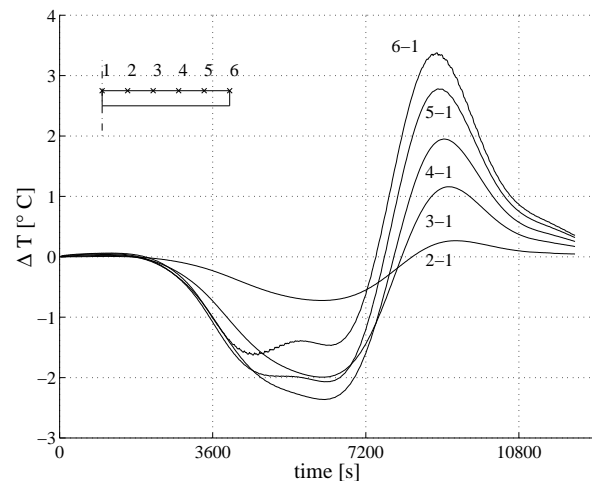
Figure 6.14. Temperature differences for a time shift of 2600 [s].

Shape of the muffle

The curved shape of the roof of the muffle is a very characteristic property of industrial conveyor belt furnaces. The roof is made curved for gaining mechanical strength, especially when high temperatures are needed and material becomes weaker. In this section the influence of this curved shape on the radiative heat transfer is investigated.

A cross-section of the muffle as used in the experimental setup is given in Figure 6.15. The radiative heat fluxes for this muffle have been calculated using the radiation model. Also two muffles with a flat roof have been calculated, of which the positions are depicted in Figure 6.15 by the dashed lines. For all the calculations the muffle temperatures were set to 600 [°C], while the temperature of the belt equals 400 [°C]. The emission coefficient of the muffle and the belt was set to 0.38. To investigate the influence of specular reflections, calculations were carried out for pure diffuse reflection (mirror coefficient $s_w = 0$) and for 68% specular reflection ($s_w = 0.68$).
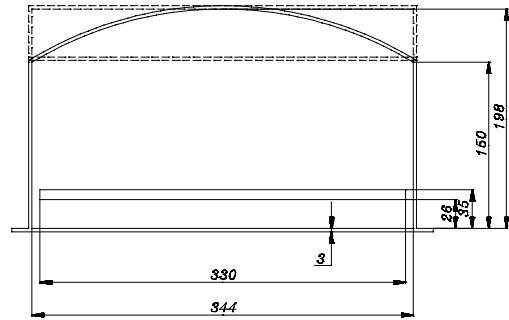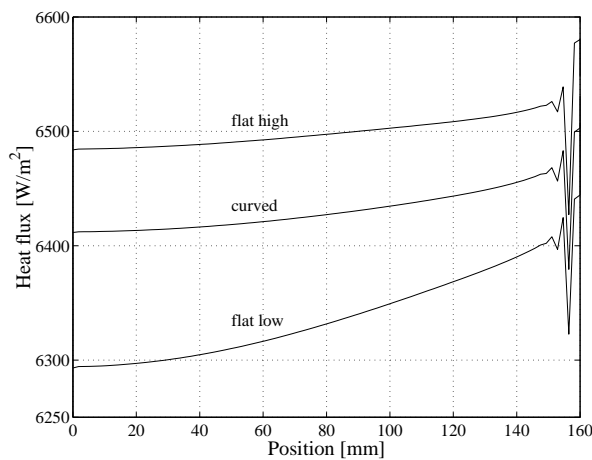
Figure 6.15. Scaled shape of the muffle.

Figure 6.16. Heat fluxes to the belt for the three different muffle shapes with purely diffuse reflections.
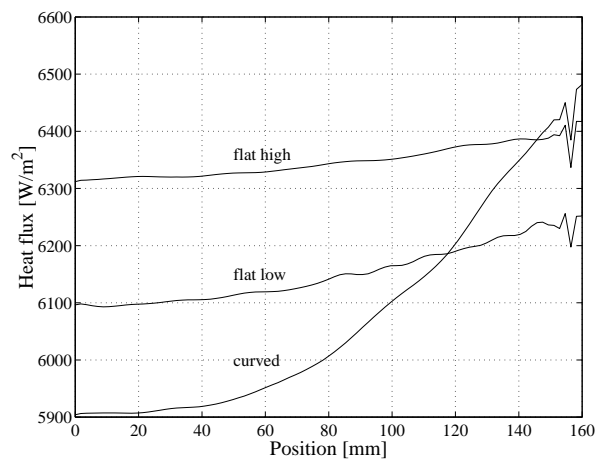
Figure 6.17. Heat fluxes to the belt for the three different muffle shapes with partly specular reflections.

In Figure 6.16 and Figure 6.17 the heat flux to the belt as function of the position is depicted for the three different muffle shapes and for the two values of the mirror coefficient. As can be seen in Figure 6.16, for diffuse reflections the heat transfer depends significantly on the height of the muffle. The heat flux for the curved roof is in between the values of the heat flux for the high and low muffles with a flat roof. For specular reflections (Figure 6.17), the curved shape of the muffle roof has a significant influence on the heat transfer. The flux for the curved roof varies much more over the width of the belt, and therefore, a flat roof is preferred in case of specular reflections. Also the total amount of heat transfer with specular reflections is slightly less than in the case with diffuse reflections. As mentioned in section 6.2, for a uniform temperature distribution of the belt the reflection coefficient of the muffle has to be as low as possible. As the influence of the curved roof on the heat flux to the belt depends on the radiative reflections against the muffle, for a muffle with a low reflection coefficient also the influence of the curved roof on the temperature distribution over the width of the belt is expected to be low. Therefore, in an optimized furnace a muffle with a curved roof is expected to give no problems with respect to the temperature uniformity.

6.4 Calculation of an optimized furnace

Using all the design improvements as given in the previous section, an optimized design can be calculated. In this way an estimation is given of the temperature differences that will remain in a real optimized furnace. The optimized furnace design contains a muffle with an emission coefficient equal to 0.9, radiation shields at the sides of the belt (emission coefficient equal to 0.1 and specularly reflecting) and a xenon atmosphere. The calculated temperature differences over the width of the belt are given in Figure 6.18, both for the optimized and for the non-optimized furnace. As can be seen in the figure, the maximum temperature difference for the optimized furnace is approximately equal to 5 [℃]. This difference can further be decreased by using a time shift for the side heating elements, as explained in the previous section (Figure 6.14). When using a shift of 400 [sec], the maximum temperature difference decreases to ±1.5 [℃], as can be seen in Figure 6.19. Remind again that due to convective effects the resulting temperature differences will be reduced by about 30%. As a result, in the optimized furnace a maximum temperature difference of 1 [℃] is reached. This meets the design requirement for DCB processes as discussed in chapter 1.
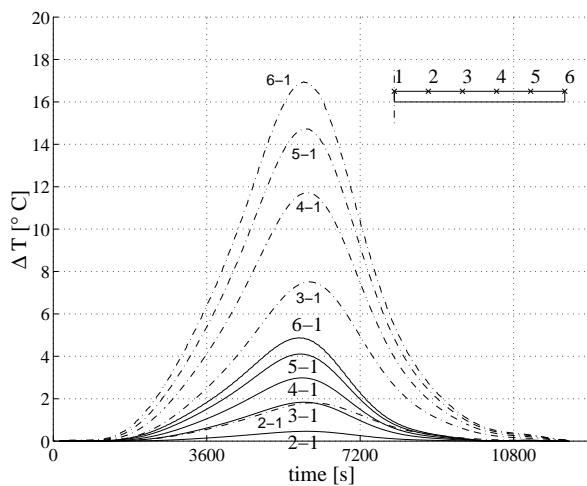

Figure 6.18. Temperature differences over the width of the belt for the optimized (solid, large font) and the non-optimized furnace (dashdot, small font).
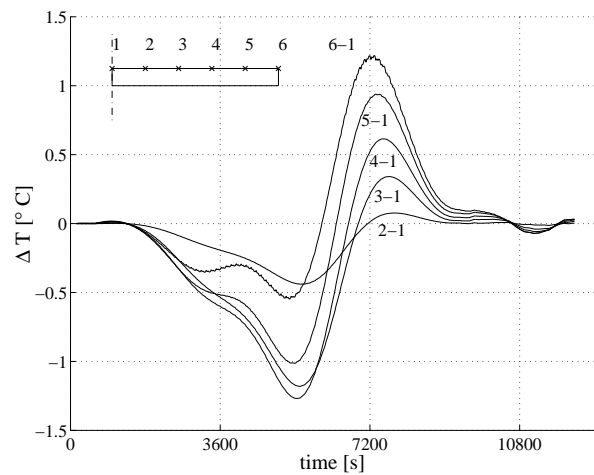
Figure 6.19. Temperature differences over the width of the belt for the optimized furnace when using a time shift of 400 [sec].

CHAPTER 7.
CONCLUSIONS AND RECOMMENDATIONS

7.1 Conclusions

In this study both a furnace model and a design tool for optimizing conveyor belt furnaces are developed. It can be concluded that both the furnace model and the design tool are suitable for calculating the temperature distribution over the width of the belt. With the design tool the influences of material parameters, control behaviour and the geometry on the temperature distribution over the width of the belt can be investigated very easily. From measurements in the experimental set-up it appears that 3-*D* heat transfer effects (both radiative and convective) are of negligible influence to the temperature distribution over the width of the belt. The main effects causing temperature differences over the width of the belt are radiative and conductive heat transfer through the sides of the belt, and non-uniform radiative heat fluxes through the top and bottom surfaces of the belt caused by reflections of radiation against the muffle. Convective heat transfer is a secondary effect, and causes temperature differences to reduce. This forms a justification for omitting convective effects in the design tool. In practice, the temperature uniformity of a conveyor belt furnace can be optimized by using radiation shields at the sides of the belt and by equipping the muffle with an anti-reflective coating. In this way, the radiative fluxes through the side of the belt and the non-uniform reflections against the muffle are minimized. In the experimental set-up, further optimization of the temperature uniformity was realized by using a time shift for the heating elements of the sides. This corresponds to using a lower setpoint temperature for the side elements compared to the top and the bottom in a real conveyor belt furnace. The conductive heat transfer can be reduced by using xenon gas instead of air as medium inside the muffle, or by local cooling. For the muffle geometry studied, using xenon gas (or local cooling) in combination with a coated muffle, radiation shields and a time shift for the heating elements of the sides, the maximum temperature differences over the width of the belt can be reduced to about 1 [°C]. This is good enough for most critical industrial production processes.

7.2 Recommendations

The model developed in this study is suitable for furnaces with a large axial dimension, so that a 2-*D* marching procedure is valid. Besides, the furnaces investigated in this study contain opaque materials. In shorter furnaces, 3-*D* heat transfer effects play a more important role. Therefore, for modelling shorter furnace types the model should be extended to 3-*D*. Also the use of non-opaque materials, like glass, requires an extension of the model. The plane discrete ordinate set used in the present study is valid for non-absorbing media. For absorbing media a general 3-*D* ordinate set is necessary. By also discretizing the polar angle ϑ a 3-*D* discrete ordinate set can be made, which can be integrated in the existing model very easily. Also the use of standard discrete ordinate sets as known in literature is possible. Then the orientation of the ordinates has to be considered again, as this effects the reflection of radiation used in the boundary conditions. A second extension of the radiation model is making it wavelength dependent, which is necessary for modelling materials with wavelength dependent material properties, like glass. This can be done by using a grey band model, in which the total wavelength spectrum is divided into a finite number of grey bands. The model can calculate all the bands separately by using material parameters that fit to the wavelength range of each specific band. At the end the heat fluxes of all the bands can be integrated over the Planck curve to give the total heat flux. The most completing step is a full extension of the model to 3-*D*, which is indispensable

for shorter furnace types, in which 3-*D* heat transfer effects play a more important role than in conveyor belt furnaces. Solving the 3-*D* Navier-Stokes and energy equations is already possible with the standard SEPRAN package. To extend the radiation model to 3-*D*, the 3-*D* discrete ordinate equations have to be solved. As the radiation model makes use of the standard SEPRAN solvers, solving the 3-*D* discrete ordinate equations hardly requires extra programming work. In the 3-*D* model a 3-*D* ordinate set has to be used. Also the routines that calculate the boundary conditions have to be reprogrammed to deal with 3-*D* reflections.

With respect to the experimental set-up, a possible extension is the use of PIV or PTV measurement techniques for measuring quantitative velocity data. As the muffle is filled with air, very small particles are required in order to follow the flow accurately, especially at the low velocities occuring in the muffle. The smaller the particles used in PIV or PTV measurements, the stronger the light sheet has to be in order to make the particles visible. Furthermore, the set-up can be used to test improvement measures as given in this study. By constructing air cooled pipes between the side walls of the muffle and the sides of the plates, the effect of local cooling can be studied. Also the influence of an anti-reflective coating on the muffle and of radiation shields near the sides of the plates can be measured. Finally, the heat transfer in plates of different materials (like glass plates) can be studied.

APPENDIX 1.
THE RADIATIVE TRANSPORT EQUATION IN CARTESIAN COORDINATES

For a grey, non-scattering medium the transport equation for radiation intensity can be written as

$$\frac{di(S)}{dS} = \alpha\big(i_b(S) - i(S)\big). \tag{2.5}$$

Using a 3-*D* Cartesian coordinate system, the radiation intensity depends on three coordinates (x, y, z). The derivative $di(S)/dS$ from equation (2.5) can be expanded giving

$$\frac{di}{dS} = \frac{\partial i}{\partial x}\frac{dx}{dS} + \frac{\partial i}{\partial y}\frac{dy}{dS} + \frac{\partial i}{\partial z}\frac{dz}{dS}. \tag{A1.1}$$

When the curvilinear coordinate S intersects the xz-plane with angle φ and the z-axis with angle ϑ (Figure A1.1), then a distance dS along S can be written as

$$dS = \frac{dx}{\cos(\varphi)\sin(\vartheta)} = \frac{dy}{\sin(\varphi)\sin(\vartheta)} = \frac{dz}{\cos(\vartheta)}. \tag{A1.2}$$

Figure A1.1. Distance dS along a curvilinear coordinate S in a 3-D coordinate system.

In combination with equation (A1.1) it follows for the derivative of i to S:

$$\frac{di}{dS} = \cos(\varphi)\sin(\vartheta)\frac{\partial i}{\partial x} + \sin(\varphi)\sin(\vartheta)\frac{\partial i}{\partial y} + \cos(\vartheta)\frac{\partial i}{\partial z}. \tag{A1.3}$$

Combining this result with equation (2.5) the intensity in a 3-*D* domain is found to be:

$$-\underline{\zeta} \cdot \underline{\nabla} i = \alpha\big(i(x,y,z) - i_b(x,y,z)\big), \tag{2.15}$$

with

$$\underline{\zeta} = \begin{bmatrix} \cos(\varphi)\sin(\vartheta) \\ \sin(\varphi)\sin(\vartheta) \\ \cos(\vartheta) \end{bmatrix}. \tag{A1.5}$$
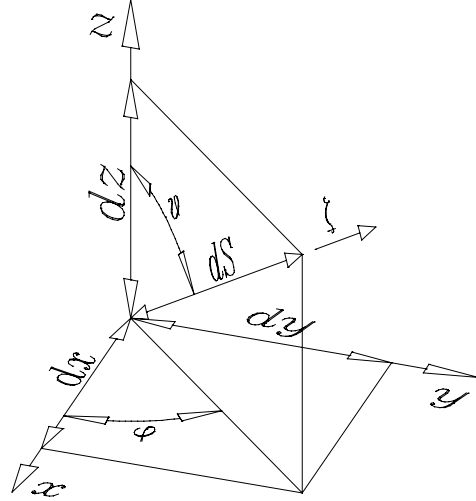
APPENDIX 2.
THE DISCRETE ORDINATE EQUATIONS FOR PLANE AND 3-*D* ORDINATES

The general form of the discrete ordinate equations for radiative transfer is

$$-\underline{\xi}_m \cdot \underline{\nabla} i_m = \alpha\left(i_m - i_b\right),$$

$$m = 1 \ .. \ M \quad (2.16)$$

with $\underline{\xi}_m$ equal to

$$\underline{\xi}_m = \omega_m^{-1} \int_{\omega_m} \underline{\zeta} d\omega, \ m = 1 \ .. \ M \quad (2.17)$$

and $\underline{\zeta}$ equal to

$$\underline{\zeta} = \begin{bmatrix} \cos(\varphi)\sin(\vartheta) \\ \sin(\varphi)\sin(\vartheta) \\ \cos(\vartheta) \end{bmatrix}. \quad (A1.5)$$

Figure A2.1. 3-D solid angle with the bounding planar angles.

The direction vector $\underline{\xi}_m$ is calculated by integrating $\underline{\zeta}$ over the solid angle ω_m corresponding to ordinate *m*. A general 3-*D* ordinate can be defined as depicted in Figure A2.1. For this ordinate the integration in (2.17) is derived as

$$\underline{\xi}_m = \left(\int_{\varphi=\varphi^-}^{\varphi^+} \int_{\vartheta=\vartheta^-}^{\vartheta^+} \sin(\vartheta)d\vartheta \, d\varphi \right)^{-1} \int_{\varphi=\varphi^-}^{\varphi^+} \int_{\vartheta=\vartheta^-}^{\vartheta^+} \underline{\zeta}\sin(\vartheta)d\vartheta \, d\varphi. \qquad m = 1 \ .. \ M \quad (A2.1)$$

Carrying out the integration gives:

$$\underline{\xi}_m = \begin{bmatrix} \dfrac{\left(\sin(\varphi_{m^-}) - \sin(\varphi_{m^+})\right)\left(\sin(\vartheta_{m^-})\cos(\vartheta_{m^-}) - \sin(\vartheta_{m^+})\cos(\vartheta_{m^+}) - \vartheta_{m^-} + \vartheta_{m^+}\right)}{2\left(\varphi_{m^-} - \varphi_{m^+}\right)\left(\cos(\vartheta_{m^-}) - \cos(\vartheta_{m^+})\right)} \\[4mm] \dfrac{\left(\cos(\varphi_{m^+}) - \cos(\varphi_{m^-})\right)\left(\sin(\vartheta_{m^-})\cos(\vartheta_{m^-}) - \sin(\vartheta_{m^+})\cos(\vartheta_{m^+}) - \vartheta_{m^-} + \vartheta_{m^+}\right)}{2\left(\varphi_{m^+} - \varphi_{m^-}\right)\left(\cos(\vartheta_{m^-}) - \cos(\vartheta_{m^+})\right)} \\[4mm] \dfrac{\sin^2(\vartheta_{m^+}) - \sin^2(\vartheta_{m^-})}{2\left(\cos(\vartheta_{m^-}) - \cos(\vartheta_{m^+})\right)} \end{bmatrix}.$$

$$m = 1 \ .. \ M \quad (A2.2)$$

For a given discretization of the total hemisphere around some point into solid angles ω_m the planar angles $\varphi_{m^-}, \varphi_{m^+}, \vartheta_{m^-}$ en ϑ_{m^+} are known, and the vector $\underline{\xi}_m$ can be calculated.
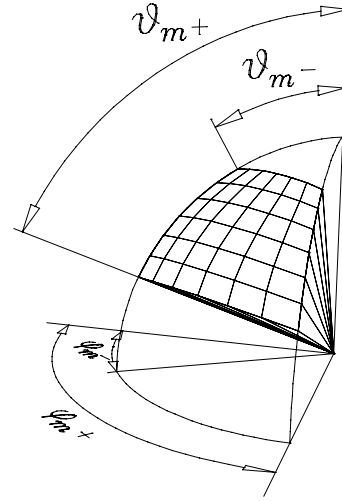
For a semi 2-*D* (plane) ordinate as depicted in Figure A2.2, the bounds of the polar angle are allways $\vartheta^- = 0$ and $\vartheta^+ = \pi$ [rad] for all M ordinates. Substitution in (A2.2) gives $\underline{\xi}_m$ for the plane ordinates:

$$\underline{\xi}_m = \begin{bmatrix} \dfrac{\pi\left(\sin(\varphi^+) - \sin(\varphi^-)\right)}{4(\varphi^+ - \varphi^-)} \\[2ex] \dfrac{\pi\left(\cos(\varphi^-) - \cos(\varphi^+)\right)}{4(\varphi^+ - \varphi^-)} \\[2ex] 0 \end{bmatrix}.$$

$$m = 1 .. M \quad (A2.3)$$

As these plane ordinates are used in 2-*D* geometries, the third component of the equations is never used. As can be seen in (A2.3), the third component of $\underline{\xi}_m$ appears to be 0.
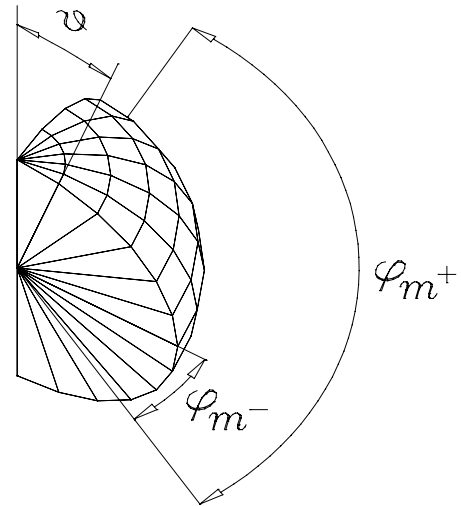

Figure A2.2. Plane ordinate with ϑ integrated from 0 to π [rad].

APPENDIX 3.
THE BOUNDARY COEFFICIENTS

The boundary coefficients determine which part of the radiation from a certain ordinate falls in to a wall. So for every wall/ordinate combination there is a boundary coefficient.
In this appendix the derivation of the boundary coefficient for a general wall/ordinate combination is explained.

In order to determine the boundary coefficients, we first should look at the incident behaviour of rays to a wall. For some wall/direction combination the radiation will hit the wall, and for other combinations not. There are in fact two possible wall/direction combinations, which are both depicted in Figure A3.1. The geometry is drawn counterclockwise, so that the wall vectors of the geometry are always determined.

In the first possibility the ray is directed to the right ($\Delta x_{ray} > 0$). Such a ray hits walls for which:

$H_w > H_{ray}$ and $\Delta x_w > 0$ or
$H_w < H_{ray}$ and $\Delta x_w < 0$,

with H_w the slope of the wall,

H_{ray} the slope of the ray,
x_w the x component of the wall vector and
x_{ray} the x component of the ray vector.

A second possibility is that the ray points to the left ($\Delta x_{ray} < 0$). In this case the ray hits walls for which:

$H_w < H_{ray}$ and $\Delta x_w > 0$ or
$H_w > H_{ray}$ and $\Delta x_w < 0$.

Using these rules it is always possible to determine if a ray falls in to a certain wall or not.

Each ordinate corresponds to a solid angle in space. In order to determine the boundary coefficients one has to determine which part of the solid angle falls in to a certain wall. The solid angle belonging to ordinate m is bounded by two bounding vectors, ζ_m^+ and ζ_m^-. There are now four possible orientations of a solid angle (an ordinate) and a wall. These possibilities are depicted in Figure A3.2.

Figure A3.1. Two possible orientations of the incident radiation direction and a wall.

The first situation occurs when both ζ_m^+ and ζ_m^- point to the wall. In this case, all radiation from the solid angle bounded by ζ_m^+ and ζ_m^- will fall in to the wall, and the boundary coefficient equals 1. So when both ζ_m^+ and ζ_m^- point to the wall, then the boundary coeffcient for this wall/ordinate combination equals:

$$c_{w,m} = 1 \tag{A3.1}$$

In the second case ζ_m^+ points to the wall, while ζ_m^- points from the wall. In this case only a part of the radiation in the ordinate will fall in to the wall. This part equals:

$$c_{w,m} = \frac{\varphi}{\vartheta} \tag{A3.2}$$

with φ the sharp angle between the wall and ζ_m^+, and ϑ the angle between ζ_m^+ and ζ_m^-.
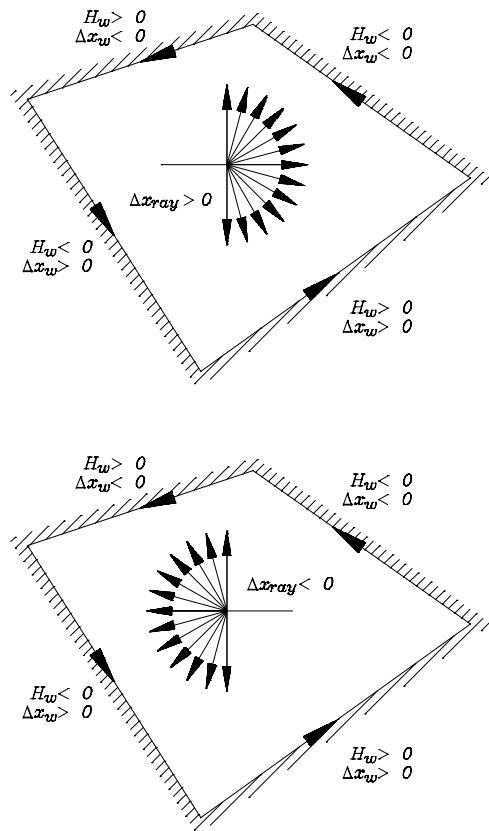
The angle ϑ equals 2π over the total number of ordinates.

$$\vartheta = \frac{2\pi}{M} \qquad (A3.3)$$

The angle φ can be calculated using the vectors $\underline{\zeta}_m^+$ and $\underline{w}$ (the wall vector).

$$\varphi = \arccos\left(\frac{\underline{w} \cdot \underline{\zeta}_m^+}{|\underline{w}| |\underline{\zeta}_m^+|} \right) \qquad (A3.4)$$

Combining equations (A3.2), (A3.3) and (A3.4) gives for the boundary coefficient in the second case:

$$c_{w,m} = \frac{M}{2\pi} \arccos\left(\frac{\underline{w} \cdot \underline{\zeta}_m^+}{|\underline{w}| |\underline{\zeta}_m^+|} \right) \qquad (A3.5)$$

The third situation occurs when $\underline{\zeta}_m^-$ points to the wall and $\underline{\zeta}_m^+$ not. In fact now an analogous derivation as in the second case holds. The result can easily be obtained by changing $\underline{\zeta}_m^+$ and $\underline{\zeta}_m^-$. Then the boundary coefficient equals:

$$c_{w,m} = \frac{M}{2\pi} \arccos\left(\frac{\underline{w} \cdot \underline{\zeta}_m^-}{|\underline{w}| |\underline{\zeta}_m^-|} \right) \qquad (A3.6)$$

The fourth situation at last occurs when neither $\underline{\zeta}_m^+$ nor $\underline{\zeta}_m^-$ hits the wall. In that case no radiation from the ordinate will fall in to the wall, and the boundary coefficient equals:

$$c_{w,m} = 0 \qquad (A3.7)$$

In a geometry a certain number of ordinates is chosen, and the corresponding bounding vectors ($\underline{\zeta}_w^+$ and $\underline{\zeta}_m^-$) are calculated. Also for every wall point the corresponding wall vector $\underline{w}$ and its slope are calculated. For the bounding vectors the rules of Figure A3.1 are applied in order to determine which vectors fall in to a wall. Then it is also determined which situation from Figure A3.2 is dealt with, and the boundary coefficients for every wall/ordinate combination can be calculated.
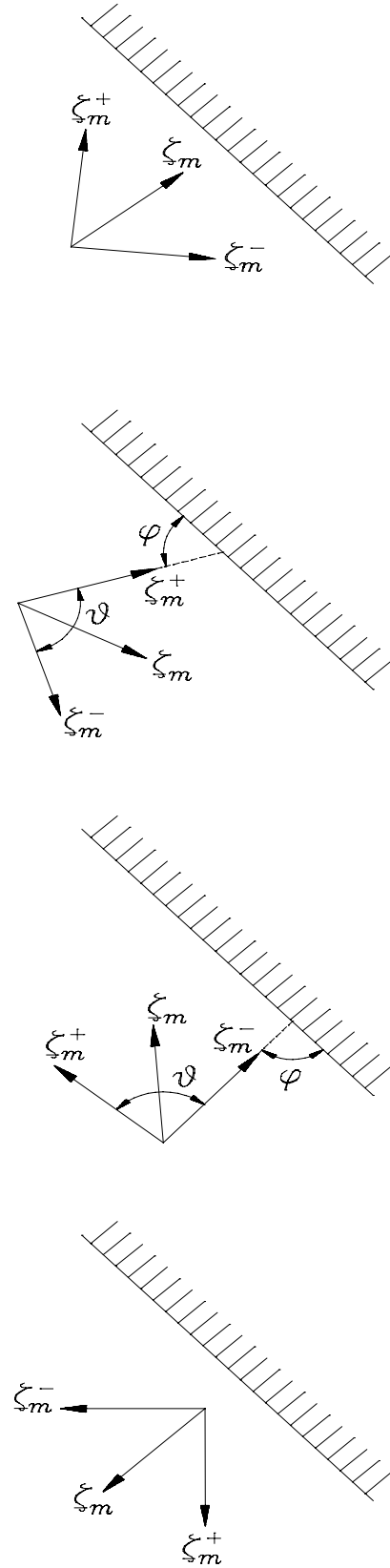

Figure A3.2. The four possibilities of incident radiation from an ordinate to a wall.

APPENDIX 4.
THE REFLECTION COEFFICIENTS

Reflections at walls can be diffuse, specular or something in between (Figure A4.1). At a wall, the incident energy from ordinate m will be reflected to various ordinates pointing from the wall. The part of radiation that is sent from an incident ordinate m to a reflected ordinate m' is determined by the specular and the diffuse reflection coefficients. In this appendix the derivation of these coefficients is explained.
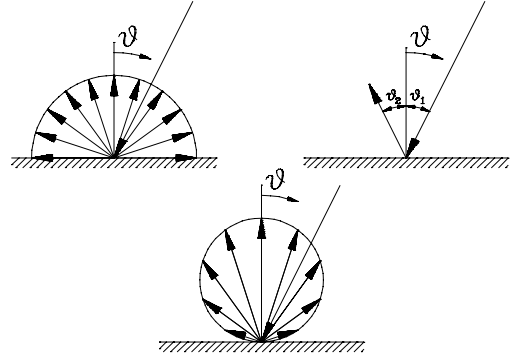
The diffuse reflection coefficient

The diffuse reflection coefficient $c_{w,m \to m'}$ determines the part of the diffusely reflected energy against a wall w coming from ordinate m that is sent to ordinate m'.

$$i_{r,dif_{w,m \to m'}} = c_{dif_{w,m \to m'}} i_{r,dif_{w,m}} \quad . \qquad \text{(A4.1)}$$

Figure A4.1. Diffuse, specular and mixed reflection.

For diffuse reflection the incoming radiation to a wall is reflected into all ordinates the wall is radiating to. The wall is radiating to M_{out} ordinates, so the reflected energy has to be divided over M_{out} ordinates. As explained in paragraph 2.2, the part of an ordinate m' radiation can be reflected to from wall w equals $(1 - c_{w,m'})$. Therefore, the diffuse reflection coefficient from ordinate m to ordinate m' equals:

$$c_{dif_{w,m \to m'}} = \frac{1 - c_{w,m}}{M_{out}} \quad . \qquad \text{(A4.2)}$$

The specular reflection coefficient

For specular reflection, the reflected intensity from ordinate m to ordinate m' can be derived in an analogous way as for diffuse reflection. The reflected intensity can be calculated using a specular reflection coefficient from ordinate m to ordinate m':

$$i_{r,spec_{w,m \to m'}} = c_{spec_{w,m \to m'}} i_{r,spec_{w,m}} \quad . \qquad \text{(A4.3)}$$

For specular reflection the incoming angle of ordinate m equals the angle of reflection. As the incoming and the reflected solid angle are of equal size, the reflected solid angle can coincide with two ordinates (Figure A4.2).
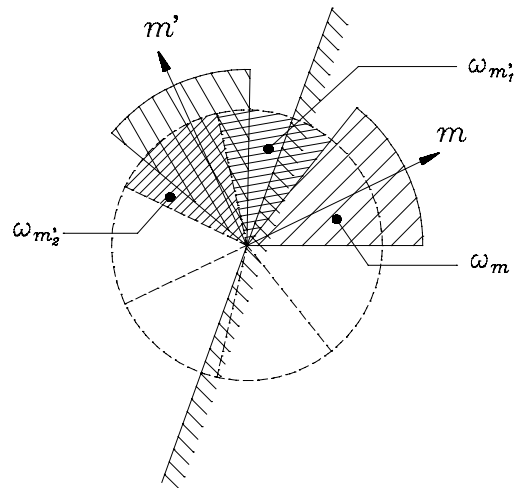
For an ordinate m falling in to a wall w the angle of reflection $\varphi_{m'}$ in Figure A4.3 can be calculated. With this angle, the specular reflection coefficient from ordinate m to the ordinates m'_1 and m'_2 can be derived (Figure A4.3).

Figure A4.2. Specular reflection; reflected solid angle overlaps with two ordinates $\omega_{m1'}$ and $\omega_{m2'}$.

$$c_{spec_{w,m \to m'_1}} = \frac{\varphi_{m'_1} + \dfrac{\pi}{M} - \left(\varphi_{m'} - \dfrac{\pi}{M}\right)}{\dfrac{\pi}{M}}. \qquad (A4.4)$$

Since all the energy that is not reflected into m'_1 will be reflected to m'_2, the reflection coefficient from m to m'_2 can be calculated as:

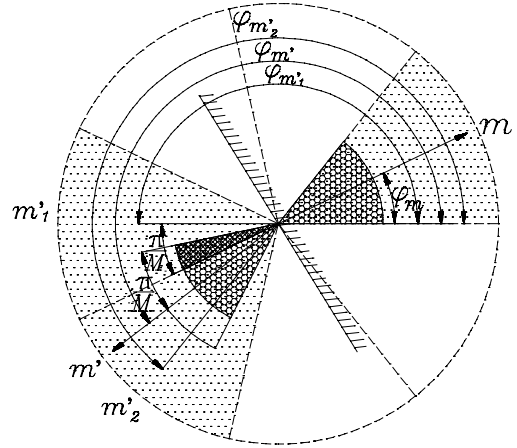$$c_{spec_{w,m \to m'_2}} = 1 - c_{spec_{w,m \to m'_1}}. \qquad (A4.5)$$

Figure A4.3. Angles for determining the specular reflection coefficient.

APPENDIX 5.
QUADRATURE SCHEMES

Various quadrature schemes like Newton Cotes or Gauss schemes can be used in solving the discrete ordinate equations. For 2-*D* quadratic elements, which have to be used in solving the Navier-Stokes equations, some quadrature schemes are not applicable in solving the equations as will be shown in this appendix.

The general form of a discrete ordinate equation is

$$\underline{\xi} \cdot \underline{\nabla} i(\underline{x}) + i(\underline{x}) = i_b(\underline{x}). \tag{A5.1}$$

This equation is transformed into a weak formulation, giving

$$\int_{\Omega} \left(\underline{\xi} \cdot \underline{\nabla} i(\underline{x}) + i(\underline{x}) \right) \varphi_j(\underline{x}) d\Omega = \int_{\Omega} i_b(\underline{x}) \varphi_j(\underline{x}) d\Omega. \qquad j = 1 .. N. \tag{A5.2}$$

When the solution $i(\underline{x})$ is approximated by a combination of basis functions (Galerkin) say

$$i(\underline{x}) = \sum_{k=1}^{N} i_k \varphi_k(\underline{x}), \tag{A5.3}$$

one finds

$$\sum_{k=1}^{N} i_k \int_{\Omega} \left(\underline{\xi} \cdot \underline{\nabla} \varphi_k(\underline{x}) \varphi_j(\underline{x}) + \varphi_k(\underline{x}) \varphi_j(\underline{x}) \right) d\Omega = \int_{\Omega} i_b(\underline{x}) \varphi_j(\underline{x}) d\Omega. \qquad j = 1 .. N. \tag{A5.4}$$

This equation can be written in matrix notation, which gives

$$A \underline{i} = \underline{f}, \tag{A5.5}$$

with

$$A_{j,k} = \int_{\Omega} \left(\underline{\xi} \cdot \underline{\nabla} \varphi_k(\underline{x}) \varphi_j(\underline{x}) + \varphi_k(\underline{x}) \varphi_j(\underline{x}) \right) d\Omega , \quad f_j = \int_{\Omega} i_b(\underline{x}) \varphi_j(\underline{x}) d\Omega.$$

$$j , k = 1 .. N. \tag{A5.6}$$

For one element an element matrix can be derived. If N_i is the number of integration points per element, for a single element the integrals can be approximated using numerical integration in the following way:

$$\int_e g(\underline{x}) d\Omega = \sum_{m=1}^{N_i} g(\underline{x}_m) w_m, \tag{A5.7}$$

with w_m the weights for numerical integration, belonging to the integration points $\underline{x}_m$. Using numerical integration for a matrix element in equation (A5.6) gives:

$$A_{j,k}^e = \int_e \left(\underline{\xi} \cdot \underline{\nabla} \varphi_k(\underline{x}) \varphi_j(\underline{x}) + \varphi_k(\underline{x}) \varphi_j(\underline{x}) \right) d\Omega = \sum_{m=1}^{N_i} \left(\underline{\xi} \cdot \underline{\nabla} \varphi_k(\underline{x}) \Big|_{\underline{x}_m} \varphi_j(\underline{x}_m) + \varphi_j(\underline{x}_m) \varphi_k(\underline{x}_m) \right) w_m.$$

$$j , k = 1 .. N_i. \tag{A5.8}$$

Since for the basis- and the weight functions $\varphi_j(\underline{x}_m) = \delta_{jm}$, equation (A5.8) reduces to:

$$A_{j,k}^e = \left(\underline{\xi} \cdot \underline{\nabla} \varphi_k(\underline{x}) \Big|_{\underline{x}_j} + \delta_{jk} \right) w_j. \qquad j , k = 1 .. N_i. \tag{A5.9}$$

From this it follows that if the weight for numerical integration $w_j = 0$, then a whole row of the element matrix will be zero. In that case the element matrix is singular, and the system cannot be solved. So in order to get a regular element matrix all the weights w_j must be unequal to zero.

Different quadrature schemes use different values for the weights w_j. When using a Newton-Cotes quadrature scheme in combination with quadratic triangular elements, the weights in the corner points of the element appear to be equal to zero too. This quadrature scheme therefore gives a singular element matrix. Another quadrature scheme is required, like a Newton-Cotes scheme with all weights unequal to zero. Also the Gauss quadrature scheme gives a regular matrix, and the system can be solved. Therefore, the Gauss integration scheme is used in the furnace calculations.

APPENDIX 6.
UPWIND TO AVOID OSCILLATIONS

In section 2.6 oscillation problems in 2-*D* geometries have been found. The oscillations seemed to be caused by the appearance of two boundary conditions for a first order differential equation. Using upwind elements the oscillations disappeared. In this appendix the appearance of the oscillations and the upwind solution will be analyzed.

As a benchmark problem the following 1-D first order differential equation will be solved,

$$\frac{\partial i(x)}{\partial x} + i(x) = 1, \tag{A6.1}$$

for $0 \leq x \leq 1$. The left boundary condition is set to $i(0) = 3$, which in combination with equation (A6.1) gives an exact solution equal to:

$$i(x) = 2e^{-x} + 1. \tag{A6.2}$$

At the right hand side of the domain the boundary condition $i(1) = 2$ will be prescribed, which does not coincide with the exact solution of (A6.2). This boundary condition combined with (A6.1) gives an exact solution of:
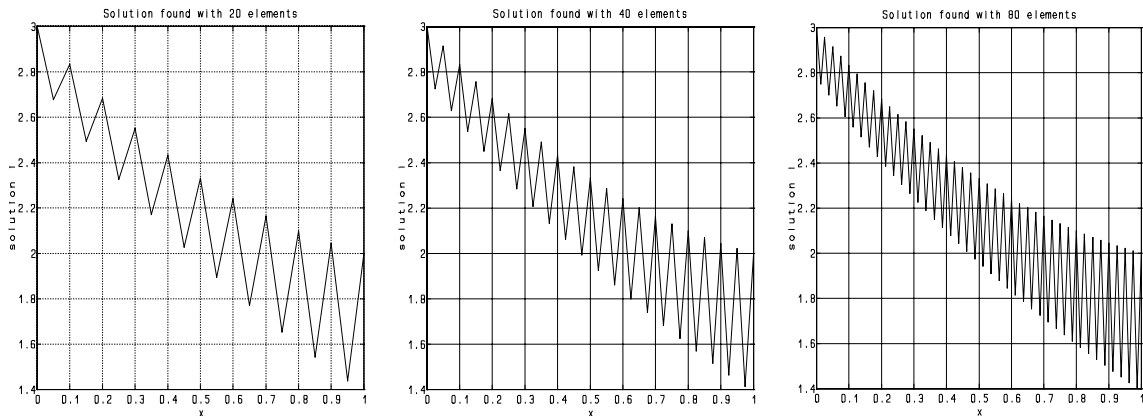
$$i(x) = e^{1-x} + 1. \tag{A6.3}$$

Figure A6.1. Solutions found without upwinding for meshes with 20, 40 and 80 linear 1-D elements.

If the problem with both boundary conditions is solved using the finite element method with standard linear 1-D elements (no upwinding) then an oscillating solution is found. In Figure A6.1 solutions found with different mesh sizes are depicted. As can be seen, the oscillations do not disappear with an increasing mesh density.

The solution found using 20 linear upwind elements is shown as the solid line in Figure A6.2. The exact solution of equation (A6.2) is drawn as a dotted line in the figure. As can be seen, the oscillations have disappeared and the upwind solution fits very well to the exact solution. For complex geometries, as in section 3.2, for several directions also two boundary conditions are prescribed for the discrete ordinate equations. In these geometries upwind elements will be used.
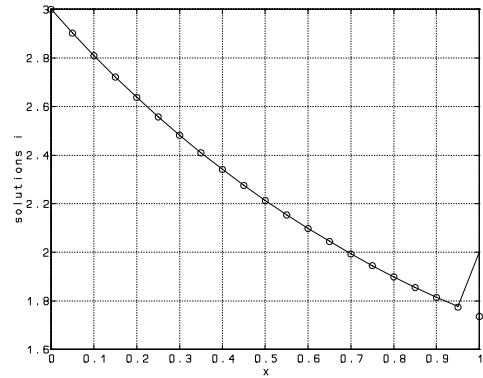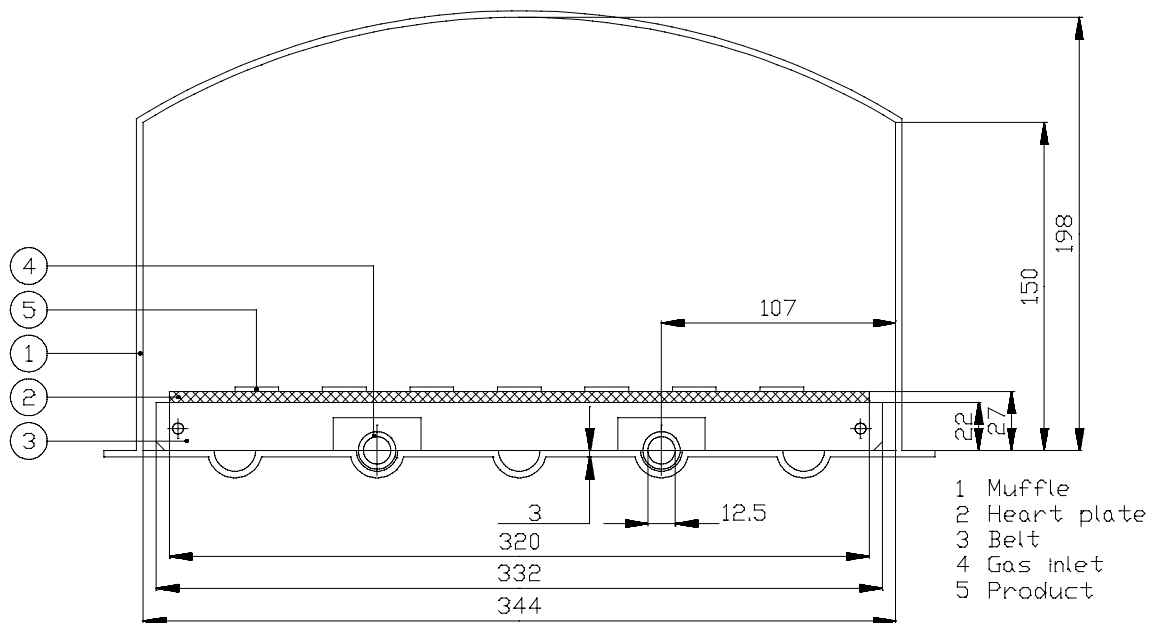

Figure A6.2. Solution found with 20 linear upwind elements (solid) and the exact solution (dotted).
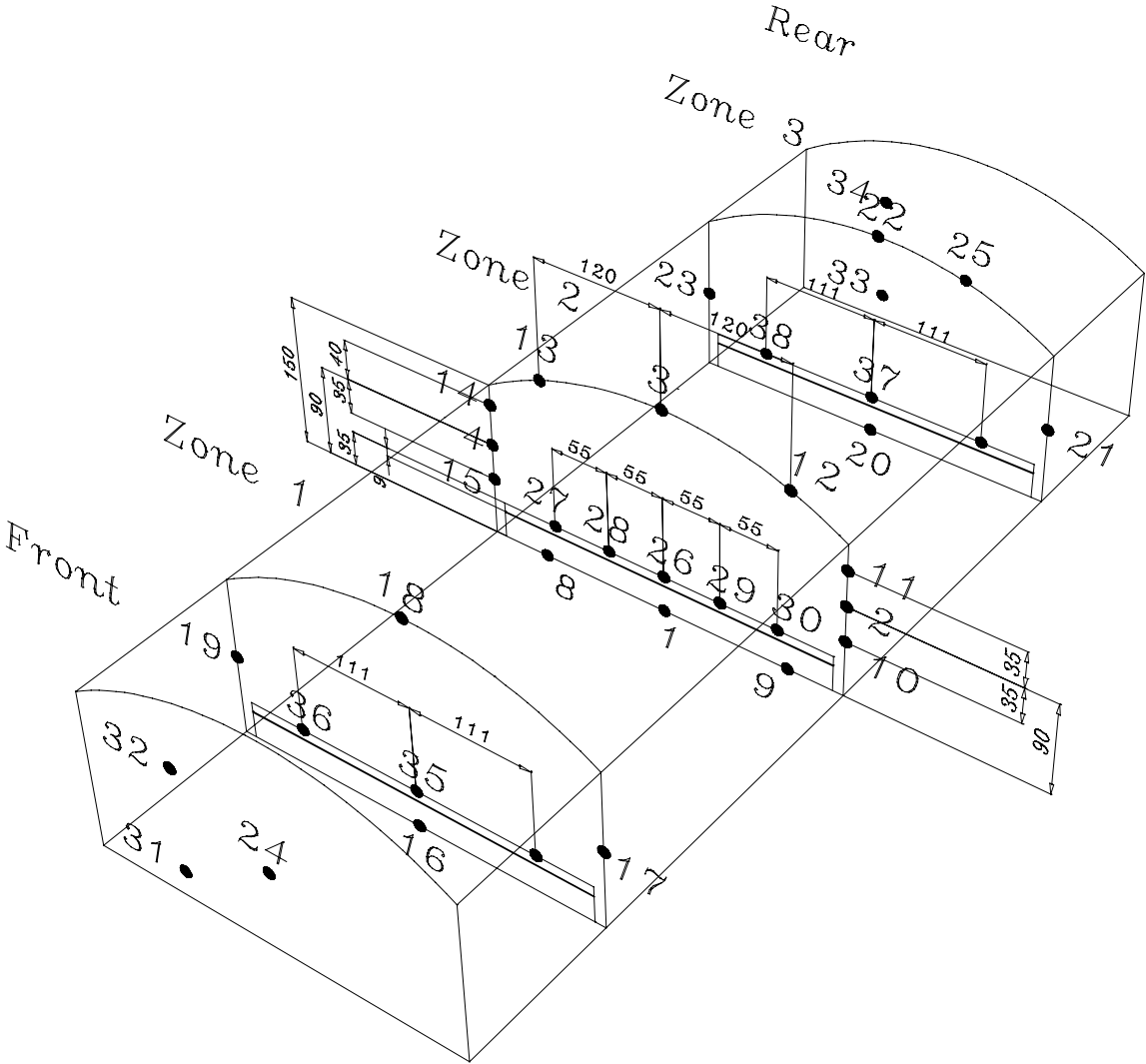
APPENDIX 7.
MUFFLE PROPERTIES

1	Muffle
2	Heart plate
3	Belt
4	Gas inlet
5	Product

Muffle

Material	Steel 310.
Emission coefficient	ε_w = 0.38 [-],
	s_w = 0.68 [-].

Product plates

|	
Material	Steel.
Density	ρ = $7.9 \cdot 10^3$ [kg m^{-3}].
Conduction coefficient	λ = $1.6 \cdot 10^1$ [W m^{-1} K^{-1}].
Heat capacity	c_p = $5.0 \cdot 10^2$ [J kg^{-1} K^{-1}].

APPENDIX 8.
POSITIONING OF THE THERMOCOUPLES IN THE SET-UP

The figure shows the numbering of the type *K* thermocouples for measuring metal surface temperatures. The thermocouples measure the following temperatures respectively:

1, 8, 9, 16 and 20	Bottom of the muffle.
2, 10, 11, 17 and 21	Right side wall of the muffle.
3, 12, 13, 18 and 22	Roof of the muffle.
4, 14, 15, 19 and 23	Left side wall of the muffle.
24, 31 and 32	Front head side of the muffle.
25, 33 and 34	Rear head side of the muffle.
35 and 36	Product plate in zone 1.
26, 27, 28, 29 and 30	Product plate in zone 2.
37 and 38	Product plate in zone 3.
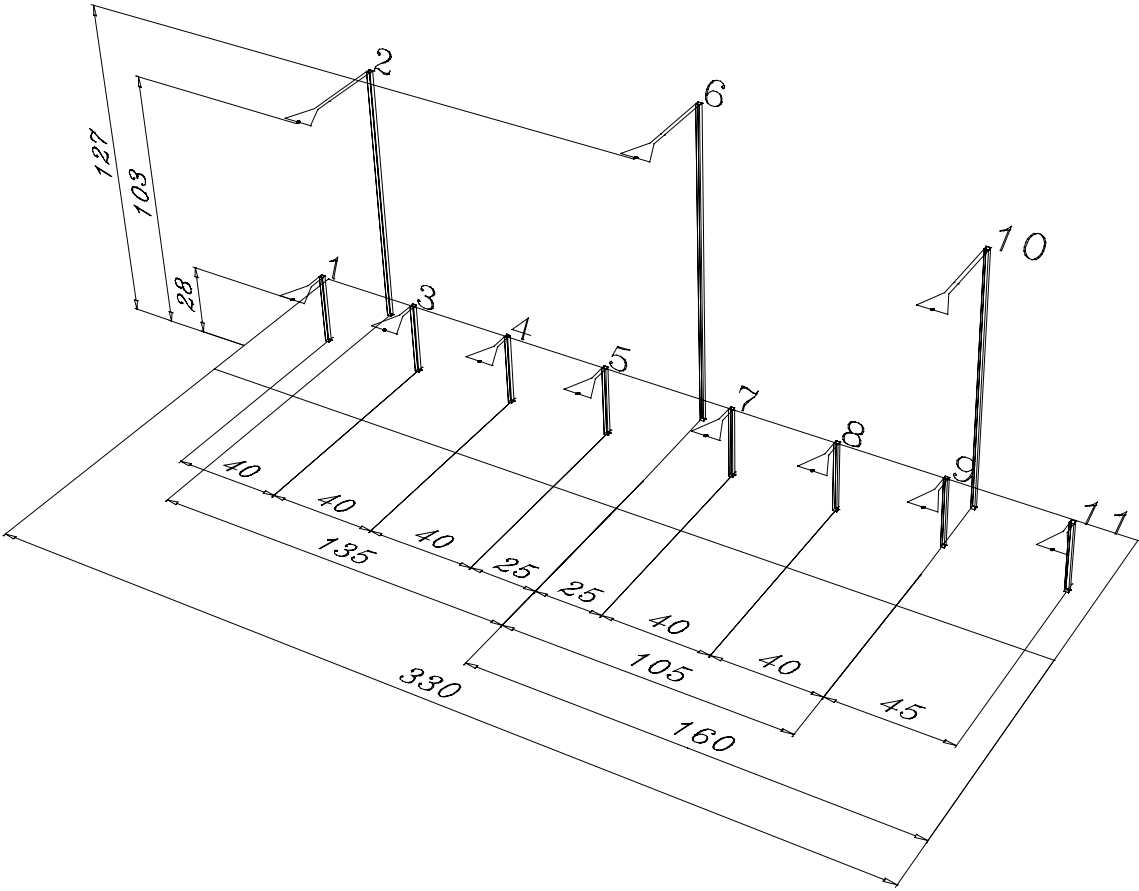
In the figure, the frame with the type *S* thermocouples for measuring air temperatures is shown.

APPENDIX 9.
RESULTS FOR THE MEASUREMENT SETS

In this appendix the measurement results for the various measurement sets done in order to determine the 3-*D* source terms in chapter 5 are summarized.

A9.1 Measurement set 1
Set point 200 [°C], ramp rate 3 [°C/min]

For a set point of 200 [°C] and a ramp rate of 3 [°C/min] a measurement set was created. For the 2-D measurement the preheating was 20 [°C], and the 3-D measurement was done with an axial temperature gradient of about 20 [min/zone]. This measurement set was also used in section 4.2, where temperature histories and shift graphs were already shown.

For the product plate in zone 2 the temperature differences between the thermocouples at the sides and the thermocouple in the middle are depicted in Figure A9.1 and Figure A9.2. The product plate contains 5 thermocouples over its width, which are one middle thermocouple, two inner side thermocouples and two outer side thermocouples. The side thermocouples are placed symmetrical with respect to the middle. As can be seen in the figures, the differences are never higher than about 1 [°C]. As this is about the same order of magnitude of the thermocouple accuracy, no conclusions can be drawn from these graphs with respect to 3-*D* heat transfer effects. The only conclusion to draw is that in this low temperature range no significant differences will occur. Higher differences are expected in the experiments at higher temperatures.
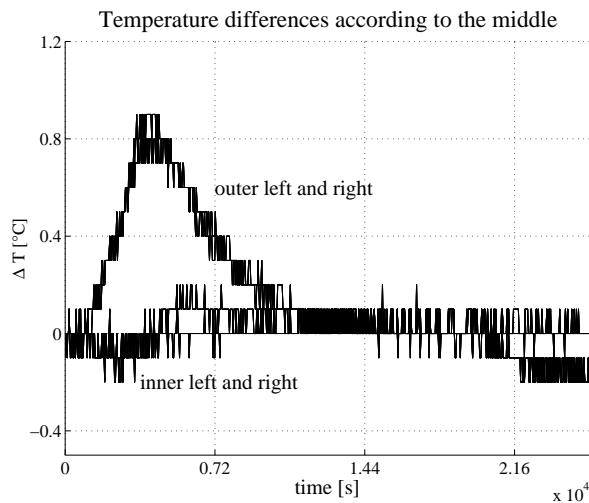

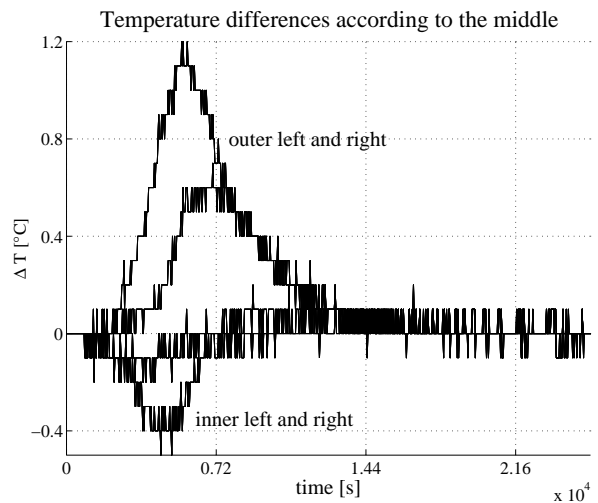*Figure A9.1. Temperature differences compared to the middle for the 2-D experiment in set 1.*

Figure A9.2. Temperature differences compared to the middle for the 3-D experiment in set 1.

A9.2 Measurement set 2
Set point 400 [℃], ramp rate 5 [℃/min]

A set of experiments also has been done with a temperature gradient of 5 [℃/min], and a set point of 400 [℃] for all the zones.
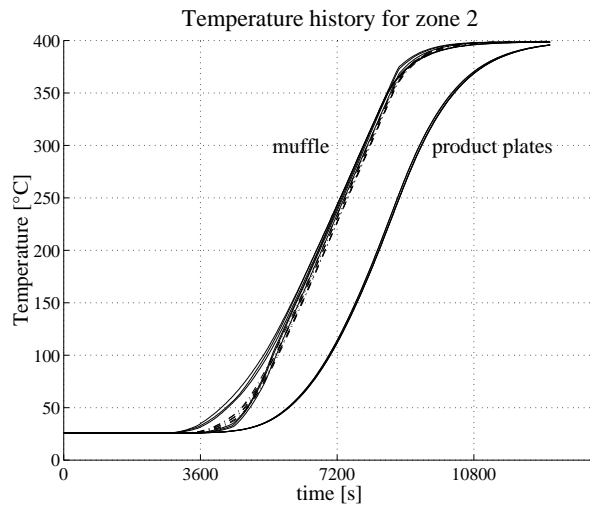

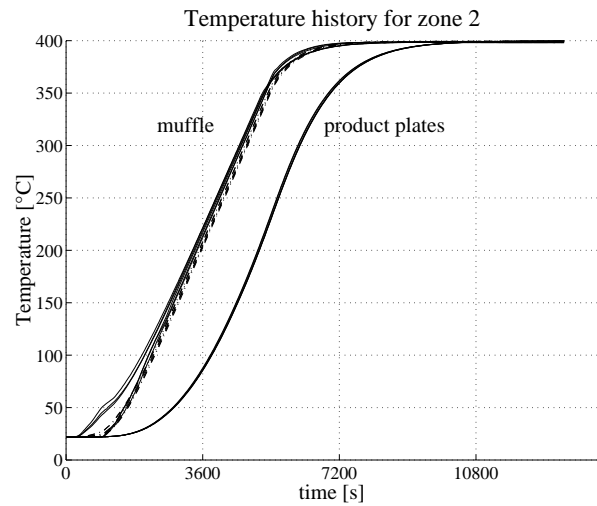*Figure A9.3. Temperature history for zone 2 for the 3-D experiment in set 2.*

Figure A9.4. Temperature history for zone 2 for the 2-D experiment in set 2.

In Figure A9.3 the temperature histories in zone 2 for the 3-D experiment are depicted. The axial temperature gradient was created by turning on the power for the subsequent zones with 15 minutes delay. In this way, a temperature difference of about 60 [℃] arised between neighbouring zones.

The top temperatures appeared to be higher than the other muffle temperatures. The temperature differences of the top control thermocouple compared to the other control thermocouples in zone 2 are graphed against time in Figure A9.5. The maximum temperature differences occured at about 4800 [s], and are equal to about 31 [℃] for the top-bottom difference, and about 24 [℃] for the top-sides differences. The top-sides differences are also expected to be lower than the top-bottom difference because of conductive heat transfer through the muffle.
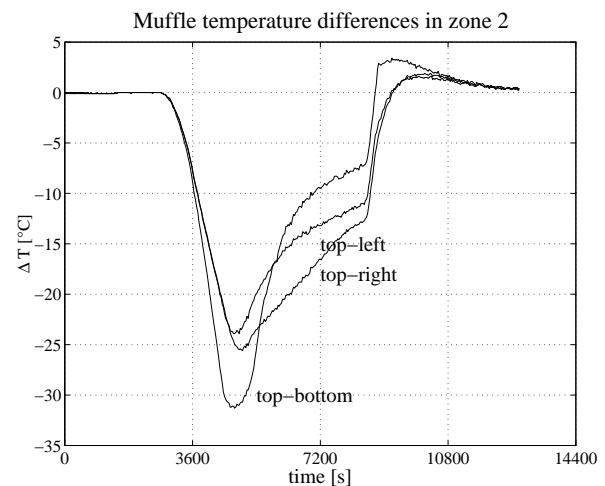

Figure A9.5. Temperature differences between the top thermocouples and the other muffle thermocouples in zone 2.

According to this result, a *2-D* measurement was done with the top elements preheated 25 [℃]. The measured temperature history for zone 2 in this measurement is depicted in Figure A9.4.

The time shift graphs for the thermocouples in zone 2 are depicted in Figure A9.6. As can be seen, between 4000 [s] and 10000 [s] the graphs are approximately horizontal, so the

measurements are comparable during this period. It also appears from this graph that the time shift is approximately equal for all the muffle thermocouples, and is about 3300 [s] in the given time range. Therefore it can be concluded that the two measurements agree quite well, and that the initial preheating of the top elements of 25 [°C] was a good choice.

Just like for the previous set of measurements, the temperature differences between the thermocouples at the sides and the thermocouple in the middle of the product plate in zone 2 were determined. These temperature differences are graphed in Figure A9.7 and Figure A9.8. As can be seen in the figures, the differences near the

Figure A9.6. Time shift graphs for the measurement set at 400 [°C].

sides of the product plates are about 5 [°C], while the differences nearer to the middle of the belt are lower than 1 [°C]. A slight difference can be seen between the left and the right hand side of the furnace. No significant difference in temperature uniformity is measurable between the 2-*D* and the 3-*D* situation.
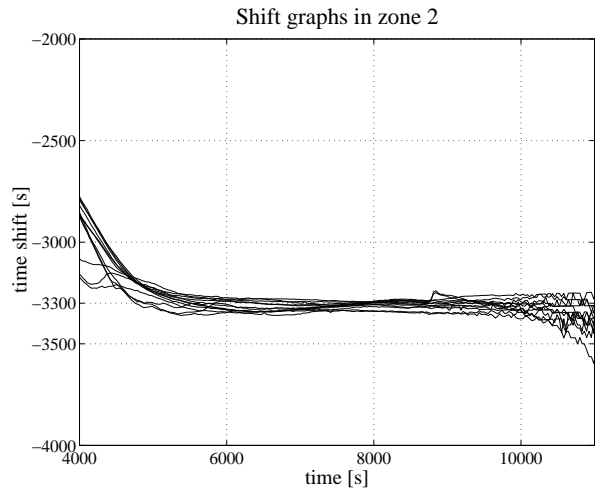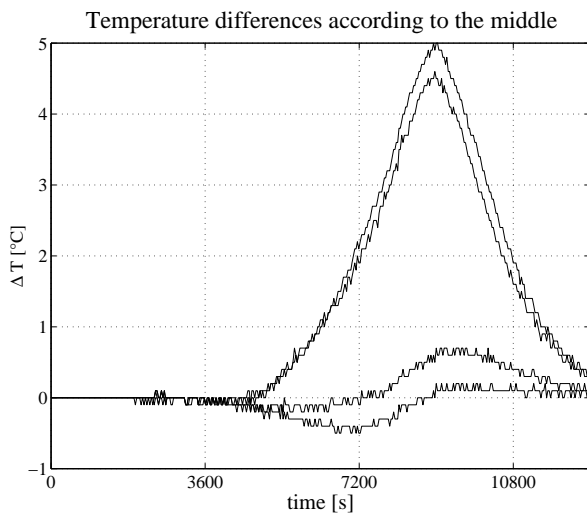

Figure A9.7. Temperature differences compared to the middle for the 3-D experiment in set 2.

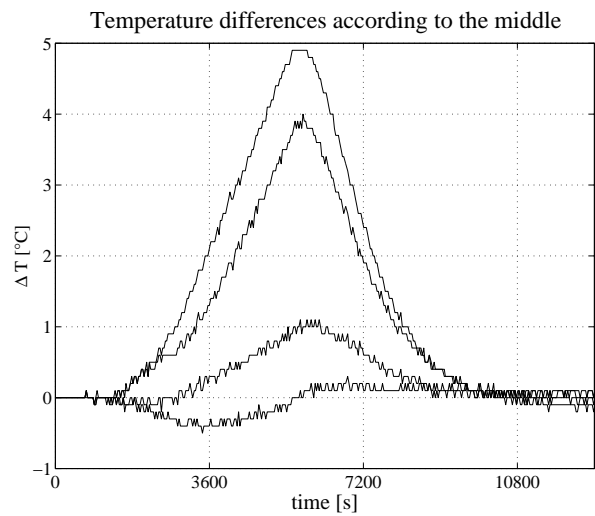*Figure A9.8. Temperature differences compared to the middle for the 2-D experiment in set 2.*

A9.3 Measurement set 3
Set point 600 [℃], ramp rate 5 [℃/min]

The next set of measurements was done for a set point of 600 [℃], with still a ramp rate of 5 [℃/min]. This set point temperature is the highest temperature the test rig was designed for. For the 3-*D* measurement, an axial gradient was created using a delay of 15 minutes between neighbouring zones, resulting in a typical temperature difference of approximately 60 [℃/zone].
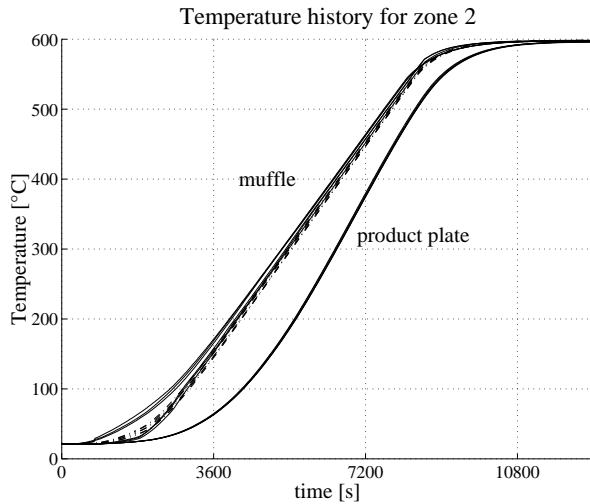

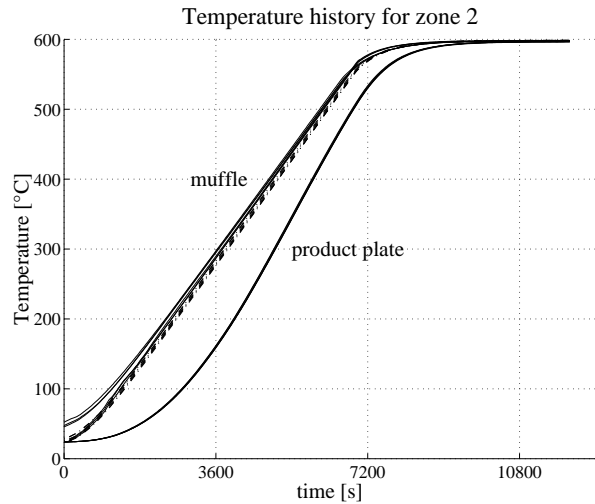*Figure A9.9. Temperature history for zone 2 for the 3-D experiment in set 3.*

Figure A9.10. Temperature history for zone 2 for the 2-D experiment in set 3.

In Figure A9.9 the temperature histories in zone 2 for the 3-*D* experiment are depicted. For this measurement the differences between the top muffle temperature and the other control temperatures of zone 2 are depicted in Figure A9.11. From these graphs, a top preheating of 25 [℃] was estimated to be suitable for the corresponding 2-*D* measurement. The measured temperature history for zone 2 in this 2-*D* measurement is depicted in Figure A9.10.

The time shift graphs for the thermocouples in zone 2 are depicted in Figure A9.12. As can be seen, between 2000 [s] and 8000 [s] a time shift of approximately 1580 [s] is determined. Only the muffle thermocouple in the middle of the bottom has a slightly different time shift. However, because all the other thermocouple profiles, including the two other muffle bottom thermocouples, give equal time shifts in the graph, the initial

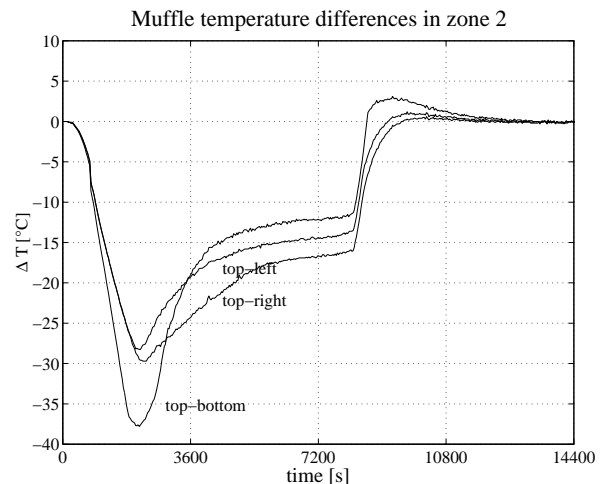*Figure A9.11. Temperature differences between the top thermocouples and the other muffle thermocouples in zone 2.*

preheating of the top elements is expected to be good enough to create a set of measurements that is equivalent enough to be used for comparison. Therefore, this set of measurements will also be used to determine 3-*D* heat transfer effects.

The temperature differences between the thermocouples at the sides and the thermocouple in the middle of the product plate in zone 2 were determined. These temperature differences for both measurements are graphed in Figure A9.13. As can be seen in the figures, the differences are about equal for the 2-*D* and for the 3-*D* measurement, so still in this measurement set 3-*D* effects appear to be negligible, despite the high temperatures. For the outer right hand sides of the product plates the differences compared to the middle is about 5 [℃], while for the outer left hand sides this difference is slightly lower (equal to 3.5 [℃]). The differences with the middle thermocouple for the inner side thermocouples are never larger than 1 [℃].
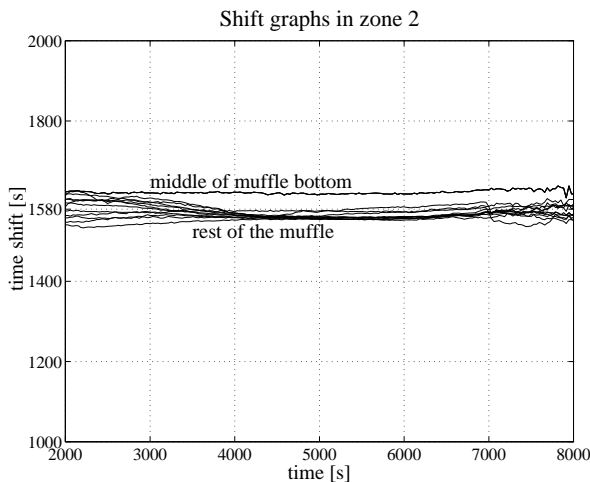

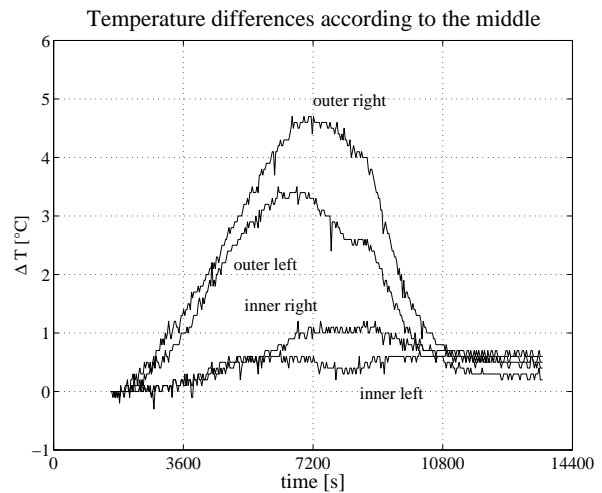*Figure A9.12. Time shift graphs for measurement set 3.*

Figure A9.13. Temperature differences compared to the middle for the 2-D (dashed) and the 3-D (solid) experiment in set 3.

A9.4 Measurement set 4
Set point 600 [℃], ramp rate 8 [℃/min]

3-*D* effects have appeared to be negligible in the previous measurements. The only tests possible using the test-rig for increasing these effects is using a higher ramp rate, in order to create higher belt-muffle temperature differences, and using a higher axial temperature gradient. In this measurement set, the influence of the higher ramp rate is investigated. As the ramp rate used must be lower than 10 [℃/min] in order to avoid too high temperature differences between the several heating elements, a ramp rate of 8 [℃/min] seems a good value for the higher ramp rate. In the 3-*D* measurement, a time delay between the neighbouring zones of 15 minutes was used. Because of the higher ramp rate this also resulted in a higher temperature difference between neighbouring zones (approximately 100 [℃]). Also, a temperature difference between the top and the other control temperatures of 30 [℃] was determined for use as a preheat temperature for the 2-*D* measurement.
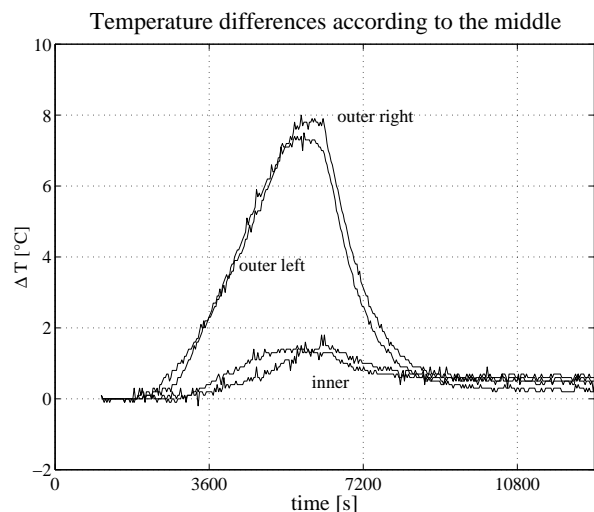

Figure A9.14. Temperature differences compared to the middle for the 2-D experiment (dashed) and the 3-D experiment (solid) in set 4.

The temperature differences between the thermocouples at the sides and the thermocouple in the middle of the product plate in zone 2 were determined. These temperature differences for both measurements are graphed in Figure A9.14. As can be seen in the figures, the differences are still about equal for the 2-*D* and for the 3-*D* measurement, so also for the higher ramp rate 3-*D* effects appear to be negligible. For the outer right hand sides of the product plates the differences compared to the middle are about 9 [°C], while for the outer left hand sides this difference equals about 8 [°C]. The differences with the middle thermocouple for the inner side thermocouples are never larger than 2 [°C]. From comparing this result to Figure A9.13, it can be concluded that the higher ramp rate causes higher temperature differences over the belt width. Because there are no significant differences between the 2-*D* and the 3-*D* measurement results, these larger differences must be caused by larger cross-sectional temperature gradients, which makes them analysable as 2-*D* effects.

A9.5 Measurement set 5
Set point 600 [°C], ramp rate 8 [°C/min], increased axial gradient

In order to determine from which point the 3-*D* effects start to play a role of importance for the temperature uniformity, the axial temperature gradient in the test-rig will be varied in order to increase the 3-*D* effects. The set of measurements in this section is equal to the previous set, with as only difference a higher axial temperature gradient of 25 minutes per zone, resulting in an axial temperature gradient of approximately 120 [°C] between neighbouring zones. After performing the 3-*D* measurement, a top temperature offset of 50 [°C] comparing to the other control temperatures in zone 2 was determined, which was used as preheating in the 2-*D* measurement afterwards.
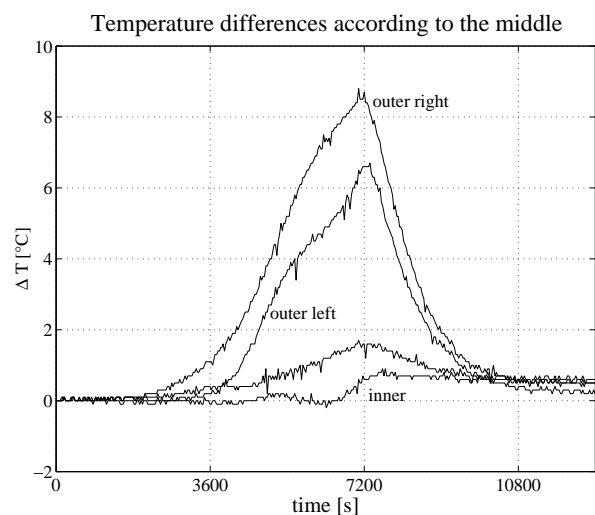
Figure A9.15. Temperature differences compared to the middle for the 2-D experiment (dashed) and the 3-D experiment (solid) in set 5.

The temperature differences between the thermocouples at the sides and the thermocouple in the middle of the product plate in zone 2 were determined. These temperature differences for both measurements are graphed in Figure A9.15. As can be seen, there is hardly any difference between Figure A9.15 and Figure A9.14. The higher axial temperature gradient had no effect on the temperature uniformity over the belt width. Again it can be concluded that 3-*D* heat transfer effects were negligible.

REFERENCES

Brooks, A.N. and Hughes, T.J.R., 1982,
> *"Streamline upwind/Petrov Galerkin formulations for convection dominated flows with particular emphasis on the incompressible Navier-Stokes equations"*, Computer methods in Applied Mechanics and Engineering, Vol. 32, pp. 199-259.

Burns G.W., Scroger M.G., Strouse G.F., Croarkin M.C. and Guthrie W.F., 1993,
> *"Temperature-Electromotive Force Reference Functions and Tables for the Letter-Designated Thermocouple Types Based on the ITS-90"*, National Institute of Standards and Technology, Monograph 175.

Chawla, T.C. and Chan, S.W., 1980,
> *"Combined Radiation Convection in Thermally Developing Poiseuille Flow with Scattering"*, Journal of Heat Transfer, Vol. 102, pp. 297-302.

Chung, T.J. and Kim, J.Y.. 1984,
> *"Two-Dimensional, Combined-Mode Heat Transfer by Conduction, Convection and Radiation in Emitting, Absorbing, and Scattering Media - Solution by Finite Elements"*, Journal of Heat Transfer, Vol. 106, pp. 448-452.

Cuvelier, C., Segal, A., and van Steenhoven, A.A., 1986,
> *"Finite element methods and Navier-Stokes equations"*, D. Reidel Publishing Company, Dordrecht/Boston/Lancaster/Tokyo.

Fiveland, W.A.. 1984,
> *"Discrete-Ordinate Solutions of the Radiative Transport Equation for Rectangular Enclosures"*, Journal of Heat Transfer, Vol. 106, pp. 699-706.

Fiveland, W.A., 1988,
> *"Three-Dimensional Radiative Heat-Transfer Solutions by the Discrete-Ordinates Method"*, Journal of Thermophysics and Heat Transfer, Vol. 2, pp. 309-316.

Gray, D.D. and Giorgini A., 1976,
> *"The validity of the Boussinesq approximation for liquids and gases"*, International Journal of Heat and Mass Transfer, Vol. 19, pp. 545-551.

Henkes, R.A.W.M., 1990,
> *"Natural convection boundary layers"*, Huisdrukkerij Delft University, Delft.

Kanthal,
> *Kanthal AB*, Box 502, SE-734 27 Hallstahammar, Sweden, http://www.kanthal.se.

Le Dez, V. and Charette, A., 1994,
> *"Application of the Discrete Ordinates Method to a Bidimensional Grey Medium of Complex Shape in Radiative Equilibrium"*, Eurotherm seminar 36, pp. R1-R9.

Lide, D.R., 1994,
> *"CRC Handbook of Chemistry and Physics"*, 75th edition, CRC Press, Inc., Florida.

Limpens, M.P.M.A., 1997,
> *"2-D Coupled Radiation and Convection Modelling in an Industrial Furnace"*, SAI Design Thesis, ISBN 90-5282-818-0.

Liu, F., Becker, A. and Pollard, A., 1996,
> *"Spatial differencing schemes of the discrete-ordinate method"*, Numerical Heat Transfer, Vol. 30, pp. 23-43.

Oberbeck, A., 1888,
> *"Uber die Bewegungserscheinungen der Atmosphaere"*, Sitzungsberichte der Königlich Preuszischen Akademie der Wissenschaften", pp. 1129-1138.

Selçuk, N. and Kayakol, N., 1997,
> *"Evaluation of discrete ordinates method for radiative transfer in rectangular furnaces"*, International Journal of Heat and Mass Transfer, Vol. 40, pp. 213-222.

Segal, A., 1995,
> *"SEPRAN Introduction, Users Manual, Programmers Guide and Standard Problems"*, Ingenieursbureau SEPRA, Leidschendam, The Netherlands.

Siegel, R. and Howell, J.R., 1992,
> *"Thermal radiation heat transfer"*, Hemisphere Publishing Corporation, Washington.

Verhaar, B.T., 1999,
> *"Design of an experimental set-up simulating a conveyor belt furnace"*, Eindhoven University of Technology, Department of Mechanical Engineering, Report nr. WET99.003.

NOMENCLATURE

Symbol	Description	Standard units
A	surface area	[m^2]
c	boundary coefficient	[-]
c_p	heat capacity	[J kg^{-1} K^{-1}]
F	configuration factor	[-]
g	acceleration of gravity	[m s^{-2}]
H	slope	[-]
h	thickness	[m]
h_c	conduction coefficient	[W m^{-2} K^{-1}]
i	radiation intensity	[W m^{-2} sr^{-1}]
i_b	black body intensity	[W m^{-2} sr^{-1}]
K_p	proportional control action	[W K^{-1}]
k	conduction coefficient	[W m^{-1} K^{-1}]
O	order of magnitude	
p	pressure	[N m^{-2}]
Q	power	[W]
Q'	power per unit length	[W m^{-1}]
q	heat flux	[W m^{-2}]
L	reference length	[m]
l	length	[m]
M	number of ordinates	[-]
m	mass	[kg]
n	perpendicular coordinate	[m]
S	path coordinate	[m]
T	temperature	[K]
T_p	proportional band	[K]
ΔT	temperature difference	[K]
t	time	[s]
Δt	timestep	[s]
U	reference velocity	[m s^{-1}]
u	velocity	[m s^{-1}]
w	weight	[-]
x,y,z	Cartesian coordinates	[m]
α	medium absorption coefficient	[m^{-1}]
α_w	wall absorption coefficient	[-]
δ	Kronecker delta	
ε_w	wall emission coefficient	[-]
ζ	arbitrary factor	[-]
$\underline{\zeta}$	direction vector	[-]
η	dynamic viscosity	[kg m^{-1} s^{-1}]
ϑ	polar angle	[rad]
λ	wavelength	[m]
$\underline{\xi}$	ordinate vector	[-]
ρ	density	[kg m^{-3}]
Y_d	differentiation time	[s]
ρ_w	wall reflection coefficient	[-]
σ	Stefan-Boltzmann constant	[W m^{-2} K^{-4}]
σ_s	scattering coefficient	[m^{-1}]
Y_w	wall transmission coefficient	[-]
Φ	phase function for scattering	[-]
φ	azimuthal angle	[rad]

Symbol	*Description*	*Standard units*
ω	solid angle	[sr]
$\underline{\nabla}$	gradient operator	[m⁻¹]
2-*D*	two-dimensional	
3-*D*	three-dimensional	

Dimensionless ratios

Fo	Fourier number
Fr	Froude number
Gr	Grashof number
N	conduction/radiation parameter
Pe	Péclet number
Re	Reynolds number
Sr	Strouhal number

Subscripts

a	absorbed
b	black body
	belt
dif	diffuse
e	emitted
el	elements
in	incident
k	conductive
m	muffle
	ordinate number
max	maximum
out	outer
p	projected
r	reflected
rad	radiant
s	scattered
	stones
set	setpoint
spec	specular
t	transmitted
w	wall
λ	wavelength dependent
0	reference
∞	environment

Superscripts

+,-	bounds
*	dimensionless

SUMMARY

In this study the improvement of the temperature uniformity in an industrial conveyor belt furnace is the main topic. In a conveyor belt furnace, the products follow a certain temperature history as they are transported through the furnace by means of a conveyor belt. For setting the temperature history of the products the furnace is divided into several electrically heated zones, each with an own temperature setting. For some production processes, a very high temperature accuracy is required (±2 [℃] at an absolute temperature level of 1000 [℃]). When several product rows are placed next to each other on the conveyor belt, then automatically a uniform temperature distribution over the width of the belt is required.

To get an understanding of the heat transfer phenomena in a conveyor belt furnace, a numerical model is made for calculating the heat fluxes. Because of the relatively large length of the muffle compared to its cross-sectional dimensions, a 2-D model is chosen for. Three dimensional (axial) effects are supposed to be of less importance, but can be taken into account in the model by means of source terms. The transport equation for radiative intensity is discretized with the Discrete Ordinate Method, after which all heat transfer equations are solved using the finite element package SEPRAN. From comparing the several heat fluxes to each other it appears that radiation and local conductive effects are the most important phenomena in disturbing the temperature uniformity over the width of the belt. Therefore, the model is simplified to a design tool, in which only these effects are taken into account, and which has the ability of making fast calculations on a new furnace configuration.

For comparing the model to reality, and also for checking if the assumptions on which the model is based are valid, an experimental set-up is built. This set-up consists of three zones of a real conveyor belt furnace, in which the belt has been replaced by steady (possible cooled) plates. With the set-up temperatures can be measured of the muffle walls and the plate surfaces, and also of the air at several positions. Also the flow pattern inside the muffle can be visualized by means of a system of lenses and smoke injection. In this way the furnace is used for simulating a real furnace, and for investigating the flow phenomena inside the muffle. From simulations it appears that the flow pattern inside the muffle is very strongly dependent on the wall temperatures of the muffle, and is also predicted accurately by the numerical model. Three dimensional effects appear to be of minor influence on the temperature distrubution over the width of the belt. In this way it is demonstrated that the design tool is capable of calculating the temperature distribution over the width of the belt with a satisfactory accuracy.

Using the design tool, an optimization study is done for a conveyor belt furnace. The influence of the several heat transfer phenomena on the temperature distribution over the width of the belt is analyzed. Also the influence of the geometry, material properties and the control strategy of the heating elements is investigated. From this, design rules for a new conveyor belt furnace have been formulated. In theory, the temperature distribution is completely uniform for a non-reflecting muffle and when no heat transfer through the sides of the belt takes place. In practice, a temperature distribution with a maximum deviation of 1 [℃] can be realized. This is satisfactory for critical production processes.

SAMENVATTING

In deze studie staat het verbeteren van de temperatuur-uniformiteit in industriële band-doorloopovens centraal. In een banddoorloopoven ondergaan producten een bepaald temperatuurtraject door ze op een lopende band door de oven heen te trekken. Om het temperatuurtraject van de producten in te stellen is de oven verdeeld in een aantal elek-trisch verwarmde zones, elk met een eigen temperatuurinstelling. Voor sommige produc-tieprocessen is een zeer hoge temperatuurnauwkeurigheid vereist (±2 [℃] bij een absolute temperatuur van ongeveer 1000 [℃]). Indien meerdere productrijen naast elkaar op de band liggen wordt dan automatisch een hoge temperatuuruniformiteit over de breedte van de band vereist.

Om begrip te krijgen van de warmteoverdrachtsfenomenen in een banddoorloopoven is een numeriek model opgesteld ter berekening van de warmtestromen. Vanwege de relatief grote lengte van de muffel t.o.v. de afmetingen in een dwarsdoorsnede is gekozen voor een tweedimensionaal model. Driedimensionale (axiale) effecten worden geacht van minder invloed te zijn, maar kunnen wel worden toegevoegd aan het model door middel van brontermen. In het model worden warmteoverdracht door straling, convectie en geleiding meegenomen. De stralingsvergelijkingen worden gediscretiseerd volgens de Discrete Ordinaten Methode, waarna alle warmteoverdrachtsvergelijkingen opgelost wor-den met het eindige elementen pakket SEPRAN. Uit een vergelijking van de warmtestro-men ten opzichte van elkaar blijkt dat vooral straling en lokale geleidingseffecten een noe-menswaardige invloed hebben op de temperatuuruniformiteit. Het model is daarom vereenvoudigd tot een ontwerpgereedschap, waarin alleen de laatste effecten gemodel-leerd zijn, en waarmee het mogelijk is om snel een nieuwe ovenconfiguratie door te rekenen.

Om het model te toetsen aan de werkelijkheid, en ook om te controleren of de gedane aannamen kloppen, is er een experimentele opstelling gebouwd. Deze opstelling bestaat uit drie zones van een echte banddoorloopoven, waarbij de band vervangen is door stilliggende (eventueel gekoelde) platen. Met de opstelling kunnen wandtemperaturen van de muffel en de platen, en ook luchttemperaturen op verschillende posities worden gemeten. Ook kan het stromingsveld gevisualiseerd worden m.b.v. een lenzensysteem en rookinjectie. Zodoende wordt de opstelling gebruikt voor simulatie van een echte oven, en ook voor het onderzoeken van stromingsverschijnselen in de muffel. Uit de simulaties blijkt dat het stromingspatroon in de muffel sterk afhankelijk is van de opgedrukte rand-temperaturen, en ook goed wordt voorspeld door de numerieke code. Ook blijkt dat driedimensionale effecten geen noemenswaardige invloed hebben op de temperatuuruni-formiteit over de breedte van de band. Op deze manier is aangetoond dat het ontwerpge-reedschap nauwkeurig genoeg is om de temperatuuruniformiteit over de breedte van de band te voorspellen.

Met het ontwerpgereedschap is een optimalisatiestudie uitgevoerd voor een banddoor-loopoven. De invloed van de verschillende warmteoverdrachtsfenomenen op de tempera-tuurverdeling over de breedte van de band is geanalyseerd. Ook de invloeden van de geometrie, materiaaleigenschappen en van de regeling van de verwarmingselementen zijn onderzocht. Hieruit zijn ontwerpregels opgesteld voor een nieuwe banddoorloopoven. Theoretisch is de temperatuurverdeling over de breedte van de band uniform voor een niet reflecterende muffel, en wanneer er geen warmtestromen zijn door de zijkanten van de band. Praktisch haalbaar is een temperatuurverdeling met maximaal 1 [℃] afwijking. Dit is voldoende voor kritische productieprocessen.

NAWOORD

Aan het einde van dit onderzoek kijk ik terug op een leerzame promotietijd in een bijzonder prettige werkomgeving. De goede sfeer in de groep is de belangrijkste reden waardoor voor mij de vijf jaar onderzoek enorm snel voorbijgegaan lijken te zijn. Dat een aantal collega's ook van mening was dat differentiaalvergelijkingen en meetstrategieën van tijd tot tijd plaats moeten maken voor een al dan niet onzinnig gesprek bij een kop koffie, een potje zaalvoetbal in de pauze, of een borrel op donderdagmiddag vond ik zeer positief. Hiervoor bedank ik al mijn collega's uit de groep Energietechnologie aan de Technische Universiteit Eindhoven.

Verder bedank ik het Stan Ackermans Instituut en de firma Gemco Furnaces voor de financiële ondersteuning van het onderzoek. Voor de goede begeleiding en de betrokkenheid bij het onderzoek wil ik in de eerste plaats mijn directe begeleider Camilo Rindt en mijn eerste promotor Anton van Steenhoven bedanken. De overige leden van de kerncommissie, prof. Mattheij, prof. van der Meer en prof. Brouwers bedank ik voor de nuttige suggesties met betrekking tot het proefontwerp. Voor de begeleiding vanuit Gemco Furnaces bedank ik Geert Janssen, Jos Bakema en Bert Benthem.

Ook stagiaires en afstudeerders boden welkome hulp tijdens het onderzoek. Op het numerieke vlak is door sommigen direct meegewerkt aan de uiteindelijke code. Ook werden door de brede variatie in de onderwerpen van stages en afstudeeropdrachten allerlei uitdagingen aangedragen om de bestaande code te testen en te verbeteren. Met name bedank ik Dave Doerwald, Erwin Niessen, Pieter van der Jagt, Roger Kroonen, Rob Jansen en Marcel Cremers voor hun bijdragen aan het numerieke werk. Met betrekking tot het experimentele stuk bedank ik Boudewijn Verhaar voor de onmisbare steun bij het ontwerpen van de testoven en het meetsysteem, en Alberto Sarrantonio voor het doen van testmetingen ter controle van het numerieke model.

Verder wil ik nog bedanken:
Dhr. Cappon voor de ondersteuning bij het ontwerpen van het meetsysteem.
Piet en Rob van Gemco Furnaces voor het bouwen van de testoven.
Frits, Frank en Erik voor de ondersteuning bij werkzaamheden in het lab.
Lambert en Peter voor hun ondersteuning in de werkplaats, zowel met betrekking tot mijn onderzoek als ook bij technische hobbies van andere aard.
Ad, Jan en Roy voor de ondersteuning met betrekking tot computers en meetapparatuur.
Rian en Marjan voor de administratieve ondersteuning.
Mijn ouders, voor alle steun, en voor de laatste correcties van dit proefontwerp.

CURRICULUM VITAE

July 20th 1972   Born in Geleen, The Netherlands.

1984 - 1990   Pre-university Education (Gymnasium)
Scholengemeenschap Sint Michiel, Geleen.

1990 - 1995   Mechanical Engineering at the
Eindhoven University of Technology.
Graduated within the division of
Energy Technology,
on a *'Radiation Model for Complex Geometries'*.

1995 - 1997   Designer course in Computational Mechanics,
Stan Ackermans Institute,
Eindhoven.
'2-D Coupled Radiation and Convection Modelling in an Industrial Furnace'

1997 - 2000   Doctoral design project,
Stan Ackermans Institute,
Eindhoven,
'A Design Tool for Conveyor Belt Furnaces'.

2000 -   research work at the Systems & Processes Division of TNO Institute of
Applied Physics.

INDEX